Non-equilibrium dynamics in ordered modulated phases

von der Fakultät für Naturwissenschaften
der Technischen Universität Chemnitz
genehmigte Dissertation zur Erlangung des akademischen Grades

doctor rerum naturalium

(Dr. rer. nat.)

vorgelegt von M. Sc. Christian Riesch
geboren am 13.01.1984 in Kassel
eingereicht am 20.05.2015

Gutachter: Prof. Dr. Robert Magerle
Prof. Dr. Günter Radons

Tag der Verteidigung: 03.07.2015

`http://nbn-resolving.de/urn:nbn:de:bsz:ch1-qucosa-172821`

Bibliografische Beschreibung

Riesch, Christian
Non-equilibrium dynamics in ordered modulated phases
Dissertation (in englischer Sprache), Technische Universität Chemnitz,
Fakultät für Naturwissenschaften, Chemnitz, 2015
140 Seiten, 67 Abbildungen

Referat: In der vorliegenden Arbeit wird die Dynamik geordneter modulierter Phasen außerhalb des thermischen Gleichgewichts untersucht. Der Schwerpunkt liegt auf einem zweidimensionalen, streifenbildenden System, genannt Modell B mit Coulomb-Wechselwirkung, welches aus einem geordneten Anfangszustand unter dem Einfluß eines Rauschterms relaxiert. Aus den mittels numerischer Simulationen gewonnenen Daten wird die lokale Orientierung der Streifen extrahiert und deren raum-zeitliche Korrelationsfunktionen berechnet. Wir beobachten eine langsame Dynamik und Alterungseffekte in der Zwei-Zeit-Autokorrelationsfunktion, welche einer Skalenform folgt, die aus kritischen Systemen bekannt ist. Dies geht einher mit dem Wachstum einer räumlichen Korrelationslänge senkrecht zu den Streifen. Zu sehr späten Zeiten klingt die zugehörige räumliche Korrelationsfunktion mit einem Potenzgesetz ab. Weiterhin wird der Einfluß der Systemgröße und verschiedener Seitenverhältnisse auf die Dynamik des Orientierungsfeldes studiert, wobei ein Wachstumsprozeß parallel zur Ausrichtung der Streifen identifiziert wird. Es zeigt sich, daß dieser Prozeß für die Nichtgleichgewichtsdynamik entscheidend ist. Zwei weitere Modelle für modulierte Phasen werden in ähnlicher Weise untersucht. Die Swift-Hohenberg-Gleichung in der Variante mit erhaltenem sowie nicht erhaltenem Ordnungsparameter zeigt ebenfalls Alterungseffekte in der Dynamik der Streifenorientierung. In einem System, welches zweidimensionale hexagonale Muster bildet, werden Alterungseffekte in der Autokorrelationsfunktion der Verschiebung beobachtet. Jedoch sättigt die zugehörige räumliche Korrelationslänge bei einem endlichen Wert, was auf eine Unterbrechung der Alterung hindeutet.

Schlagwörter: modulierte Phasen, Nichtgleichgewichtsdynamik, Alterung, Skalenverhalten, kritische Dynamik, weiche kondensierte Materie, Musterbildung, statistische Physik

TABLE OF CONTENTS

Non-equilibrium dynamics in a stripe-forming system

I. INTRODUCTION

Equilibrium statistical mechanics has been very successful in explaining a large number of phenomena, especially related to phase transitions [1–3]. However, the notion of equilibrium, upon which most of the theoretical understanding is based, turns out to be a rather idealized situation [4]. For concreteness, we focus on systems without external driving forces, coupled to a heat bath at a temperature T. In equilibrium, this setting corresponds to the canonical ensemble. Small perturbations close to an equilibrium state can be treated with linear response theory [3], and the system is expected to quickly return to equilibrium. However, no general formalism is available to explain the behavior encountered in systems far from equilibrium. Thus, a problem-spedific approach is necessary, and tools such as computer simulations have proven to be of great importance [5, 6]. Starting from equilibrium, a system can be brought out of equilibrium by a sudden change of a control parameter, e.g., the temperature, or by switching on an external field. Subsequently, a long or even infinite time may be necessary to re-establish equilibrium, depending on the nature of the equilibrium state the system is approaching. Such a slow relaxation can be found in a wide variety of systems [7]. One important class is given by glass-forming systems, which are well-known to exhibit such phenomena as aging, rejuvenation, and memory effects [8, 9]. The glass transition as well as its accompanying features are at the center of extensive and ongoing research [10]. In trying to understand the microscopic origin of glassy dynamics, much effort has been directed towards the study of disorder, which can be quenched, as in spin glasses [11, 12], or self-generated [13, 14]. On the other hand, it has been known for a long time that pure systems, which do not contain quenched randomness, may also exhibit a slow dynamics and particularly aging [15–17]. Examples are simple models for ferromagnets [18, 19] and other phase-ordering systems [16, 20, 21], where the observed dynamics can often be explained in

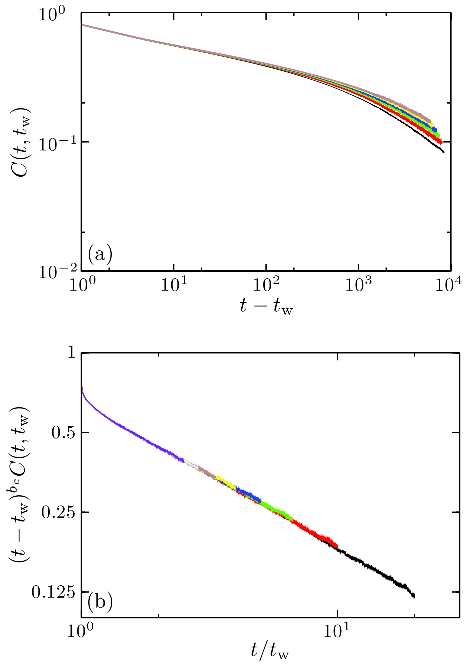

FIG. 1. Aging in the 2D Glauber-Ising model quenched to the critical temperature T_c. (a) The two-time autocorrelation function $C(t,t_w)$ is plotted as a function of $t-t_w$. The waiting time t_w increases from 1500 up to 4000 in steps of 500 (bottom to top). (b) The rescaled correlation function $(t-t_w)^{b_c}C(t,t_w)$ is plotted as a function of t/t_w. The values of t_w are the same as in (a). Adapted from Ref. 21.

terms of growing length scales [22]. To illustrate the aging effect, which is central to the present work, we present in Fig. 1 the two-time autocorrelation function $C(t,t_w)$ obtained from a ferromagnetic spin system quenched to the critical point [21]. While a more complete introduction to aging will be given in Sec. III A, the basic phenomenology of this effect can easily be identified: When plotted as a function of the time difference $t-t_w$, the correlation function $C(t,t_w)$ depends on the waiting time t_w. This is in contrast to the expected behavior in a stationary system, where $C(t,t_w)$ should be a function of $t-t_w$ only [21]. Another aspect of aging is demonstrated in Fig. 1(b), namely the scaling behavior inherent in $C(t,t_w)$. When the correlation function is rescaled by multiplication with a factor $(t-t_w)^{b_c}$, it depends only on the ratio t/t_w. The exponent b_c is specific to the system under consideration. Nevertheless, in the course of this work, we will encounter exactly the type of scaling demonstrated in Fig. 1.

In this thesis, we will investigate microphase-ordering systems, also called modulated phases [23]. They can take the form of stripes, lamellae, hexagonally ordered cylinders, as well as spatially more complex phases. Real-world examples for microphase-ordering systems are, e.g., block copolymers [24–26], thin magnetic films [27–30], electronic stripe phases [31, 32], Rayleigh-Bénard convection [33, 34], lipid bilayers [35], or patterns in chemical reactions [36, 37]. These systems possess at least one intrinsic, finite modulation length λ_0, which remains (mostly) constant in time. An additional length scale might be necessary to capture the degree of long-range order present in the system [38]. In contrast, most phase-ordering systems can be described by a single growing length scale, for instance the typical size of a domain. This length tends to infinity as the system orders [16]. The models we investigate here belong to the class $\mathrm{I_S}$ defined by Cross and Hohenberg [39], which means that the respective equilibrium state at zero temperature is periodic in space, but stationary in time.

In the main part of the present work, we study the evolution of a simple model for stripe formation under the influence of noise. Since the choice of the initial condition has a tremendous influence on the resulting dynamics, a few comments are in order. In numerical studies, the usual approach to investigating the dynamics of a phase-ordering system is to first prepare it in a suitable initial state. The temporal evolution after the start of the simulation, which mimics a change of the temperature, is then monitored. When considering the initial states of a system exhibiting a phase transition at a critical temperature T_c, at least two states stand out: The high-temperature homogeneous phase, which is observed as the temperature approaches infinity, and the completely ordered ground state at zero temperature. The evolution after a quench from an initial temperature $T_\mathrm{i} = \infty$ to a temperature $T_\mathrm{f} \leq T_\mathrm{c}$ has been addressed extensively in the literature [16, 40]. On the other hand, preparing the system in its ground state, corresponding to $T_\mathrm{i} = 0$, is less common [41–43]. The former approach often entails a dynamics dominated by topological defects and/or domain boundaries, as different ordered phases compete during the coarsening process [16]. Here, we will adopt the latter procedure, thus preparing the stripe-forming system in an ordered state corresponding to $T_\mathrm{i} = 0$ before performing an "up-quench", which mimics a jump to a temperature $T_\mathrm{f} < T_\mathrm{c}$. We present some illustrative examples for the different types of dynamics in Fig. 2 [44]. The model system as well as the free-energy density $\rho_\mathcal{F}$ and the orientational order parameter S will be properly introduced further below. Briefly, the free-energy density $\rho_\mathcal{F}$ acts as a driving force for the deterministic dynamics of the stripe-forming system, while the quantity

S indicates the degree of orientational order. $S = 0$ represents a disordered system, $S = 1$ in a completely ordered system. On the left-hand side [Fig. 2(a–c)], data for a quench from homogeneous initial conditions are shown in red. Even a long time after the start of the simulation, there are numerous topological defects still present in the system [Fig. 2(a)]. The free-energy density $\rho_{\mathcal{F}}$ decreases quickly at first, but its decline slows down at later times [Fig. 2(b)]. On the other hand, the orientational order parameter S remains close to zero for a long time, but finally approaches unity [Fig. 2(c). This indicates that the system consists of mostly parallel stripes and thus the onset of orientational order. The ordering process in stripe-forming systems we just described has been extensively studied in the literature [38, 45–52]. We will briefly address its aging properties in Sec. V.

We now turn to the case of ordered initial conditions, which is central to the present work. The corresponding results are shown in blue on the right-hand side of Fig. 2. As evident from Fig. 2(d), the stripe pattern becomes visibly perturbed as time progresses, but no topological defects appear. In contrast to the case of homogeneous initial conditions, the free-energy density $\rho_{\mathcal{F}}$ actually increases initially, but remains constant thereafter [Fig. 2(e)]. The apparent increase of fluctuations is an artifact of the logarithmic time scale. This indicates that the fluctuations seen in Fig. 2(d) have very low energy. Finally, the orientational order parameter S remains close to unity at all times, as expected for an ordered system [Fig. 2(f)]. Nevertheless, there is an ongoing decay, and the order parameter does not become stationary even at the latest times. Already from these preliminary data, we can conclude that the stripe-forming system evolving from ordered initial conditions exhibits a slow dynamics. This is despite the fact that one major obstacle on the way to equilibrium, namely the presence of topological defects, has been removed by our choice of initial conditions. The investigation of this phenomenon will be the major goal of the present work.

The remainder of this thesis is organized as follows: First, we introduce the model and define the quantities used to analyze its behavior (Sec. II). In Sec. III we present our main results concerning the dynamics of the orientation field when the stripe-forming system is relaxing from an ordered state. Sec. IV is devoted to the study of the influence of spatial confinement on that dynamics. The case of a quench from homogeneous initial conditions is briefly addressed in Sec. V.

In the second part of this thesis, we study a related stripe-forming system, namely the Swift-Hohenberg equation [53] (see Sec. VI), before turning to the dynamics of an ordered

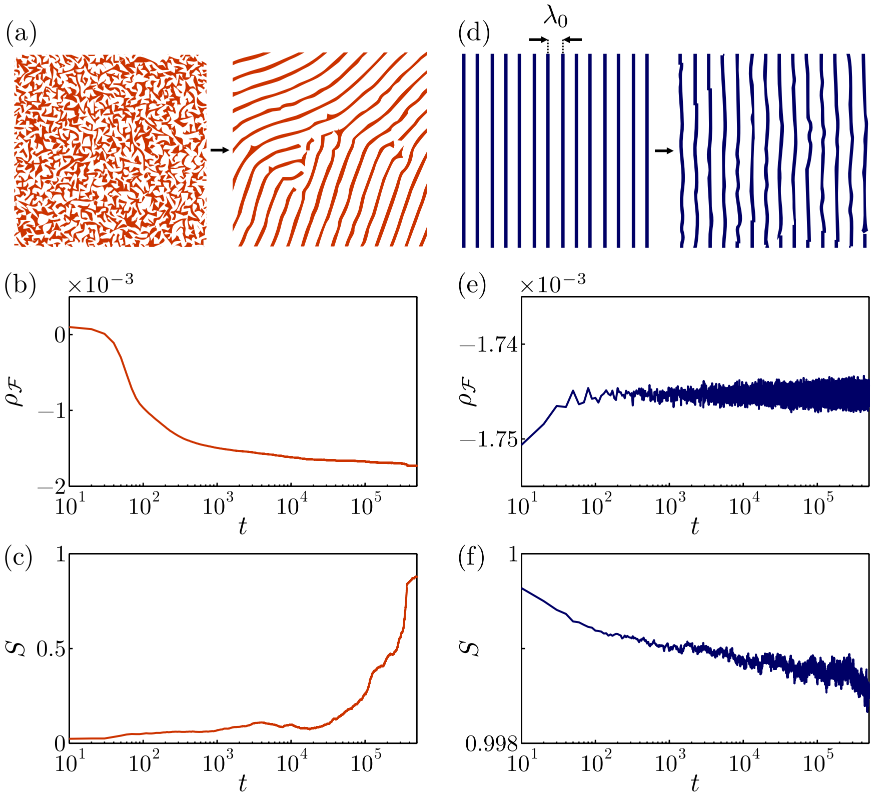

FIG. 2. Two types of slow dynamics in stripe patterns starting from different initial conditions: (a–c) homogeneous initial state, (d–f) striped initial state. (a) and (d) show binarized snapshots representing the corresponding dynamics of the concentration field. The free energy density $\rho_{\mathcal{F}}(t)$ decays slowly for homogeneous initial conditions (b), whereas it becomes stationary in the ordered system (e). During defect annihilation, the orientational order parameter S remains close to zero for a long time, but approaches unity at later times (c). In contrast, the ordered system exhibits a very slow but ongoing decay of orientational order (f). The noise strength $\eta/\eta_c = \frac{1}{30}$ in both cases. In (d), the wave length λ_0 is indicated. Adapted from Ref. 44.

hexagon-forming system, which provides an example for a modulated phase with a different symmetry (Sec. VII).

II. MODEL AND DATA ANALYSIS

A. Model B with Coulomb interactions

In this section, we briefly introduce the model, the simulation algorithm, and the data analysis techniques used in this work. The stripe-forming system we study is based on model B known from the theory of critical phenomena [54],

$$\frac{\partial \psi}{\partial t} = \nabla^2 \frac{\delta \mathcal{F}}{\delta \psi} + \zeta, \tag{1}$$

where $\psi(\mathbf{r}, t)$ is a scalar field representing the concentration difference $\psi_A - \psi_B$ of two species A and B. $\zeta(\mathbf{r}, t)$ is Gaussian white noise with zero mean and correlations $\langle \zeta(\mathbf{r}, t)\zeta(\mathbf{r}', t')\rangle = -2\eta\nabla^2\delta(\mathbf{r} - \mathbf{r}')\delta(t - t')$, with the parameter η controlling the noise strength. It remains to specify the free energy functional $\mathcal{F}$, which we write as follows:

$$\begin{aligned} \mathcal{F}[\psi] = & \int d^d r \left\{ -\frac{1}{2}\psi(\mathbf{r}, t)^2 + \frac{1}{4}\psi(\mathbf{r}, t)^4 + \frac{1}{2}\left[\nabla\psi(\mathbf{r}, t)\right]^2 \right\} \\ & + \frac{\Gamma}{2} \int \int d^d r' \psi(\mathbf{r}', t) G(\mathbf{r}, \mathbf{r}') \psi(\mathbf{r}, t) d^d r, \end{aligned} \tag{2}$$

with d being the spatial dimension, and the Green's function $G(\mathbf{r}, \mathbf{r}')$ defined by $\nabla^2 G(\mathbf{r}, \mathbf{r}') = -\delta(\mathbf{r} - \mathbf{r}')$. The first part of Eq. (2) is the usual Ginzburg-Landau free energy representing attractive interactions, whereas the second part describes repulsive long-range Coulomb interactions. This free energy has first been derived by Ohta and Kawasaki [55] in the context of block copolymer melts. It also arises in the context of Coulomb-frustrated ferromagnets [56–60], as well as in reactive binary mixtures [61] and a number of other systems [62]. Inserting Eq. (2) into Eq. (1) leads to the following stochastic partial differential equation:

$$\frac{\partial}{\partial t}\psi(\mathbf{r}, t) = \nabla^2\left[-\psi(\mathbf{r}, t) + \psi(\mathbf{r}, t)^3 - \nabla^2\psi(\mathbf{r}, t)\right] - \Gamma\psi(\mathbf{r}, t) + \zeta(\mathbf{r}, t). \tag{3}$$

For $\Gamma = 0$, Eq. (3) reduces to the Cahn-Hilliard equation used to describe spinodal decomposition in metallic alloys and other binary mixtures [16, 63]. with $\Gamma > 0$, Eq. (3) has been used as a simple model for the dynamics of microphase separation and the development of stripe order, both in block copolymers [38, 64–69] and in reactive binary mixtures [70, 71]. Without the noise term ($\eta = 0$), the system performs a gradient descent within the energy landscape given by Eq. (2) [65], whereas a finite value $\eta > 0$ simulates the coupling of the system to a noise source, e.g., a heat bath [54].

As mentioned before, most works in the literature devoted to the study of phase-separating systems address the dynamics after a quench from the high-temperature phase to a temperature $T < T_\mathrm{c}$. This is also the case for the stripe-forming system [38, 45–52]. However, quenches within the ordered phase have been investigated using a linear stability analysis [72]. Since our goal is to study the stripe-forming system in the ordered state, we use initial conditions of the form $\psi(\mathbf{r}, t = 0) = A\cos(2\pi/\lambda_0 r_\perp)$, where the amplitude $A = 2\sqrt{(1 - 2\sqrt{\Gamma})/3}$ and the wave length $\lambda_0 = 2\pi/\Gamma^{\frac{1}{4}}$ minimize the free energy, Eq. (2), in a single-mode approximation [71]. In this work, the two-dimensional vector $\mathbf{r} \equiv (r_\perp, r_\parallel)^\intercal$ has components referring to the directions perpendicular and parallel to the stripes, respectively. We fix the parameter $\Gamma = 0.2$ in all simulations, which is within the range $0 < \Gamma \leq \frac{1}{4}$ for which Eq. (3) exhibits stripe formation [38]. The value $\Gamma = 0.2$ leads to a sinusoidal concentration profile of $\psi(\mathbf{r}, t)$, which corresponds to the weak-segregation regime in the language of block copolymers [24]. The noise strength η is treated as an adjustable parameter. We mainly present data from simulations where $\eta = 1.39 \cdot 10^{-2}$, $6.94 \cdot 10^{-3}$, $6.94 \cdot 10^{-4}$, and $1.39 \cdot 10^{-4}$. For clarity, we will refer to these noise strengths as $\eta/\eta_\mathrm{c} = \frac{2}{3}, \frac{1}{3}, \frac{1}{30}$, and $\frac{1}{150}$, respectively. The critical noise strength $\eta_\mathrm{c} = 0.020(3)$ will be discussed in Section III E. We have performed computer simulations of Eq. (3) on a two-dimensional square lattice of size $L_\perp \times L_\parallel$, where $L_\perp = L_\parallel = L = 517$ in most cases. This value of the system size L has been chosen to be commensurate with the wavelength $\lambda_0 \approx 9.4$ of the stripe pattern. Time and space are discretized in steps of $\Delta t = 0.1$ and $\Delta x = 1$, respectively. We use a semi-implicit pseudo-spectral algorithm adapted from Ref. 73, which implies periodic boundary conditions. All spatial derivatives are computed in Fourier space and the time derivative is integrated using a backwards-differences scheme, which is third-order in our case. The corresponding first-order algorithm has been used before in simulations of Eq. (3), in both, a deterministic [74, 75] and a stochastic variant [76–78]. The details can be found in Appendix A, while a comparison with other algorithms is presented in Appendix B. All results have been averaged over 40 independent realizations, unless stated otherwise.

B. Local stripe orientation

In order to analyze the results of our simulations, we make use of the local orientation of the stripe patterns, which has become a standard method in recent years [38, 79–82].

We compute the orientation field $\theta(\mathbf{r}, t)$ from $\psi(\mathbf{r}, t)$ using the so-called gradient-square or structure tensor [83–85],

$$\mathbf{G} \equiv \nabla\psi \otimes \nabla\psi = \begin{pmatrix} \psi_\perp^2 & \psi_\perp\psi_\parallel \\ \psi_\perp\psi_\parallel & \psi_\parallel^2 \end{pmatrix}, \tag{4}$$

where the subscripts denote the partial derivatives $\partial\psi/\partial r_\perp$ and $\partial\psi/\partial r_\parallel$, respectively. The tensorial representation, which can also be generalized to higher dimensions [86–88], has several advantages. Because it is a quadratic form of the gradient, $\nabla\psi$ and $-\nabla\psi$ are mapped to the value of $\mathbf{G}$, as required by symmetry. Equivalently, this reflects that the orientation of a pattern (in rad) is only defined modulo π. Furthermore, the structure tensor enables averaging over a local neighborhood without cancellation effects. This is especially important at locations where the gradient vanishes (e.g., the valleys and ridges of a stripe pattern), and in the presence of noise. The orientation is given by the direction of the eigenvector of $\mathbf{G}$ associated with the largest eigenvalue. An equivalent expression can be obtained by introducing the double angle 2θ [85, 89]:

$$\tan(2\theta) = \frac{2\overline{\psi_\perp\psi_\parallel}}{\overline{\psi_\perp^2} - \overline{\psi_\parallel^2}}, \tag{5}$$

with the bars denoting the local average necessary for a robust estimation of the orientation. In this work, we use the algorithm described in Ref. 90. Its implementation in Fourier space matches the periodicity of our simulation data.

C. Correlation functions and order parameters

A major aspect of this work concerns correlation functions of the local stripe orientation. The orientation correlation function is defined as

$$C_\theta(\mathbf{r}, \mathbf{r}', t, t') \equiv \langle e^{2i(\theta(\mathbf{r}',t')} e^{-2i\theta(\mathbf{r},t)} \rangle_\zeta - \langle e^{2i\theta(\mathbf{r}',t')} \rangle_\zeta \langle e^{-2i\theta(\mathbf{r},t)} \rangle_\zeta, \tag{6}$$

where $\langle\cdot\rangle_\zeta$ stands for an average over independent noise realizations, and the double angles 2θ reflect the nematic symmetry of the stripe orientation, i.e., the aforementioned invariance with respect to rotations by π. Using this generic correlation function, we define the orientation autocorrelation function

$$C_\theta(t, t_\mathrm{w}) \equiv \mathrm{Re}\langle C_\theta(\mathbf{r}, \mathbf{r}, t, t_\mathrm{w}) \rangle_\mathbf{r} \tag{7}$$

and the spatial orientation correlation function

$$C_\theta(\mathbf{r},t) \equiv \mathrm{Re}\langle C_\theta(\mathbf{r}',\mathbf{r}'+\mathbf{r},t,t)\rangle_{\mathbf{r}'}. \tag{8}$$

The orientational order parameter $S \in [0,1]$ is defined as $S \equiv \left|\langle e^{2i\theta(\mathbf{r},t)}\rangle_{\mathbf{r}}\right|$. This is equivalent to the definition of the nematic order parameter used to describe liquid crystals [91]. Finally, we also consider the translational order parameter $U \in [0,1]$, which measures how well the stripe pattern conforms to a one-dimensional lattice. U is defined as follows:

$$U \equiv \left|\langle e^{i[\phi(\mathbf{r},t)-\phi_0(\mathbf{r})]}\rangle_{\mathbf{r},\zeta}\right|, \tag{9}$$

where $\phi(\mathbf{r},t)$ is the phase field obtained from the concentration field $\psi(\mathbf{r},t)$ by Fourier demodulation [92], and $\phi_0(\mathbf{r}) \equiv \mathbf{k}_0 \cdot \mathbf{r}$, with $\mathbf{k}_0$ the wave vector characterizing the pefect stripe pattern. This definition compares to the one used previously to extract the translational order parameter from stripe patterns, which requires localizing the center lines within the stripe pattern [81]. Nevertheless, our method yields almost identical values for U compared to the algorithm presented in Ref. 81 (data not shown).

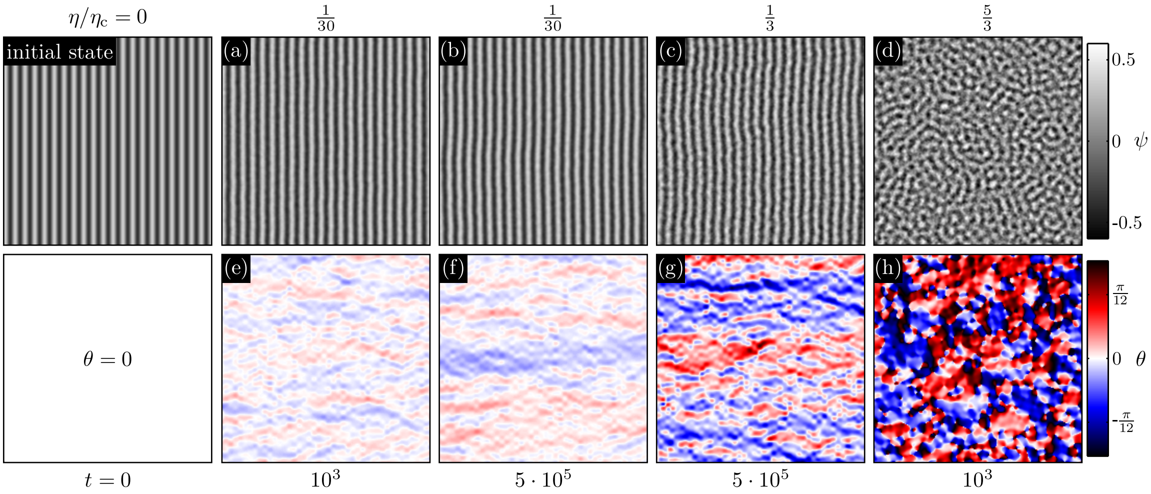

FIG. 3. Influence of the noise strength η and the simulation time t. (a–d) Concentration fields $\psi(\mathbf{r}, t)$ and (e–h) orientation field $\theta(\mathbf{r}, t)$ at different times t and noise strengths η. The outer left column shows the inital state of the system. Sections sized 200×200 of larger systems ($L = 517$) are shown. Note that in (h), the color scale ranges from $-\frac{\pi}{2}$ to $+\frac{\pi}{2}$.

III. EVOLUTION FROM AN ORDERED INITIAL STATE

In the following, we investigate the behavior of a stripe-forming system evolving from a perfectly ordered state under the influence of noise. The results presented in this section have been published in part in Ref. 44.

The impact of noise on ordered stripe patterns has been studied recently in the context of block copolymer films used as lithographic masks, where the interfacial roughness is of technological importance [77, 78, 93–95]. Nevertheless, the detailed dynamics of the relaxation, and specifically the dynamics of the stripe orientation, has not been addressed before. Fig. 3(a-d) displays some exemplary simulation results for the concentration field $\psi(\mathbf{r}, t)$ at different times t and for different noise strengths η. The initial configuration of the system $\psi(\mathbf{r}, t)$ is shown on the left. Visual inspection of the concentration fields shows a qualitative difference between systems where $\eta < \eta_c$ and the one where $\eta/\eta_c = \frac{5}{3}$ [Fig. 3(d)]. While $\psi(\mathbf{r}, t)$ exhibits ordered stripes in the former case, only very short stripe segments can be distinguished in the latter. Apparently, there is a critical noise strength $\eta = \eta_c$ which marks an order-disorder transition (ODT). While the ODT will be investigated in Sec. III E, we focus on the regime $\eta < \eta_c$ for the remainder of this section. A comparison of systems in the ordered state reveals increasing fluctuations of the stripes' shape and orientation when the noise strength is increased. In contrast, the influence of the simulation time is rather subtle [Fig. 3(a) and (b)], but becomes more obvious when the local stripe orientation $\theta(\mathbf{r}, t)$ is considered [Fig. 3(e-h)]. The morphology of the orientation field changes considerably with time, with elongate structures perpendicular to the stripes appearing at later stages of the evolution [Fig. 3(f)]. On the other hand, there is little difference in the morphology of $\theta(\mathbf{r}, t)$ for increasing noise strengths $\eta < \eta_{\mathrm{c}}$, except for an increase of the magnitude. Below, we will analyse the dynamics of the stripe-forming system in a more quantitative manner.

A. Aging

Aging is a non-equilibrium phenomenon associated with the time-dependent behavior of a system. It is one of the intriguing effects associated with glass formation [7, 9, 10]. On the other hand, it has long been recognized that non-glassy systems may also exhibit aging as part of their non-equilibrium dynamics [15, 22, 96]. Aging is often discussed using two-time correlation functions, although, depending on the system and the specific situation, two-time response functions may also be considered [8]. The generic autocorrelation function of an observable $A(\mathbf{r}, t)$ can be written as $C(t, t_{\mathrm{w}}) = \langle A(\mathbf{r}, t) A(\mathbf{r}, t_{\mathrm{w}}) \rangle_{\mathbf{r}}$, where the waiting time t_{w} is smaller than the observation time t. A system in equilibrium exhibits correlations of the form $C_{\mathrm{eq}}(t, t\mathrm{w}) = f(t - t_{\mathrm{w}})$, which reflects the invariance of the dynamics with respect to time translation. On the other hand, the correlation function explicitly depends on both, t and t_{w} in case of an aging system [97].

In the following, we briefly consider the autocorrelation function of the concentration field $\psi(\mathbf{r}, t)$ of the stripe-forming system, before focusing on orientation correlations. The two-time concentration autocorrelation function is given by

$$C_{\psi}(t, t_{\mathrm{w}}) \equiv \langle \psi(\mathbf{r}, t) \psi(\mathbf{r}, t_{\mathrm{w}}) \rangle_{\mathbf{r}, \zeta}. \tag{10}$$

We note that the average $\langle \psi(\mathbf{r}, t) \rangle_{\mathbf{r}}$ vanishes at all times.

To investigate possible aging effects in the dynamics of the stripe-forming system, we first plot the two autocorrelation functions $C_{\psi}(t, t_{\mathrm{w}})$ and $C_{\theta}(t, t_{\mathrm{w}})$ as a function of the time difference $t - t_{\mathrm{w}}$ for different waiting times t_{w} (Fig. 4). The results have been averaged over 40 independent realizations, except for those shown in Fig. 4(e) and (f), where 5

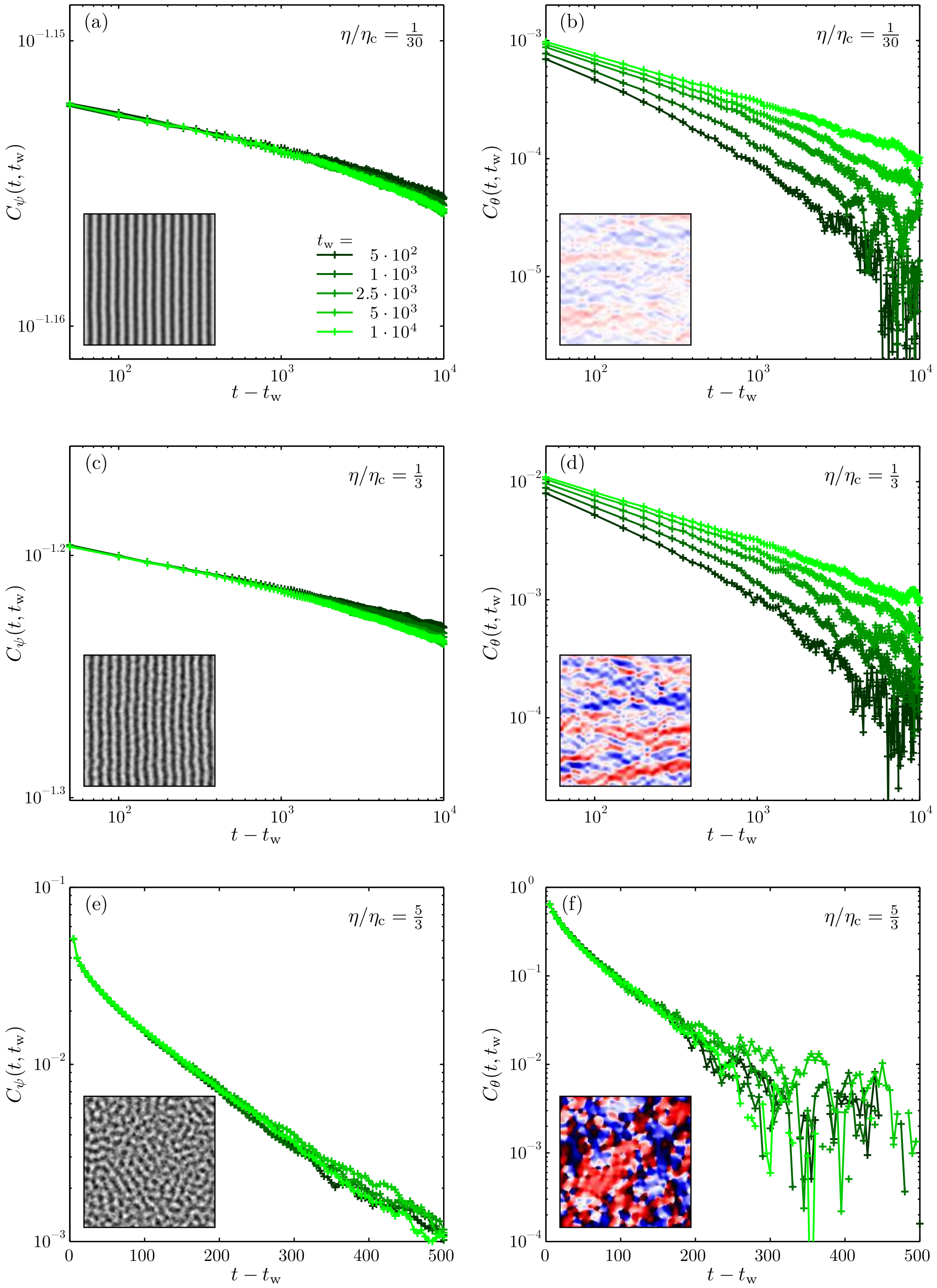

FIG. 4. Test for time translation invariance. The concentration autocorrelation function $C_\psi(t, t_w)$ (left column) and the orientation autocorrelation function $C_\theta(t, t_w)$ (right column) are plotted as a function of $t - t_w$. The waiting times $t_w = 5 \cdot 10^2$, 10^3, $2.5 \cdot 10^3$, $5 \cdot 10^3$, and 10^4 (dark green to bright green). Data for three different noise strengths $\eta/\eta_c = \frac{1}{30}$ (a, b), $\eta/\eta_c = \frac{1}{3}$ (c, d), and $\eta/\eta_c = \frac{5}{3}$ (e, f) are shown as indicated. The insets show examples of $\psi(\mathbf{r}, t)$, and $\theta(\mathbf{r}, t)$ for $t = 10^4$. The respective color scales are the same as in Fig. 3.

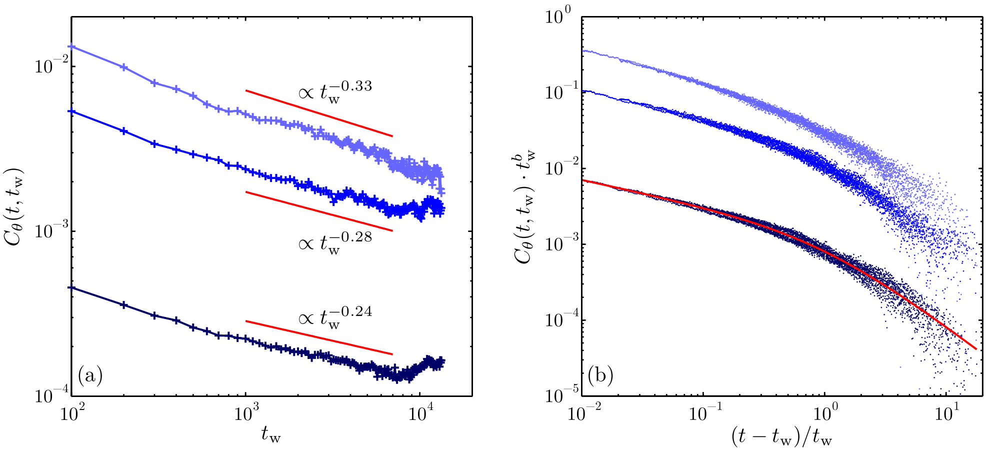

FIG. 5. Scaling form of the orientation autocorrelation function. (a) $C_\theta(t, t_\mathrm{w})$ plotted as a function of t_w for the ratio $t/t_\mathrm{w} = 3/2$. The noise strength $\eta/\eta_\mathrm{c} = \frac{2}{3}$, $\frac{1}{3}$, and $\frac{1}{30}$ (top to bottom). The straight red lines represent power laws with the indicated exponents. (b) The rescaled correlation function $C_\theta(t, t_\mathrm{w}) \cdot t_\mathrm{w}^b$ plotted as a function of $(t - t_\mathrm{w})/t_\mathrm{w}$. Data for the same noise strengths as in (a) are shown. The red line is a fit function described in the text.

realizations proved to be sufficient. Different noise strengths η below and above η_c yield a qualitatively different behavior of both correlation functions. Above the ODT, there is a fast relaxation of $C_\psi(t, t_\mathrm{w})$ and $C_\theta(t, t_\mathrm{w})$, which both decay as an exponential function of the difference $t - t_\mathrm{w}$ [Fig. 4(e) and (f)]. No dependence on the waiting time t_w is discernible. In contrast, the relaxation of both correlation functions is much slower below the ODT. The orientation correlation function $C_\theta(t, t_\mathrm{w}$ decays similarly to a power law of $t - t_\mathrm{w}$, whereas the concentration correlation function $C_\psi(t, t_\mathrm{w})$ exhibits an even slower decline, changing by only a few percent of the initial value within the range we consider. In case of the latter function, curves for different values of the waiting time t_w collapse almost perfectly [Fig. 4(a) and (c)]. Deviations only appear for the largest differences $t - t_\mathrm{w}$. On the other hand, $C_\theta(t, t_\mathrm{w})$ exhibits a pronounced dependence on the waiting time t_w [Fig. 4(b) and (d)]. The longer the waiting time, the slower the relaxation we observe.

To summarize, the two-time correlation functions $C_\psi(t, t_\mathrm{w})$ and $C_\theta(t, t_\mathrm{w})$ decay rapidly above the ODT ($\eta > \eta_\mathrm{c}$), but slowly in the ordered phase ($\eta < \eta_\mathrm{c}$). Only $C_\theta(t, t_\mathrm{w})$ exhibits a significant dependence on the waiting time t_w. In the following, we will therefore focus on the aging of the orientation autocorrelation function $C_\theta(t, t_\mathrm{w})$ in the ordered phase. A common scaling form for the autocorrelation function of an aging system is given by [18, 19, 21]

$$C(t, t_\mathrm{w}) \propto t_\mathrm{w}^{-b} \cdot f(t/t_\mathrm{w}), \tag{11}$$

where b is a non-negative exponent, and $f(t/t_\mathrm{w})$ is a scaling function. Usually, $b = 0$ in systems which are quenched from a temperature $T_\mathrm{i} = \infty$ to $T_\mathrm{f} < T_\mathrm{c}$, and $b > 0$ if $T_\mathrm{f} = T_\mathrm{c}$ [97], where T_c is the critical temperature. In order to test the scaling form given by Eq. (11), we first plot $C_\theta(t, t_\mathrm{w})$ as a function of the waiting time t_w while keeping the ratio t/t_w constant. The results for $t/t_\mathrm{w} = 3/2$ and different noise strengths η are shown in Fig. 5(a) on a log-log plot. $C_\theta(t, t_\mathrm{w})$ decays as a power law of t_w for all three values of η. In order to extract the exponent b, we have fitted the data in the interval $10^3 \leq t_\mathrm{w} \leq 7 \cdot 10^3$, resulting in $b = 0.24$, 0.28, and 0.33 for $\eta/\eta_\mathrm{c} = \frac{1}{30}$, $\frac{1}{3}$, and $\frac{2}{30}$, respectively. This constitutes a very weak dependence of the exponent b on the noise strength, considering that the noise strength varies over more than one order of magnitude. Fig. 5(b) shows the rescaled correlation functions $C_\theta(t, t_\mathrm{w}) \cdot t_\mathrm{w}^b$ as a function of $(t - t_\mathrm{w})/t_\mathrm{w}$. This choice for the abscissa allows for distinguishing the large number of data points obtained for $t/t_\mathrm{w} \approx 1$. There is a collapse of the data onto individual curves for each noise strength, thereby confirming the scaling relation, Eq. (11). We are now able to determine the scaling function $f(t/t_\mathrm{w})$. Regarding its functional form, we propose two candidates, a stretched exponential $f_1(x) \propto \exp[-\alpha_1(x-1)^{\beta_1}]$ and a product of two power laws $f_2(x) \propto x^{-\alpha_2}(x-1)^{-\beta_2}$. Fitting these functions to the data for $\eta/\eta_\mathrm{c} = \frac{1}{30}$ yields the parameters $\{\alpha_1 = 3.4, \beta_1 = 0.22\}$ and $\{\alpha_2 = 0.89, \beta_2 = 0.34\}$, respectively. Both functions fit the data equally well within the available range of t/t_w, whereas clearly distinguishing the two functions would require data for $t/t_\mathrm{w} \gg 10^2$. However, there is an argument in favor of f_2 being the correct scaling function. For large arguments t/t_w, f_2 exhibits the power-law decay found in other phase-ordering systems [18]. We note that this behavior is also used to define the autocorrelation exponent λ_C [97, 98].

In this section, we have established that there is aging in the dynamics of the stripe orientation. The scaling form we found, Eq. (11) with an exponent $b > 0$, is typical for critical systems [97]. The fact that we observe this type of scaling at low noise strengths which are far away from the order-disorder transition, might seem surprising. However, there are other systems which are critical not only at an isolated point, but for a whole range of temperatures. Most notable is the XY model in two dimensions [99–101]. Its non-equilibium dynamics has been studied in Refs. [41, 42], including quenches from ordered initial conditions, where aging

with a scaling form according to Eq. (11) was found. Furthermore, while the scaling function $f(t/t_{\mathrm{w}})$ is different than the one we observe, it decays as a power law for large arguments [41], which is typical for phase-ordering systems in general [97].
In the following chapters we will report on further evidence for critical behavior of the stripe-forming system, and compare it to the XY model where appropriate.

B. Spatial correlations, defects, and late-stage properties

In the preceding section, we have demonstrated aging in the stripe-forming system by investigating the two-time autocorrelation function of the orientation. A more complete understanding of the dynamics of the stripe-forming system requires taking into account spatial correlations as well. This will be the focus of the first part of the present section. Second, we investigate the influence of topological defects, which, while absent from the initial state, may be generated by the noise. Third, while aging is by definition a non-equilibrium effect, it is instructive to monitor the behavior of the system as it evolves towards equilibrium in order to understand the origin of the observed phenomena. While an equilibrium state could in principle be attained by evolving Eq. (3) until the system becomes stationary, we will see in the following that this cannot be done with reasonable computational effort. Therefore, the results presented in this section constitute only an approximation to the equilibrium behavior of the stripe-forming system. Nevertheless, we will be able to draw some valuable conclusions regarding its properties.

1. Spatial orientation correlations

As it turns out, the anisotropic nature of the ordered stripe pattern, which arises from the concentration field being modulated only in one dimension, is also reflected by the shape of the spatial orientation correlation function $C_\theta(\mathbf{r}, t)$. At this point, we recall that $\mathbf{r} \equiv (r_\perp, r_\parallel)^\intercal$. In Fig. 6, a portion of the full two-dimensional function is plotted. It is clear from a visual inspection that the fluctuations of the stripe orientation are more correlated horizontally (in the $r_\perp$ direction, see the regions shaded in red) than vertically (in the $r_\parallel$ direction). Therefore, a separate discussion of the behavior of $C_\theta(\mathbf{r}, t)$ in the directions perpendicular and parallel

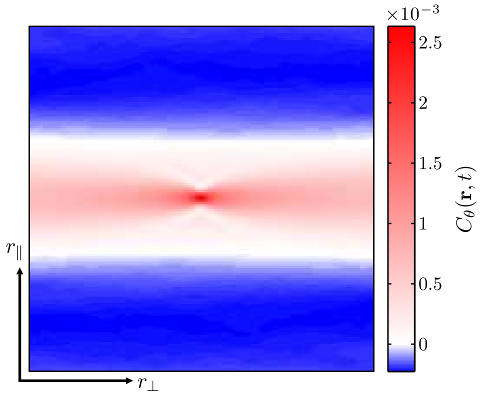

FIG. 6. Anisotropy of the spatial orientation correlation function. The central part (size 200 × 200) of $C_\theta(\mathbf{r}, t)$ is shown for $t = 5 \cdot 10^5$ and $\eta/\eta_c = \frac{1}{30}$.

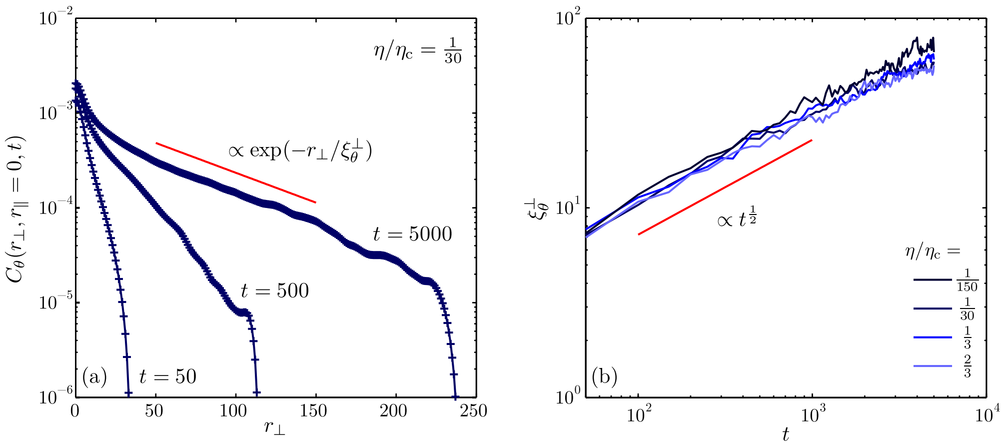

FIG. 7. Evolution of the orientation correlation length. (a) Cuts through the spatial orientation correlation function $C_\theta(\mathbf{r}, t)$ perpendicular to the stripe pattern for times $t = 50$, 500, and 5000. The red line represents an exponential $\propto \exp(-r_\perp/\xi_\theta^\perp)$. (b) The orientational correlation length $\xi_\theta^\perp$ is plotted as a function of time for different noise strengths. The red line is a power law with the exponent $\frac{1}{2}$ drawn as a guide to the eye.

to the stripes is necessary.

We first focus on the perpendicular direction. In Fig. 7(a), $C_\theta(r_\perp, r_\parallel = 0, t)$ is shown on a semi-logarithmic scale at different times $t \leq 5 \cdot 10^3$ for $\eta/\eta_c = \frac{1}{30}$. Within this range, the correlation function decays approximately as an exponential function of the distance $r_\perp$ for $r_\perp \gtrsim \lambda_0$. The temporal evolution suggests the presence of a growing correlation length. We have extracted the time-dependent orientational correlation length ξ_θ by fitting $C_\theta(r_\perp, r_\parallel = 0, t)$ with an exponential $\propto \exp(-r_\perp/\xi_\theta^\perp)$. The resulting values of $\xi_\theta^\perp$ are plotted

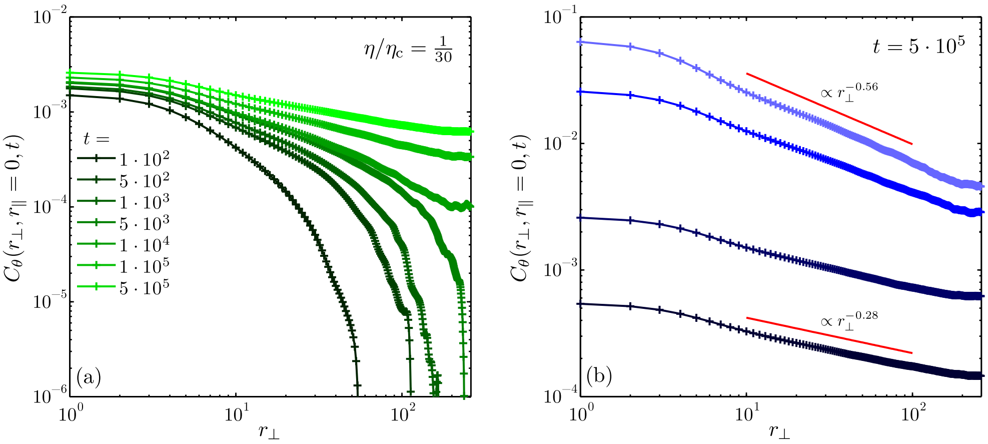

FIG. 8. Cross-over and late-stage behavior. (a) Evolution of $C_\theta(\mathbf{r}, t)$ in the direction parallel to the stripes. Data are shown for times $t = 10^2$, $5 \cdot 10^2$, 10^3, $5 \cdot 10^3$, 10^4, 10^5, and $5 \cdot 10^5$ (bottom to top). (b) $C_\theta(r_\perp, r_\parallel = 0, t)$ is plotted at time $t = 5 \cdot 10^5$ for noise strengths $\eta/\eta_c = \frac{1}{150}$, $\frac{1}{30}$, $\frac{1}{3}$, and $\frac{2}{3}$ (bottom to top). The red lines represent power laws with the indicated exponents.

for different noise strengths in Fig. 7(b). $\xi_\theta^\perp$ is independent of the noise strength and grows with time as a power law with an exponent close to $\frac{1}{2}$. Growth laws with this exponent are well-known from non-conserved phase-ordering dynamics in various systems [16].

We now consider the spatial correlation function at later times. An example for the evolution of $C_\theta(r_\perp, r_\parallel = 0, t)$ is presented in Fig. 8(a) on a log-log scale. There is a qualitative change in the shape of the curves, which proceeds over more than three decades of time and possibly continues at even later times than we consider here. While correlations are short-range at early times, $C_\theta(r_\perp, r_\parallel = 0, t)$ decays as a power law $\propto r_\perp^{-c}$ at late times $t \gtrsim 10^5$ for spatial separations $r_\perp > 10$. We use this decay to define the spatial exponent c. Power-law behavior is observed over a wide range of noise strengths, including data for the very low noise strength $\eta/\eta_c = \frac{1}{150}$, as shown in Fig. 8. It is easy to see that the exponent increases with the noise strength, with $c = 0.28$ at $\eta/\eta_c = \frac{1}{150}$ and $c = 0.56$ at $\eta/\eta_c = \frac{2}{3}$. This dependence on η will be discussed in more detail in Sec. III D.

In contrast to the behavior perpendicular to the stripes, orientation correlations parallel to the stripes remain short-range at all times. This is demonstrated in Fig. 9(a), where $C_\theta(r_\perp = 0, r_\parallel, t)$ is shown at different times t for a noise strength $\eta/\eta_c = \frac{1}{30}$. The correlation function decays rapidly within about one period of the stripe pattern. Furthermore, no pronounced evolution with time is visible, except for an overall shift of the curves. In

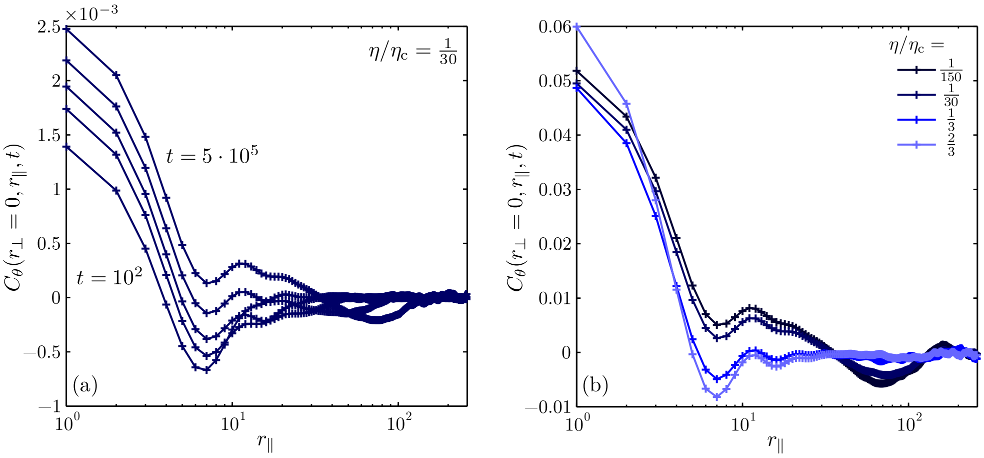

FIG. 9. Spatial correlations parallel to the stripes. (a) Temporal evolution of the correlation function $C_\theta(r_\perp = 0, r_\parallel, t)$ for the noise strength $\eta/\eta_c = \frac{1}{30}$. Data are shown for times $t = 10^2$, 10^3, 10^4, 10^5, and $5 \cdot 10^5$ (bottom to top). (b) Comparison of $C_\theta(r_\perp = 0, r_\parallel, t)$ at $t = 5 \cdot 10^5$ for noise strengths $\eta/\eta_c = \frac{1}{150}, \frac{1}{30}, \frac{1}{3}$, and $\frac{2}{3}$. In (b), the data have been rescaled using constant factors as explained in the text.

Fig. 9(b), we compare the orientation correlation function parallel to the stripes at late times t for different noise strengths. For clarity, the curves for $\eta/\eta_c = \frac{1}{150}, \frac{1}{30}$, and $\frac{1}{3}$ have been multiplied by factors of 100, 20, and 2, respectively. $C_\theta(r_\perp = 0, r_\parallel, t)$ decays quickly for $r_\parallel < 10$, with all curves exhibiting a local minimum followed by a maximum in this region. For larger separations, the curves for the two highest noise strengths remain close to zero, while $C_\theta(r_\perp = 0, r_\parallel, t)$ possesses another minimum at $r_\parallel \approx 70$ in case of the two lowest noise strengths. We do not offer an interpretation of these features, but merely note the stark contrast to the decay of the orientation correlations perpendicular to the stripes. We will revisit some aspects of the behavior of $C_\theta(\mathbf{r}, t)$ parallel to the stripes in Sec. IV.

To summarize, we have found perpendicular to the stripes (1) an orientational correlation length growing as a power-law at early times, and (2) a cross-over to power-law decay of the spatial correlation function at late times. These features are reminiscent of the features observed in critical dynamics [19, 97]. In contrast, $C_\theta(\mathbf{r}, t)$ remains short-range parallel to the stripes at all times.

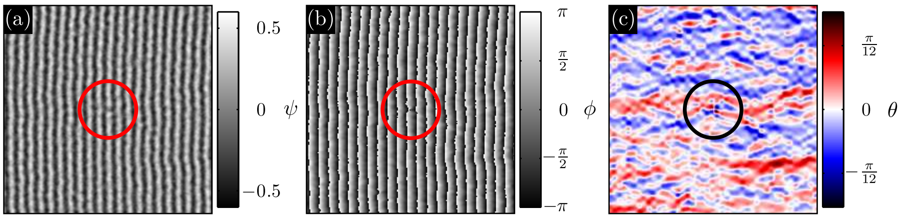

FIG. 10. A pair of dislocations in a system where $\eta/\eta_\mathrm{c} = \frac{1}{3}$ at $t = 2 \cdot 10^5$. (a) Concentration field $\psi(\mathbf{r}, t)$. (b) Phase $\phi(\mathbf{r}, t)$ used to identify the topological defects. (c) Stripe orientation $\theta(\mathbf{r}, t)$. The dislocations have been marked with a circle.

2. *Topological defects*

When a stripe-forming system is prepared in a perfectly ordered state, it contains by definition no topological defects. However, such defects might be induced during a subsequent evolution at a finite temperature. In our model, flucutations are introduced through the noise term $\zeta(\mathbf{r}, t)$ with the strength η. To understand the dynamics of the system, it is necessary to investigate the role of topological defects, which are known to be associated with the slow evolution observed after a quench from a homogeneous initial state [38, 51, 52]. To this end, we have computed the dislocation density ρ_Disloc, using a procedure described previously [92, 102]. Briefly, the phase $\phi(\mathbf{r}, t)$ is obtained from $\psi(\mathbf{r}, t)$ by Fourier demodulation. Defects are then identified by performing path integrals [39, 81, 102, 103] enclosing each lattice point. If such an integral evaluates to a non-zero integer multiple of 2π, this indicates a phase singularity, and the corresponding lattice point is counted as a defect. An example of this procedure is shown in Fig. 10. The density ρ_Disloc is finally computed as the number of defects divided by the system size. In Fig. 11, we show data only for two noise strengths ($\eta/\eta_\mathrm{c} = \frac{1}{3}$ and $\frac{2}{3}$). Below $\eta/\eta_\mathrm{c} = \frac{1}{3}$, we did not observe any defects at all, given the system size we consider. In fact, Figs. 10 and 11 show that dislocation are very rare already at the latter noise strength, as the maximum values of ρ_Disloc correspond to just two dislocations identified within 40 different realizations. On the other hand, a finite density of dislocations is always present in systems where $\eta/\eta_\mathrm{c} = \frac{2}{3}$. Aside from fluctuations, ρ_Disloc does not change over time. Furthermore, there is no qualitative change in the behavior of systems with and without dislocations ($\eta/\eta_\mathrm{c} < \frac{1}{3}$) with respect to the aging effect and the spatial orientation correlations, as we have seen in the previous section. Therefore, we conclude that dislocations are not crucial for the dynamics of the ordered stripe-forming system. The

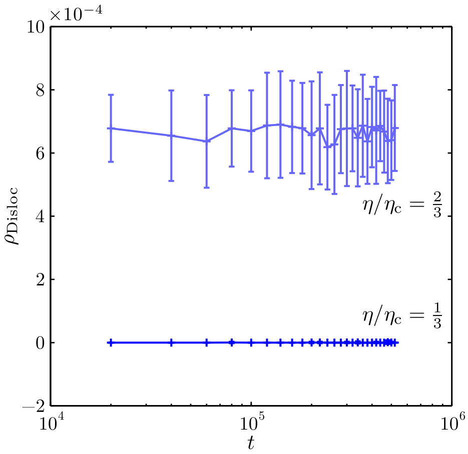

FIG. 11. Late-stage evolution of the density of defects ρ_{Disloc} for noise strengths $\eta/\eta_{\mathrm{c}} = \frac{1}{3}$ and $\frac{2}{3}$. The error bars indicate the standard deviation over 40 independent realizations.

observed dynamics is determined by excitations other than topological defects (see Fig. 3). This is in contrast to the theory of 2D smectics presented in Ref. 104, which predicts that dislocations are excited at all finite temperatures. The presence of dislocations leads to the destruction of orientational order and brings about power-law spatial orientation correlations, like in a nematic. The cited theory describes the equilibrium state and addresses length scales much larger than the distance between two dislocations. In our simulations, the linear dimension of the systems we consider is necessarily much smaller than the latter distance at low noise strengths. More importantly, it turns out that there are also qualitative differences between the dislocations we observe and those predicted to occur in two-dimensional smectic systems [104]. In Fig. 10(a), we show an example of two dislocations in a system where $\eta/\eta_{\mathrm{c}} = \frac{1}{3}$ and defects occur only at a very low density. However, as the system has a higher degree of order, the dislocations are more easily identified. From a visual inspection of the concentration field $\psi(\mathbf{r}, t)$, it is clear that the defect merely consists of a ruptured stripe, which leaves two open ends. While this configuration is topologically equivalent to two dislocations with opposite winding number [39], it only leads to a local perturbation of the stripe pattern. In contrast, a free dislocation usually consists of either an interstitial or a missing stripe, forcing the pattern to adapt on larger length scales. Such a dislocation could be created by unbinding, i.e., spatial separation, of the two defects depicted in Fig. 10, but we do not observe such a process in our simulations. The stripe orientation $\theta(\mathbf{r}, t)$ provides further evidence for the localized impact of topological defects on the stripe-forming system

[Fig. 10(c)]. The large-scale, correlated structures typically found in $\theta(\mathbf{r}, t)$ at late times are clearly visible, whereas the perturbation caused by the two defects is restricted to a small region with a diameter on the order of one wave length λ_0. This is in clear contrast to the perturbation of the orientation field caused by an isolated dislocation, which decays only algebraically perpendicular to the stripes [104].

To conclude, a finite density of topological defects (in the form of dislocations) is observed in the stripe-forming system, which increases with the noise strength. In the ordered state, dislocations occur as tightly bound pairs. There is no slow dynamics associated with defect creation, and the effect on the properties of the system, specifically the orientation dynamics, is negligible due to their localized nature. This stands in contrast with the theory of 2D smectics [104].

3. Late-stage properties

We now investigate additional properties of the stripe-forming system at late times, such as the evolution of different order parameters and of the free energy, and also the associated probability distributions. In Fig. 12(a, b), we present the temporal evolution of the orientational order parameter S and the translational order parameter U. As the systems in question are highly ordered, we plot the deficiency of the order parameters with respect to unity for reasons of clarity. These quantities increase as the system becomes less ordered. In Fig. 12(a), the evolution of $1 - S$ is shown. Orientational order is decreasing very slowly, which results in $1 - S$ growing in a fashion consistent with a power law with a very small exponent. In contrast, the translational order parameter U [Fig. 12(b)] is decreasing much faster, which leads to a more rapid growth of $1 - U$. The shape of $1 - U$ resembles a power law, the exponent of which apparently depends on the noise strength η, with larger values observed at smaller noise strengths. However, the variations between different realizations are rather large, resulting in noisy time series of $1 - U$ and making it difficult to assess its true dependence on time. The evolution of both, orientational and translational order parameters is still progressing at the latest times which we have explored, a further indication that the stripe-forming system remains out of equilibrium.

The free energy density $\rho_{\mathcal{F}} \equiv \mathcal{F}[\psi]/L^2$, obtained by numerically evaluating Eq. (2), is plotted

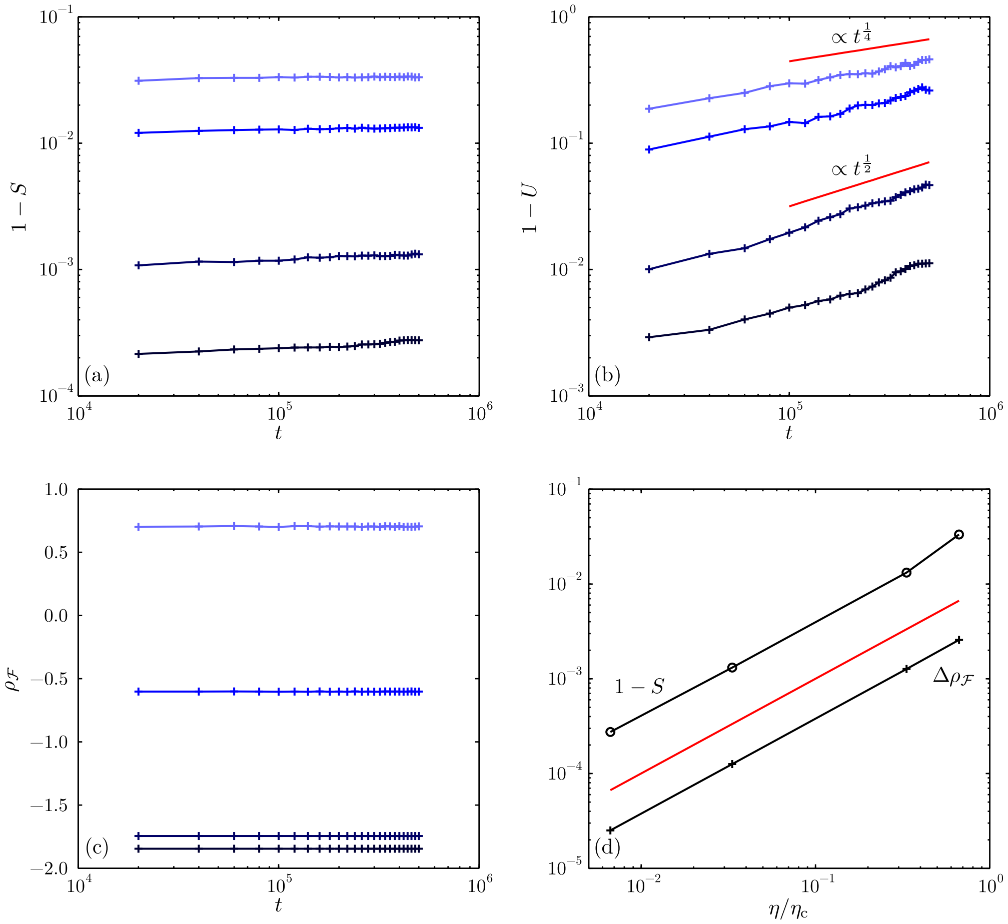

FIG. 12. Late-stage evolution of order parameters. (a–c) Temporal evolution of the orientational order parameter S, the translational order parameter U and the free energy density $\rho_{\mathcal{F}}$, respectively. The noise strength $\eta/\eta_{\mathrm{c}} = \frac{1}{150}, \frac{1}{30}, \frac{1}{3}$, and $\frac{2}{3}$ (bottom to top). The straight red lines in (b) are power laws drawn as guides to the eye. (d) Scaling of S and $\Delta\rho_{\mathcal{F}}$ with the noise strength η. Data are shown for $t = 5 \cdot 10^{5}$. The straight red line represents a linear dependence on η.

in Fig. 12(c). In contrast to the behavior of the two order parameters, the free energy density is stationary throughout the time range considered here. This indicates that the processes responsible for the dynamics at late times are quite subtle and are driven by entropic rather than by energetic forces.

Our results for the order parameters at late times can be compared to the theoretical findings of Ref. 104 regarding the different types of order in a two-dimensional stripe system. While orientational order was found to be persistent in the absence of dislocations, translational order is destroyed in this case by phonons alone, with phonons referring to excitations of the stripe pattern other than topological defects. Only when the effects of dislocations are included, orientational order is destroyed as well [104]. The pronounced and ongoing decay of the translational order parameter U we observe in systems with few or no dislocations is consistent with the predicted strong effect of phonon-like fluctuations on translational order. The orientational order parameter S decays comparatively slowly, but does not reach a stationary value either. This is not too surprising, as any kind of broken continuous symmetry is forbidden in two dimensions at finite temperatures [105, 106]. However, the presence of a finite value of the order parameter in finite-size systems, even if it should be zero in an infinite system, is to be expected. For example, the dependence of the magnetization on the system size can be explicitly calculated for the 2D XY model [107]. The mechanisms responsible for destroying long-range order, in this case spin waves, only have an effect on gigantic length scales.

In light of the very slow evolution of the orientational order parameter, we investigate the influence of varying the noise strength η by assuming S to be stationary at late times. For purposes of comparison, we define the excess free energy density $\Delta\rho_{\mathcal{F}} \equiv (\mathcal{F}[\psi] - \mathcal{F}_0)/L^2$, where $\mathcal{F}_0$ is the ground state free energy obtained by evolving a system with ordered initial conditions at $\eta = 0$ until no further decrease is observed. The effect of varying the noise strength is demonstrated in Fig. 12(d), where $1 - S$ and $\Delta\rho_{\mathcal{F}}$ are plotted as a function of η/η_{c}. It is clear that both, the free energy and the orientational order parameter scale linearly with increasing noise strength. The small deviations in $1 - S$ for $\eta/\eta_{\mathrm{c}} = \frac{2}{3}$ are probably due to the finite density of dislocations, which cause additional distortions of the orientation field $\theta(\mathbf{r}, t)$.

Up to this point, we have computed the averages of different quantities X characterizing the stripe-forming system. A more complete description can be obtained by considering the probability density function $p(X)$. If X is a spatially averaged quantity, one might expect $p(X)$ to be Gaussian by appealing to the central limit theorem [109]. We will see below that Gaussian distributions do indeed occur in many, but not all cases. In the following, we will neglect a possible dependence of $p(X)$ on time and focus solely on the latest times accessed in our simulations.

First and foremost, we will study the distribution of the orientational order parameter, $p(S)$. This is motivated by several studies [108, 110] which showed that a number of different systems, such as turbulent flows and critical ferromagnets, exhibit fluctuations described by

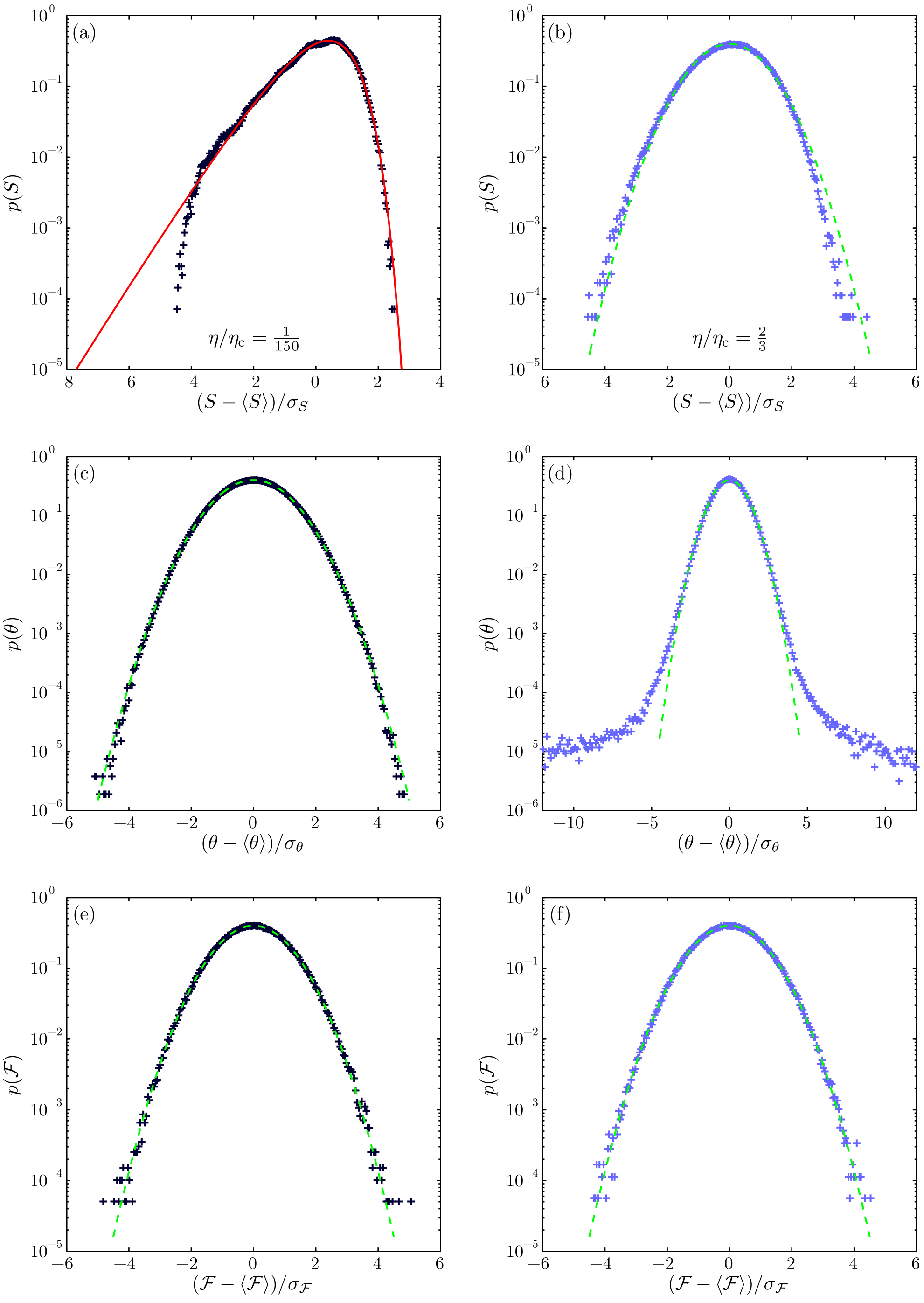

FIG. 13. Probability distributions of the orientational order parameter S (a, b), the stripe orientation θ (c, d), and the free energy $\mathcal{F}$ (e, f) for two different noise strengths ($\eta/\eta_c = \frac{1}{150}$, left column, and $\eta/\eta_c = \frac{2}{3}$, right column). The red line in (a) is the BHP distribution [108], while the dashed green lines in the remaining panels are Gaussians with zero mean and unit variance. The data have been gathered for $5 \cdot 10^5 \leq t \leq 6 \cdot 10^5$ in case of S and $\mathcal{F}$, and for $t = 5 \cdot 10^5$ in case of θ.

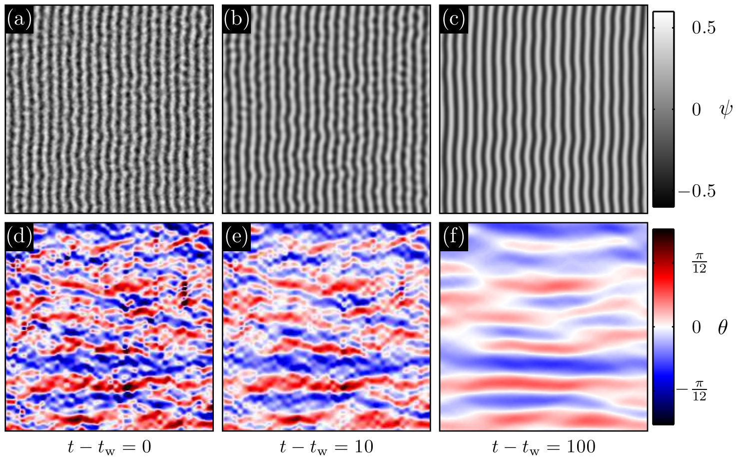

FIG. 14. Illustration of the effects of quenching to $\eta = 0$. The concentration field $\psi(\mathbf{r}, t)$ (a–c) and the orientation field $\theta(\mathbf{r}, t)$ (d–f) are shown for $t_{\rm w} = 5 \cdot 10^5$ and $t - t_{\rm w} = 0$, 10, and 100, respectively.

an approximately universal distribution. Common to those systems is the presence of strong correlations, for instance due to the proximity to a critical point. The distribution in question, the so-called BHP distribution, can be analytically derived for the XY model in the spin-wave approximation [111]. It is asymmetric with respect to the mean, decays rapidly for values larger than the average and features an asymptotically exponential tail for small values [112]. We plot the probability density as a function of the reduced quantity $(S - \langle S \rangle)/\sigma_S$, which results in a distribution with zero mean and unit variance. For comparison, we have also computed the probability density functions of the stripe orientation θ and of the free energy $\mathcal{F}$. The results are presented in Fig. 13, where the left (right) column contains data for $\eta/\eta_{\rm c} = \frac{1}{150}$ ($\eta/\eta_{\rm c} = \frac{2}{3}$). These two noise strengths are far away from and rather close to the order-disorder transition, respectively. In the former case, the function $p(S)$ is very well described by the BHP distribution for $(S - \langle S \rangle)/\sigma_S$ close to zero, while deviations occur for very small values. In Fig. 13(b), it becomes apparent that close to the ODT, the shape of $p(S)$ has changed, now being almost Gaussian with only a small asymmetry remaining. For values of η between $\frac{1}{150}$ and $\frac{2}{3}$, we observe a cross-over of the distribution $p(S)$ (data not shown). In contrast to that of the orientational order parameter, the distributions of both, the stripe orientation $p(\theta)$ and free energy density $p(\mathcal{F})$ exhibit a Gaussian shape over the whole range of noise strengths considered here [Fig. 13(c, d) and (e, f), respectively]. The deviations in the tails of $p(\theta)$ for $\eta/\eta_{\rm w} = \frac{2}{3}$ [Fig. 13(d)] arise because of a wrap-around of the orientation, which is confined to the interval $(-\pi/2, \pi/2]$.

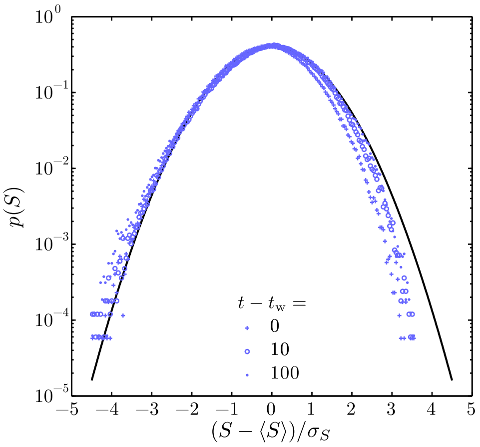

FIG. 15. Influence of quenches to $\eta = 0$ on the probability distribution $p(S)$ for $\eta/\eta_\mathrm{c} = \frac{2}{3}$. Data are shown for different times $t - t_\mathrm{w}$ after the quench: $t - t_\mathrm{w} = 0$ (+, no quench), $t - t_\mathrm{w} = 10$ (∘), and $t - t_\mathrm{w} = 100$ (•). The black line is a Gaussian with zero mean and unit variance.

The qualitative change of the distribution $p(S)$ as a function of the noise strength for $\eta < \eta_\mathrm{c}$, i.e., within the ordered phase, is rather unexpected. Up to this point, we have only observed quantitative changes upon varying the noise strength η. Furthermore, the XY model, for which the BHP distribution has been derived [111], exhibits the same order parameter distribution for all temperatures below the Kosterlitz-Thouless temperature T_KT [112], while it approaches a Gaussian form above [113]. The mechanism leading to the characteristic fluctuations in the XY model are spin waves, which are essentially a long-wavelength phenomenon [114]. Comparing the morphology of stripe patterns at different noise strengths [see Fig. 3(b) and (c)], the main visible effect of higher values of η are increased short-wavelength fluctuations and the appearance of topological defects. One might get the idea that these excitations suppress and/or interfere with long-wavelength fluctuations responsible for the observed behavior of $p(S)$ at very low noise strengths. In order to test this hypothesis, we have re-evaluated $p(S)$ for $\eta/\eta_\mathrm{c} = \frac{2}{3}$, while also quenching each configuration to $\eta = 0$ for a time $t - t_\mathrm{w}$ before computing the orientational order parameter S. As a rationale for our approach based on quenching the stripe pattern to eliminate short-wavelength fluctuations, we present in Fig. 14 examples for concentration fields $\psi(\mathbf{r}, t)$ and orientation fields $\theta(\mathbf{r}, t)$ as a function of the time $t - t_\mathrm{w}$ after the quench. This demonstrates that already a short quench time leads to a visible straightening and smoothing of the stripes. No topological defects remain at $t - t_\mathrm{w} = 100$ [Fig. 14(a–c)]. Small-scale orientation fluctuations decay quickly, but the large-scale structure of the orientation field remains the same for a long period of time [Fig. 14(d–f)]. The results for the distribution of the orientational order parameter are shown in Fig. 15 for three values of the quench time $t - t_{\mathrm{w}}$. Surprisingly, the changes in $p(S)$ upon quenching are minimal, with the overall shape remaining close to a Gaussian. The distribution decreases slightly faster for larger values of the reduced order parameter $(S - \langle S \rangle)/\sigma_S$, but this effect actually seems to vanish for larger $t - t_{\mathrm{w}}$. Thus, the cause for the variation of the distribution $p(S)$ as a function of the noise strength η remains an open question. A more in-depth discussion of the effects of quenching stripe patterns to $\eta = 0$ will be presented in the next section.

C. Quenches to $\eta = 0$

The model we investigate, Eq. (1), consists of a deterministic part, which represents a gradient descent within the energy landscape given by Eq. (2), and a stochastic noise term $\zeta(\mathbf{r}, t)$ controlled by the noise strength η. When a system which has evolved at $\eta > 0$ for some time t_{w} is subjected to further evolution without noise, it is said to be quenched to $\eta = 0$ (see Fig. 14 for an example). If we imagine the configuration of the system at time t_{w} as a point in configuration space, it will subsequently move towards the nearest minimum of the free energy [65]. We have performed such quenches for two reasons: First, they elucidate the structure of the free energy landscape the ordered stripe system evolves on. Previous investigations have revealed a glass transition in stripe- and lamellae-forming systems related to the emergence of exponentially many metastable states, i.e., local minima of the free energy [115–118]. Such minima should result in an arrest of the dynamics of Eq. (1) after a quench. Indeed, it has been demonstrated that for quenches from a homogeneous initial state and sufficiently small noise strengths the pinning of defects can cause stripe-forming systems to become stuck in states without long-range order [51]. Second, studying the non-equilibrium dynamics after a quench is interesting in its own right, and also enables a comparison to the behavior of other systems.

We note that the quench procedure we apply is similar in principle to the investigation of inherent structures [119, 120] in molecular glass formers, such as a binary Lennard-Jones fluid [121]. Such a system can be defined as a set of particles, interacting through a pair potential which depends on the distance between two particles. The time-dependent configuration is given by the locations and momenta of the particles. The inherent structure is obtained from a gradient descent within the potential energy landscape, starting from the current position of each particle, while neglecting the momenta. One can then describe the dynamics of the system as a series of transitions between different inherent structures. We note that many different configurations may be mapped to the same inherent structure, depending on its basin of attraction within the energy landscape.

We first address the relaxation of the orientation autocorrelation function $C_\theta^{\mathrm{Q}}(t, t_{\mathrm{w}})$ after a quench to $\eta = 0$. In Fig. 16(a), we plot $C_\theta^{\mathrm{Q}}(t, t_{\mathrm{w}})$ as a function of the time difference $t - t_{\mathrm{w}}$, where the noise has been switched off at time $t_{\mathrm{w}} = 5 \cdot 10^5 = \mathrm{const.}$ For a wide range of noise strengths ($\eta/\eta_{\mathrm{c}} = \frac{1}{150}, \frac{1}{30}, \frac{1}{3}$ and $\frac{2}{3}$), there is a slow relaxation, similar to a power law of $t - t_{\mathrm{w}}$. The exponent depends on the noise strength, but also seems to vary with time. For comparison, we show the quantity $C_\theta^{\mathrm{Q}}(t, t)$, which is related to the orientational order parameter through $C_\theta^{\mathrm{Q}}(t, t) \equiv 1 - S^2(t)$. The dependence of $C_\theta^{\mathrm{Q}}(t, t)$ on $t - t_{\mathrm{w}}$ closely follows that of the two-time correlation function. This shows that the relaxation of the stripe orientations after the quench is mainly driven by the order parameter S approaching unity. We have also investigated the influence of the time t_{w}, which is the duration of the system's evolution at a noise strength $\eta > 0$. A waiting time of $t_{\mathrm{w}} = 5 \cdot 10^5$ corresponds to a late stage of the orientation dynamics (see Fig. 8). In Fig. 16(b), we compare $C_\theta^{\mathrm{Q}}(t, t_{\mathrm{w}})$ for an earlier time $t_{\mathrm{w}} = 2 \cdot 10^4$ and for $t_{\mathrm{w}} = 5 \cdot 10^5$ at initial noise strengths $\eta/\eta_{\mathrm{c}} = \frac{1}{30}$ and $\frac{1}{3}$, respectively. A longer waiting time results in a slower relaxation for both noise strengths. In Fig. 16(b), we have additionally plotted the individual realizations from which the average $C_\theta^{\mathrm{Q}}(t, t_{\mathrm{w}})$ is computed. This ensemble exhibits a growing spread as $t - t_{\mathrm{w}}$ increases. Therefore we focus on the range $100 \leq t - t_{\mathrm{w}} \leq 1000$, where we have measured the quench exponent b_{Q} by fitting $C_\theta^{\mathrm{Q}}(t, t_{\mathrm{w}})$ with a power law $\propto (t - t_{\mathrm{w}})^{-b_{\mathrm{Q}}}$. The value of b_{Q} as a function of the noise strength η will be reported in Sec. III D.

As noted before, when the stripe system described by Eq. (3) evolves at vanishing noise strength $\eta = 0$, it is driven solely by the tendency to minimize the free energy, $\mathcal{F}$ [65]. Therefore, it is useful to investigate this quantity in order to understand the relaxation process. In Fig. 16(c) and (d), we plot the excess free energy density $\Delta\rho_{\mathcal{F}}$ as a function of $t - t_{\mathrm{w}}$, computed from the same data set as in (a) and (b). There is a slow dynamics, as in the case of the orientation correlations, for all noise strengths we consider. The overall shape of the free energy curves for intermediate times again resembles a power law $\propto (t - t_{\mathrm{w}})^{-d_{\mathcal{F}}}$,

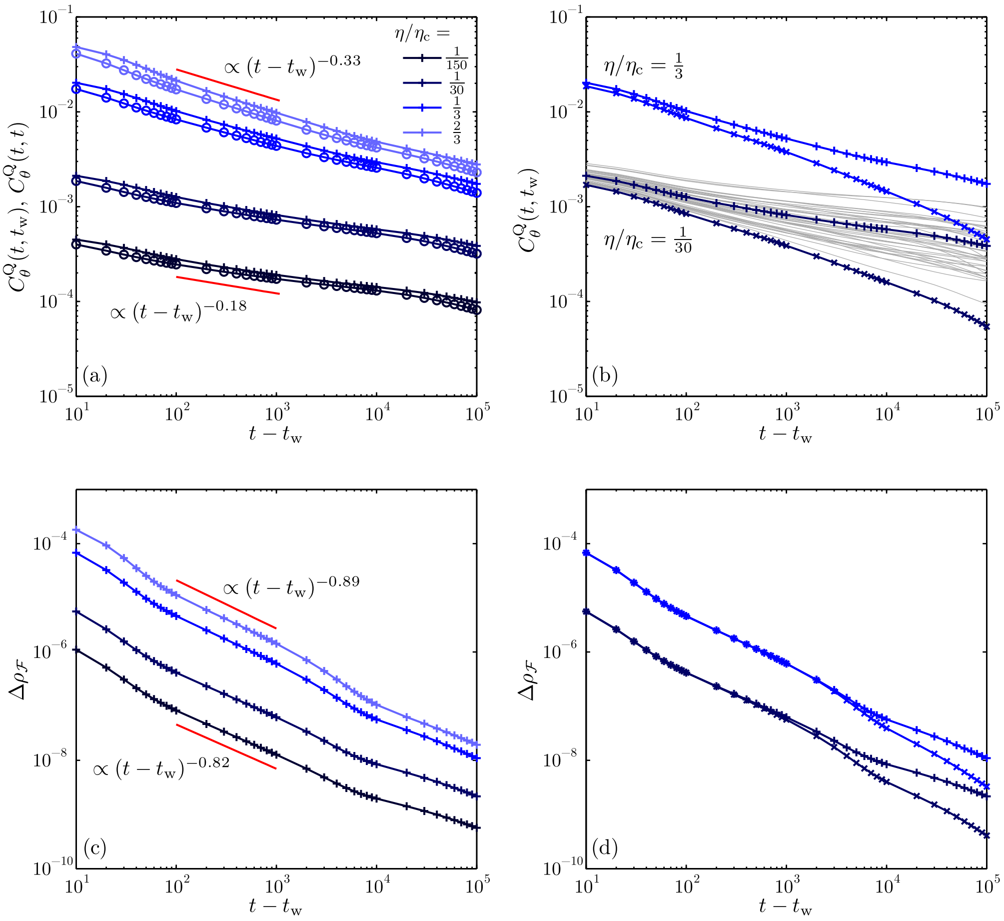

FIG. 16. Quench dynamics for different initial noise strengths η. In panels (a) and (b), the orientation autocorrelation function $C_\theta^{\mathrm{Q}}(t,t_{\mathrm{w}})$ (+) is plotted as a function of the time $t-t_{\mathrm{w}}$ after a quench at $t_{\mathrm{w}} = 5\cdot10^5$. Additionally, $C_\theta^{\mathrm{Q}}(t,t)$ (∘) is shown in panel (a). In panel (b), $C_\theta^{\mathrm{Q}}(t,t_{\mathrm{w}})$ is also plotted for $t_{\mathrm{w}} = 2\cdot10^4$ (×). The thin gray lines represent the ensemble of independent realizations over which the average $C_\theta^{\mathrm{Q}}(t,t_{\mathrm{w}})$ for $\eta/\eta_{\mathrm{c}} = \frac{1}{30}$ is computed. In panels (c) and (d), the excess free energy density $\Delta\rho_{\mathcal{F}}$ is shown as a function of $t-t_{\mathrm{w}}$. The red lines in (a) and (c) represent power laws with the indicated exponents. In (d), data for noise strengths $\eta/\eta_{\mathrm{c}} = \frac{1}{30}$ and $\frac{1}{3}$ are shown for waiting times $t_{\mathrm{w}} = 5\cdot10^5$ (+) and $2\cdot10^4$ (×).

with the exponent $d_{\mathcal{F}}$ close to unity. However, there are several pronounced kinks as time progresses. Notably, increasing the initial noise strength η causes only a shift in the magnitude of the curves, but preserves their detailed shape. In Fig. 16(d), we study the influence of the waiting time t_{w} by comparing $\Delta\rho_{\mathcal{F}}$ for $t_{\mathrm{w}} = 2\cdot10^4$ and $5\cdot10^5$. There are no discernible differences in the relaxation of the free energy for times $t-t_{\mathrm{w}} \lesssim 2\cdot10^3$. From then on, the

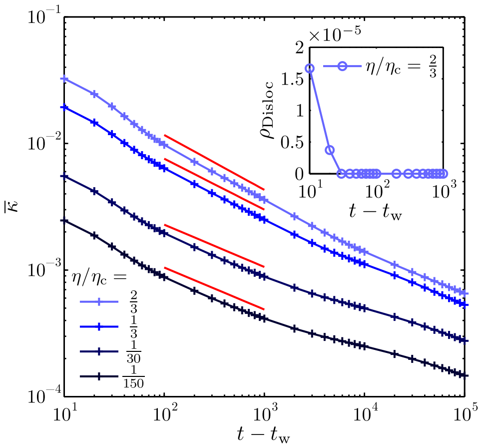

FIG. 17. Evolution of the average curvature $\overline{\kappa}$ after a quench to $\eta = 0$ at time $t_\mathrm{w} = 5 \cdot 10^5$. Data for four initial noise strengths are shown. The red lines are power laws with exponents obtained by fitting the data in the indicated range. The inset shows the defect density ρ_Disloc as a function of $t - t_\mathrm{w}$.

free energy decreases faster in the systems which had evolved at a finite noise strength for a shorter time $t_\mathrm{w} = 2 \cdot 10^4$. As in the case of the orientation correlation function, the longer the waiting time t_w, the slower the relaxation after a quench becomes.

Another potentially useful quantity for charaterizing the quench dynamics is the stripe curvature. In our case, the curvature can be thought of as the inverse of the local radius of a bent stripe. The local curvature has been used to investigate the properties of stripe patterns before. In Refs. 122–124, experimental data obtained from flow patterns were analyzed, while simulation results were considered in Refs. [50, 51, 125]. For a further discussion of the stripe curvature, see Ref. 82.

Here, we compute the curvature field $\kappa(\mathbf{r}, t)$ from the concentration field $\psi(\mathbf{r}, t)$ using the algorithm presented in Ref. 90. The authors present two approaches based on locally modeling the input data as either a parabolic or a circular shape. We have used the latter, but found no significant differences between the two variants when applied to our data. As the curvature can be both, positive and negative, the average curvature is defined as $\overline{\kappa}(t) \equiv \sqrt{\langle \kappa(\mathbf{r}, t)^2 \rangle_\mathbf{r}}$. Our investigation of the curvature is motivated by some theoretical results in the literature concerning the relaxation of stripe patterns [38, 45, 46]. In Refs. 45 and 46 it was found that curved stripes described by the Swift-Hohenberg equation [53] exhibit two regimes during their relaxation, with a power law $\sim t^{-\frac{1}{4}}$ observed at early times and a faster relaxation

$\sim t^{-\frac{1}{2}}$ dominating at late times. In a subsequent work, the same result was derived also for model B with Coulomb interactions [38]. Although both efforts were intended to explain the dynamics after a quench from homogeneous initial conditions (see Sec. V), they do not incorporate the influence of topological defects. Thus, quenching ordered stripe systems to $\eta = 0$ might more closely match the situation addressed by the theory.

In Fig. 18, $\overline{\kappa}$ is shown as a function of $t - t_{\mathrm{w}}$. The average curvature decays slowly, similar to the quantities discussed in the preceding paragraphs. There is also a considerable scatter across the ensemble of realizations (data not shown), similar to the variations in the orientation correlation function $C_\theta^{\mathrm{Q}}(t, t_{\mathrm{w}})$ seen in Fig. 16. Nevertheless, there is no sign of a cross-over to a faster relaxation. Rather, the relaxation seems to slow down for larger values of $t - t_{\mathrm{w}}$. We have fitted power laws $\propto (t - t_{\mathrm{w}})^{-d_\kappa}$ to the data within the range $100 \leq t - t_{\mathrm{w}} \leq 1000$, resulting in exponents d_κ between 0.33 and 0.43. Their dependence on the noise strength will be discussed in the next section. To sum up, the average stripe curvature exhibits a slow relaxation after a quench to $\eta = 0$, which can be described by a power law at least for intermediate ranges of $t - t_{\mathrm{w}}$. However, we find no sign of a two-stage relaxation. Furthermore, the observed exponents depend on the initial noise strength and do not match the values predicted theoretically [38, 46].

The inset in Fig. 17 shows the dislocation density ρ_{Disloc} as a function of the time after the quench for $\eta/\eta_{\mathrm{c}} = \frac{2}{3}$. It is clear that even for the highest noise strength we consider, the system is free of dislocations for $t - t_{\mathrm{w}} \geq 30$, showing that topological defects play no role in the slow relaxation observed after a quench.

We now investigate the evolution of spatial correlation functions after a quench to $\eta = 0$. In Fig. 18, we show the spatial orientation correlation function $C_\theta^{\mathrm{Q}}(\mathbf{r}, t)$ for different times $t - t_{\mathrm{w}}$ after the quench from the initial noise strength $\eta/\eta_{\mathrm{c}} = \frac{1}{30}$. Perpendicular to the stripes, the power-law decay observed as a result of the evolution at finite noise strength quickly disappears [Fig. 18(a)]. For $t - t_{\mathrm{w}} \gtrsim 10^3$, $C_\theta^{\mathrm{Q}}(\mathbf{r}, t)$ is virtually constant in the $r_\perp$ direction, while the relaxation of the order parameter is still progressing, leading to an overall decrease of the correlation function. In the $r_\parallel$ direction, $C_\theta^{\mathrm{Q}}(\mathbf{r}, t)$ retains some features, with a distinct minimum at $r_\parallel \approx 100$ still present at the latest quench times $t - t_{\mathrm{w}}$ [Fig. 18(b)].

The spatial orientation correlation function, although very useful for describing the dynamics of the stripe patterns at finite noise strength, has proven less revealing in case of the quenches to $\eta = 0$. Its evolution seems to be driven mainly by the growth of the order parameter, as

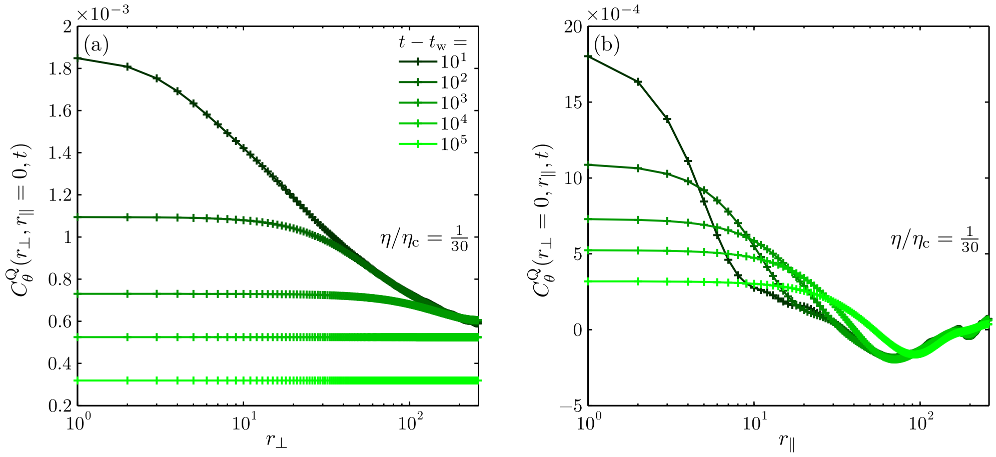

FIG. 18. Relaxation of the spatial orientation correlation function $C_\theta^{\mathrm{Q}}(\mathbf{r}, t)$ after a quench to $\eta = 0$ in the directions (a) perpendicular and (b) parallel to the stripes.

the system slowly approaches a perfectly ordered state. While there is an ongoing evolution of the correlation function in the $r_\parallel$ direction, even at very late times after the quench, we found no evidence of scaling behavior. In the Appendix C, we will briefly report on the dynamics of the structure factor of the orientation (see Sec. IV) after a quench to $\eta = 0$.

We will now give a short summary of the results from the quench experiments. The stripe system exhibits a slow dynamics when quenched to $\eta = 0$ after an initial time t_{w} spent at a finite noise strength $\eta < \eta_{\mathrm{c}}$. This is evident from the evolution of both, the orientation autocorrelation function and the free energy density, which decrease as power laws in the time $t - t_{\mathrm{w}}$ after the quench. The longer the waiting time t_{w}, the slower the subsequent relaxation becomes. Although the dynamics slows down as $t - t_{\mathrm{w}}$ increases, we do not observe any signs for an arrest of the evolution within the time span studied here. While the data shown cover times after the quench up to $t - t_{\mathrm{w}} = 10^5$, we have checked this result in longer simulations, with $t - t_{\mathrm{w}}$ reaching 10^6 in some instances.

The slow but continuing evolution provides evidence against the presence of many local minima in the free energy landscape given by Eq. (2), at least in those regions of configuration space corresponding to an ordered state. Our conclusion is corroborated by a visual inspection of configurations $\psi(\mathbf{r}, t)$ for long quench times $t - t_{\mathrm{w}}$ (see Fig. 14), where we only see an ever closer approach to an unperturbed stripe pattern. The picture changes completely when performing quenches from homogeneous initial conditions, representing a high-temperature mixed state [38, 45, 49, 51, 52]. This situation will be discussed in Sec. V.

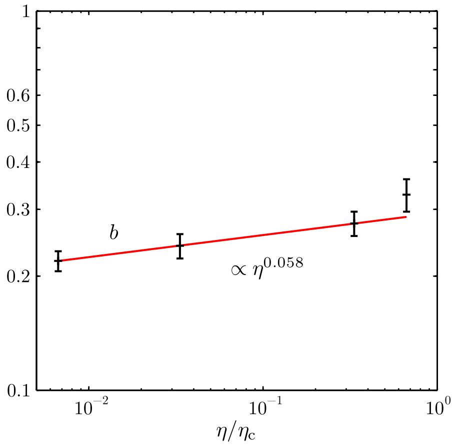

FIG. 19. The exponent b describing the power-law decay of the orientation autocorrelation function $C_\theta(t, t_w)$ is plotted as a function of the noise strength on a log-log scale. The red line is a power law drawn as a guide to the eye. Due to the large scatter in the $C_\theta(t, t_w)$ data, the error bars are based on the goodness-of-fit statistics using the averaged curves.

The perhaps counter-intuitive slow relaxation we observe can also occur in other systems with a simple energy landscape and a continous symmetry, prominently the XY model at low temperatures. Rutenberg and Bray have calculated the angular autocorrelation function for quenches within the spin-wave phase below T_{KT} [126]. For quenches to a final temperature $T = 0$, they found a power-law decay, $C_{XY}(t, t_w) \sim (t - t_w)^{-\eta_{XY}/4}$, with η_{XY} the critical exponent describing the decay of spatial correlations in equilibrium. This relates the behavior of the autocorrelation function after a quench to the decay of the quasi-long range spatial correlations in equilibrium. It will be interesting to check if such a relation also exists for the stripe-forming system. This will be part of the next section.

D. Exponents and scaling relations

We conclude our discussion of the dynamics of ordered stripe patterns in this chapter by comparing the different exponents we have obtained so far, taking into account their behavior as a function of the noise strength η. In Fig. 19, the exponent b obtained from the decay of the orientation autocorrelation function $C_\theta(t, t_w)$ is shown as a function of η. This is the result of fitting the data presented in Fig. 5(a), together with additional data for $\eta/\eta_c = \frac{1}{150}$. For the lowest three values of η/η_c, the exponent b seems to grow as a power law $\propto \eta^{0.058}$,

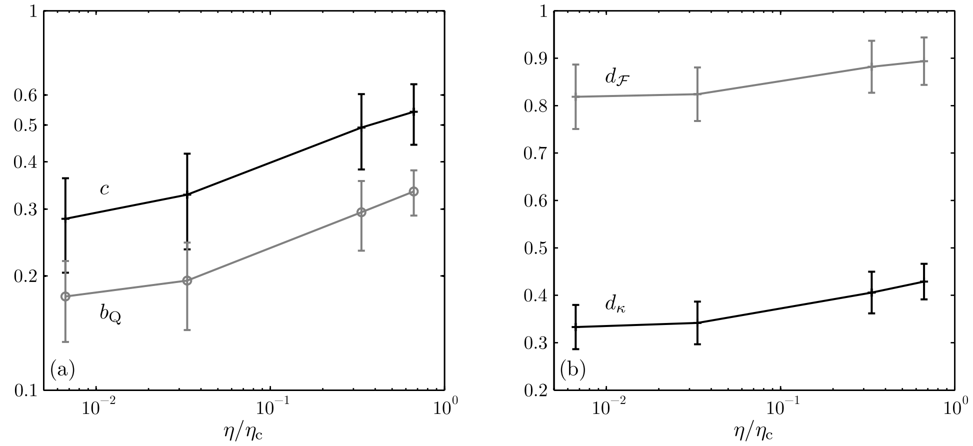

FIG. 20. Exponents extracted from the stripe-forming system as a function of the noise strength. (a) The exponents c, determined from $C_\theta(r_\perp) \sim r_\perp^{-c}$, and b_Q, defined by $C_\theta^\mathrm{Q}(t, t_\mathrm{w}) \sim (t - t_\mathrm{w})^{-b_\mathrm{Q}}$, are shown on a log-log plot. The shift in magnitude between the two curves is consistent with a factor $\approx 5/3$. (b) Exponents $d_\mathcal{F}$ and d_κ obtained by fitting the decay after a quench of the excess free energy density $\Delta\rho_\mathcal{F}$ and the average curvature $\overline{\kappa}$, respectively, are shwon on a lin-log plot. The error bars indicate the standard deviation computed over 40 realizations.

whereas b attains a larger value for the highest noise strength $\eta/\eta_\mathrm{c} = \frac{2}{3}$. This deviation might be explained with the appearance of topological defects at higher noise strengths, which in turn leads to a faster decay of $C_\theta(t, t_\mathrm{w})$. However, due to the large scatter across different realizations of $C_\theta(t, t_\mathrm{w})$ the error bars reported in Fig. 19 should be regarded as a lower bound of the uncertainty of b. Furthermore, more data points are needed to firmly establish the dependence of b on η which we have just outlined. Nevertheless, it is obvious that this dependence is only a weak one, with the exponent b increasing by just 50% as the noise strength is increased by two orders of magnitude. This is in contrast to the low-temperature behavior of the XY model, where $b \equiv \eta_{XY}/2$ [41], and a linear dependence of the critical exponent η_{XY} on the temperature is found [41, 42, 100].

We now investigate the relation between temporal and spatial orientation correlations. The exponent b_Q characterizing the two-time correlation function $C_\theta^\mathrm{Q}(t, t_\mathrm{w})$ after a quench to $\eta = 0$ together with the exponent c describing the decay of the spatial orientation correlations at finite noise strengths η is plotted as a function of η in Fig. 20(a). As revealed by the double-logarithmic plot, the two exponents agree remarkably well up to a constant factor $\approx \frac{5}{3}$. This demonstrates a causal link between the spatial orientation correlations of an inital configuration and the temporal dynamics during a subsequent quench. It seems that the long-range correlated structures present for large values of t_{w}, as described by the exponent c, impede the ability of the system to quickly relax to a state consisting of completely ordered stripes. Furthermore, from Fig. 14 it is clear that those long-wavelength modulations of the orientation field survive for the longest time after the quench.

Another aspect of the dynamics after a quench to $\eta = 0$ is presented in Fig. 20(b). The exponents $d_{\mathcal{F}}$ and d_{κ} extracted from the evolution of the excess free energy density $\Delta\rho_{\mathcal{F}}$ and the average curvature $\overline{\kappa}$, respectively, are shown on a lin-log plot as a function of η. The former ($d_{\mathcal{F}}$) takes on values between 0.8 and 0.9, while the latter (d_{κ}) lies between 0.33 and 0.45. Both exponents depend only weakly on the noise strength effective before the quench.

The results presented in Figs. 19 and 20 suggest that there are at least three distinct sets of exponents necessary to describe the static and dynamic properties of the stripe pattern at finite noise strength. The exponent b describing the decay of $C_{\theta}(t, t_{\mathrm{w}})$ grows by about 50% as the noise strength is varied over two orders of magnitude. A possible power-law dependence is observed for low noise strengths. In contrast, the quench exponent b_{Q} and the spatial exponent c presented in Fig. 20(a) approximately double over the same range of noise strengths. They exhibit a different dependence on η than the exponent b and seem to be related by a constant factor. Lastly, the exponents characterizing the decay after a quench to $\eta = 0$ of the excess free energy density and of the average curvature only increase by about 10% and 30% over the same range of noise strengths, respectively [Fig. 20(b)]. Furthermore, the latter exponents seem to be related by an additive constant ≈ 0.47, rather than by a factor, as is the case for b_{Q} and c. However, due to the large error bars, the data in this case are also consistent with the exponents not depending on the noise strength at all.

E. Noise-induced order-disorder transition

We have already mentioned the existence of an order-disorder transition (ODT) which occurs at a critical value of the noise strength η. Although the focus of this work is on stripe systems in the ordered state where $\eta < \eta_{\mathrm{c}}$, we will briefly address the properties of the ODT in the following section.

Equilibrium phase transitions and critical phenomena are well-understood areas of physics [3, 54, 127]. In the literature, there are several results relevant to stripe-forming systems, e.g., the seminal works of Brazovskiĭ [128] and Swift and Hohenberg [53]. It was found that the transition from a uniform to a modulated state is first-order, rather than second order as predicted by mean-field theory, due to the influence of fluctuations. These predictions were later confirmed experimentally for lamellae-forming block copolymers [129, 130]. Several numerical works on the nature of the transition have also been performed [131–134].

However, the aforementioned phase transition is not identical to the noise-induced ODT we observe in our simulations. From Fig. 3, it is evident that even the system at $\eta > \eta_\mathrm{c}$ is still microphase-separated, i.e., domains where $\psi > 0$ (bright) and $\psi < 0$ (dark) can be distinguished. Only the long-range order of the stripe pattern has been destroyed. This is at variance with the picture presented before, where the phase transition marks the point where the free energy of the modulated state becomes lower than that of the uniform state. This can be modeled by a change of the sign of the coefficient of the ψ^2 term in Eq. (2) [127], which causes the appearance of two symmetric minima in the bulk free energy density. However, the shape of the free energy remains unchanged in case of the noise-induced ODT. It is therefore unclear if the latter corresponds to a naturally occurring phase transition, because the strength of the noise and the temperature, which determines the shape of the free energy, usually cannot be varied independently. It might therefore be a pecularity of the model given by the Langevin equation (3). Furthermore, at least in Rayleigh-Bénard systems, the strength of fluctuations is usually very small [135]. An exception might be realized in experiments close to the critical point of the fluid used in the convection experiment [136].

The effects of varying the noise strength in computer simulations of stripe-forming systems have been described previously [45, 46, 132, 137]. In Ref. 45, a succession of smectic, nematic, and isotropic states has been reported as the noise strength was increased, with the noise-induced ODT corresponding to the nematic-isotropic transition. In our investigation, we keep in mind that the stripe system at $\eta < \eta_\mathrm{c}$ is not in equilibrium even at the latest accessible times, as discussed before. A detailed study of the noise-induced ODT would require a huge numerical effort, including far longer simulations to achieve equilibrated systems, the collection of better statistics in order to apply more sophisticated methods of analysis, as well as simulations of different system sizes in order to study finite-size scaling [6]. Therefore, we restrict ourselves to a rather simple investigation of the ODT.

In Fig. 21, we plot several quantities as a function of the noise strength η, computed from a sample of ten stripe patterns at a time $t = 5 \cdot 10^5$. As it is not clear *a priori* which quantities

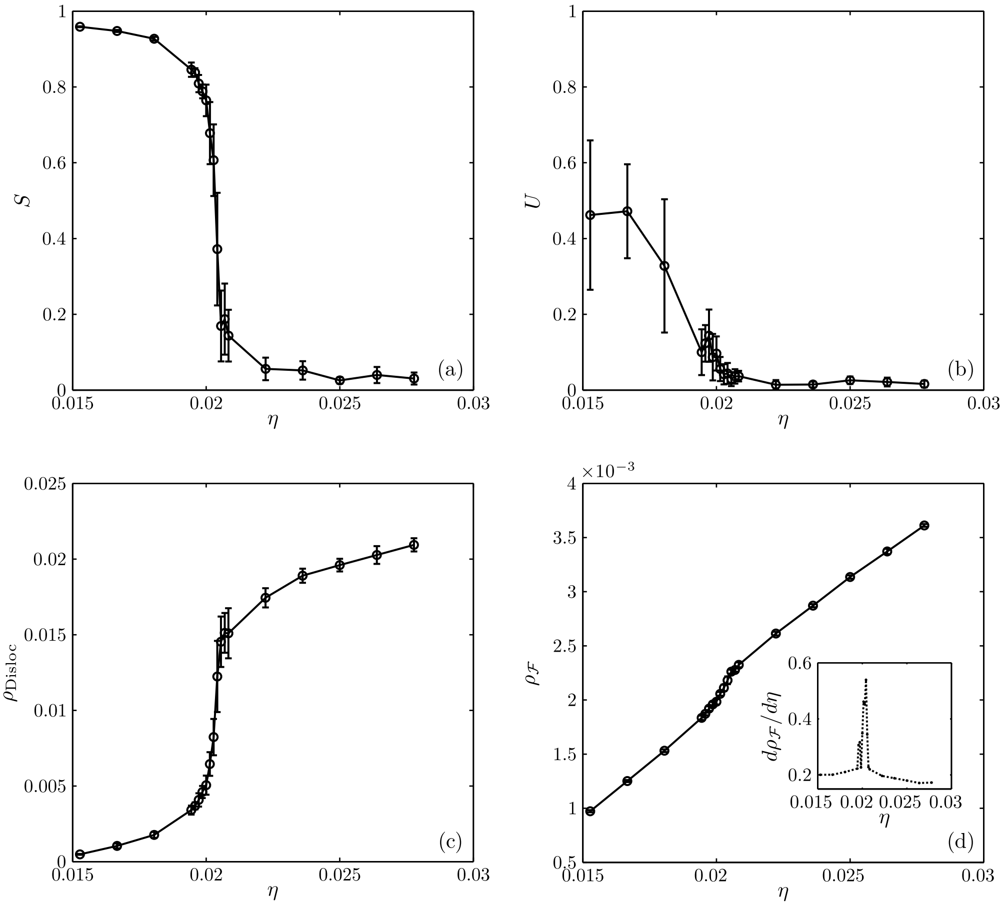

FIG. 21. Possible order parameters for the ODT plotted as a function of the noise strength η: (a) orientational order parameter S, (b) translational order parameter U, (c) defect density ρ_{Disloc}, (c) free energy density $\rho_{\mathcal{F}}$. The error bars represent the standard deviation over a sample of ten independent realizations. For all data, $t = 5 \cdot 10^5$. The inset in (d) shows the derivative of the free energy density with respect to the noise strength.

adequately describe the transition, this comparison enables us to identify a useful order parameter. The orientational order parameter S and the translational order parameter U are shown in Fig. 21(a) and (b), respectively. S exhibits a sharp drop from values close to unity to nearly zero at a noise strength slightly above $\eta = 0.02$. Notably, the error bars are largest close to this transition point, whereas they are fairly small for noise strengths above and below. In contrast to S, the translational order parameter U has already dropped below 0.5 at $\eta \approx 0.015$ and also exhibits large fluctuations. There is no well-defined decrease at $\eta \approx 0.02$, and U remains close to zero for higher values of η. In addition to these order parameters, we have investigated the behavior of the defect density ρ_{Disloc}, which increases sharply at $\eta \gtrsim 0.02$ [Fig. 21(c)]. It then seems to approach a constant value for higher values of η. Again, the fluctuations are largest for noise strengths in the critical region. Finally, the free energy density $\rho_{\mathcal{F}}$ displays a linear dependence on the noise strength for both, high and low values of η [Fig. 21(d)], in accordance with the results shown in Fig. 12. At the critical noise strength, there is but a small kink, which seems unsuitable for determining η_{c}. However, the derivative of the free energy density with respect to the noise strength [see the inset in Fig. 21(d)] as well as the standard deviation of $\rho_{\mathcal{F}}$ (not shown) exhibit a peak at $\eta \gtrsim 0.02$. We note that both quantities bear some resemblance to a specific heat capacity, which typically diverges at a phase transition [6].

In this section, we have investigated several quantities describing a stripe pattern in the critical range of the noise strength close to the order-disorder transition. The translational order parameter U does not exhibit a clear signature of the ODT, with values less than 0.5 and large fluctuations observed even far below the ODT. This is in agreement with our earlier findings of steadily decreasing translational order at all noise strengths, even very small ones. Values of U significantly deviating fom zero observed in systems where $\eta < \eta_{\mathrm{c}}$ should therefore be regarded as only a transient, non-equilibrium phenomenon, which renders U useless for studying the ODT. Theory predicts that translational order does not exist in two-dimensional stripe-forming or other crystalline systems at finite temperature due to diverging fluctuations [104, 138]. Our observations in a finite-size system which is only slowly approaching equilibrium are compatible with these assertions. While orientational order is more resilient, truly broken orientational symmetry is not possible in two dimensions either [105, 106]. The extremely slow temporal evolution of the orientational order parameter S (see Fig. 12) nevertheless renders it useful for describing the ODT in finite-size systems. The noise strength at which S has dropped to $\frac{1}{2}$ and the defect density ρ_{Disloc} has reached half its maximum value, as well as the location of the peak in the rate of change of the free energy density $\rho_{\mathcal{F}}$ all point to a critical noise strength $\eta_{\mathrm{c}} = 0.020(3)$. This value constitutes our estimate of η_{c} for $\Gamma = 0.2$. We expect a strong dependence on the parameter Γ, as it controls both the amplitude and the profile of the concentration field $\psi(\mathbf{r}, t)$ [71, 139, 140]. Furthermore, we did not investigate a possible dependence of η_{c} on the system size L. The caveats mentioned before regarding the equilibrium state also must be kept in mind. Nevertheless, we can say that orientational order is lost at the same moment as defects in the stripe pattern appear in large numbers. As in previous sections, it has become clear that the stripe orientation is essential for describing the properties of stripe-forming systems.

F. Conclusion

To summarize, we have studied a simple model for a stripe-forming system evolving from an ordered state under the influence of noise. Using numerical simulations of model B with Coulomb interactions, we have found aging in the autocorrelation function $C_\theta(t, t_\mathrm{w})$ of the local stripe orientation. The system does not reach a stationary state within the time range we were able to explore. Investigating spatial correlations at early times, we found that the orientational correlation length $\xi_\theta^\perp$ perpendicular to the stripes grows as a power law of time with an exponent $\frac{1}{2}$. At very late times, the spatial correlation function $C_\theta(r_\perp, r_\parallel = 0, t)$ decays as a power of the distance, with an exponent depending on the noise strength.

As a first approach, we have interpreted the observed dynamics as arising from the critical nature of the orientation fluctuations in two dimensions. This is corroborated by the scaling form of the orientation autocorrelation function, the power-law decay of spatial correlations at late times, and by the probability distribution of the orientational order parameter for low noise strengths. Throughout this chapter, we have compared our results for the stripe-forming system to the well-known properties of the two-dimensional XY model, which is critical for a whole range of temperatures below T_KT [99–101]. However, while there are a number of similarities, the two systems are also qualitatively different in several aspects. Most importantly, the stripe-forming system is anisotropic, since the concentration field is modulated only in one direction. This anisotropy will be investigated in detail in Sec. IV. Furthermore, the exponents characterizing the spatio-temporal correlation functions differ from those found in the XY model with respect to their magnitude, dependence on the noise strength as well as their mutual relations. Therefore, the stripe-forming system does not belong to the universality class of the 2D XY model.

Two-dimensional stripe patterns at finite noise strength have been referred to as nematics before [45, 46], even though an in-depth study of the orientation dynamics had not been performed yet. The present work fills this gap by demonstrating the importance of the orientation field for an adequate description of a stripe-forming system, particularly for assessing its proximity to equilibrium. We have shown that the orientation field $\theta(\mathbf{r}, t)$ exhibits

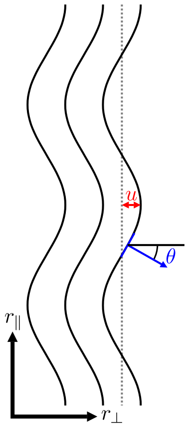

FIG. 22. Illustration of the stripe displacement u and the stripe orientation θ. The thick black lines represent the center lines of individual stripes, while the dashed grey line indicates $u = 0$.

a complex non-equilibrium dynamics in $d = 2$ spatial dimensions. This is also evidenced by a slow but steady decrease of both, the orientational and the translational order parameter. These phenomena can be interpreted as a consequence of the strength of fluctuations in low dimensions [138], especially when continuous symmetries are considered [105]. On the other hand, the picture of the stripe-forming system evolving on a rugged free-energy landscape could be excluded by performing quenches to zero noise. In this case, the system also undergoes a slow relaxation, but no indications for local minima of the free energy were detected. Theoretical results predicting a glass transition for the stripe-forming system [115, 117] are presumably related to configurations comprising topological defects [116].

We found that topological defects do not play an important role in determining the properties of the stripe-forming system. This is somewhat unexpected, since the equilibrium properties of 2D smectics strongly depend on whether defects are present or not [104]. However, we note that the results from Ref. 104 are valid for large length scales. Therefore, huge system sizes might be necessary to observe the predicted behavior.

In the present work, we have focused on the dynamics of the orientation field $\theta(\mathbf{r}, t)$. Another quantity worth investigating is the stripe displacement u, which is related to translational degrees of freedom (see Sec. III E). Fig. 22 illustrates the relation between the orientation angle θ and the displacement u. The displacement field is central in the theoretical description of smectic systems [91, 104], and should provide further insights into the properties of the stripe-forming system.

IV. ANISOTROPIC COARSENING AND SPATIAL CONFINEMENT

In this section, we continue our study of aging in an ordered stripe-forming system free of topological defects. In the previous section, we have described the aging effect in the correlation functions of the orientation field $\theta(\mathbf{r}, t)$. We found that the aging is driven by the coarsening of spatial orientation fluctuations. Here, we present an in-depth investigation of this phenomenon, focusing on the effect of different system sizes and aspect ratios while imposing periodic boundary conditions. The need to study different aspect ratios arises because of the inherent anisotropy of an ordered stripe-forming system. This anisotropy also emerges in a theoretical analysis of 2D smectics [104].

Finite-size scaling first emerged as a concept in the study of equilibrium phase transitions in finite systems [141]. Later it became an important tool for the interpretation of computer simulations, where accessible system sizes are still much smaller than macroscopic samples [142]. Scaling concepts in different forms have also proven essential for understanding systems out of equilibrium. Domain growth in phase-ordering systems after a quench [16, 97] is one example where finite-size scaling has been studied extensively [143–149]. Recently, the influence of the system size on the aging behavior has also been investigated [150]. Furthermore, the dependence of the orientational susceptibility on the system size has been used to test theoretical results for different stripe-forming systems [151]. A different class of systems out of equilibrium is given by growing surfaces and interfaces [152]. In this scenario, the width or roughness of a manifold depends on the size of the system, as expressed by the well-known Family-Vicsek scaling form [153].

Here we investigate the finite-size scaling behavior of orientation fluctuations in a stripe-forming system. Growing length scales parallel and perpendicular to the stripe pattern are identified, and finite-size scaling reveals the exponents governing the coarsening process.

As discussed in the previous section, we prepare the system described by Eq. (1) in a perfectly ordered state. Only a few studies have followed this route [78, 94], where the focus was on possible applications of block copolymers as lithographic masks [77, 95, 154]. For our purposes, the initial state is given by $\psi(\mathbf{r}, t = 0) = A\cos(2\pi/\lambda_0 r_\perp)$, where $\mathbf{r} \equiv (r_\perp, r_\parallel)^\intercal$, $A = 2\sqrt{(1 - 2\sqrt{\Gamma})/3}$ and $\lambda_0 = 2\pi\Gamma^{-\frac{1}{4}}$. This choice of parameters minimizes the free energy, Eq. (2), in a single-mode approximation [71]. We fix the interaction parameter $\Gamma = 0.2$, for which Eq. (1) exhibits stripe formation [38], and the noise strength $\eta/\eta_\mathrm{c} = \frac{1}{30}$. We have

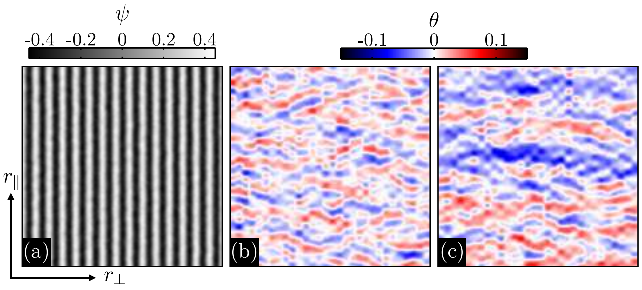

FIG. 23. Examples for the temporal evolution of the ordered stripe-forming system. Snaphots of size $15\lambda_0 \times 15\lambda_0$ are shown of (a) the concentration field $\psi(\mathbf{r}, t)$ and (b, c) the orientation field $\theta(\mathbf{r}, t)$. The time $t = 5 \cdot 10^1$ in (a, b) and $t = 5 \cdot 10^5$ in (c). The system size is $L = 55\lambda_0$.

performed simulations of Eq. (1) with periodic boundary conditions in $d = 2$ dimensions on lattices with size $L_\perp \times L_\parallel$ using the same algorithm as before [73]. Time and space have been discretized in increments of $\Delta t = 0.1$ and $\Delta r = \lambda_0/10$, respectively. The latter choice avoids any mismatch between the system size and the intrisic wave length λ_0 of the stripes if the system size $L_\perp$ is an integer multiple of λ_0. As we use periodic boundary conditions, a remark is in order on the effect of confinement in small systems. In experiments, alignment of stripe-forming block copolymers and long-range order can be induced by placing thin films on structured substrates featuring extended troughs [155–160]. In simulations, this corresponds to no-flux boundary conditions [161–163]. We expect a strong damping of fluctuations near such boundaries, effectively partitioning the system into areas close and far away from the boundaries, respectively. Therefore, we choose periodic boundary conditions, which enable changing the system size without introducing any surface effects.

In the following, we will build upon our recent study of the aging dynamics of this stripe-forming system [44]. As before, we will be investigating the local stripe orientation $\theta(\mathbf{r}, t)$, computed using the gradient-square tensor [83, 84, 90], and its spatio-temporal correlation functions. Examples for the concentration field $\psi(\mathbf{r}, t)$ and the corresponding orientation field $\theta(\mathbf{r}, t)$ are shown in Fig. 23. We remind the reader that the two-time autocorrelation function is given by Eq. (7), while the spatial correlation function is defined by Eq. (8).
We now introduce a related quantity, namely the structure factor of the orientation $S_\theta(\mathbf{k}, t)$, which is given by the Fourier transform of the spatial orientation correlation function. Since

we are using periodic boundary conditions,

$$S_\theta(\mathbf{k}_{mn}, t) \equiv \frac{1}{L_\perp L_\|} \int_0^{L_\perp} \int_0^{L_\|} C_\theta(\mathbf{r}, t) e^{-i\mathbf{k}_{mn}\mathbf{r}} d^2 r, \tag{12}$$

where the discrete wave vectors $\mathbf{k}_{mn} \equiv (2\pi m/L_\perp, 2\pi n/L_\|)^\intercal$, and $m, n \in \mathbb{Z}$. As we have reported previously [44], a growing length scale perpendicular to the stripes can be extracted from the spatial correlation function $C_\theta(r_\perp, r_\| = 0, t)$. This spatial correlation length $\xi_\theta^\perp$ was found to grow as $\xi_\theta^\perp \sim t^{0.5}$ (see Sec. III B). In the direction parallel to the stripes, no evolution of $C_\theta(r_\perp = 0, r_\|, t)$ associated with a growing length scale could be identified. Nevertheless, a visual comparison of orientation fields $\theta(\mathbf{r}, t)$ at different times t reveals that the characteristic size of the fluctuations also grows in the direction parallel to the stripes [see Fig. 23(b) and (c)]. Below, we will show that this coarsening process can be described using the structure factor of the orientation.

The remainder of this paper is organized as follows: In Sec. IV A, we will present results for the structure factor obtained from large square systems with $L = L_\perp = L_\|$. In the main part of this work (Sec. IV), we will study confined systems, for which at least one dimension is small, i.e., only a few multiples of the wave length λ_0 of the stripe pattern. The effect of different aspect ratios on the dynamics as well as on the stationary states observed at late times will be investigated. A discussion of the results and their implications will be given in Sec. IV C, followed by a summary.

A. Results for large systems

In Fig. 24(a), we present cuts through the two-dimensional structure factor $S_\theta(k_\perp = 0, k_\|, t)$ computed from a square system where $L = L_\perp = L_\| = 55\lambda_0$. The results have been averaged over 40 independent realizations. At low wave numbers $k_\|$, $S_\theta(k_\perp = 0, k_\|, t)$ exhibits a single peak, whose intensity grows with time. Simultaneously, the peak position shifts to lower $k_\|$ as time progresses. At high wave numbers, the structure factor decreases rapidly. Comparing the data for different times t, we note that there is no evolution for $k_\| \gtrsim 0.5$ (corresponding to wave lengths less than $1.3\lambda_0$), i.e., the curves for different times fall on top of each other. Since the shift and growth of the peak is the only discernible evolution, the range over which the structure factor is static increases with time.

In the following, $k_\|^*$ designates the wave number $k_\|$ for which $S_\theta(k_\perp = 0, k_\|, t)$ attains its

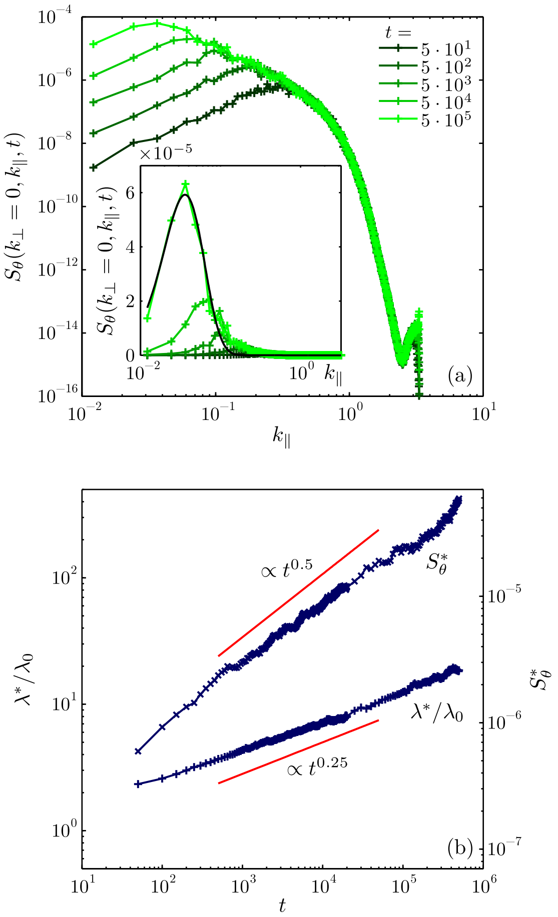

FIG. 24. Temporal evolution of the structure factor $S_\theta(k_\perp = 0, k_\parallel, t)$ parallel to the stripes in a system with $L = L_\perp = L_\parallel = 55\lambda_0$. (a) The strucure factor is shown at different times ranging from $t = 5 \cdot 10^1$ (dark) to $t = 5 \cdot 10^5$ (bright). In the inset, the same data are plotted on a lin-log scale. The continuous black line is a fit function discussed in the text. (b) The peak intensity S_θ^* and the wave length λ^* corresponding to the peak position $k_\parallel^* = 2\pi/\lambda^*$ are plotted as a function of time. The red lines represent power laws with the indicated exponents.

maximum value S_θ^*. The corresponding wave length will be referred to as the dominant wave length $\lambda^* \equiv 2\pi/k_\parallel^*$. To extract the peak position $k_\parallel^*$ and intensity S_θ^*, we have fitted the function $f(k_\parallel) = a k_\parallel^b \exp(-c k_\parallel)$ to the structure factor [see the inset in Fig. 24(a)]. In terms of the fit parameters a, b, and c, $k_\parallel^* = b/c$, $\lambda^* = 2\pi c/b$, and $S_\theta^* = a(\frac{b}{c})^b e^{-b}$. The results thus obtained are shown in Fig. 24(b). Both quantities, S_θ^* and λ^*, grow as power laws of time, but with different exponents. The dominant wave length λ^* increases as $\lambda^* \sim t^{0.25}$, while the peak intensity grows as $S_\theta^* \sim t^{0.5}$. These relations are independent of the noise strength η, which is demonstrated in Appendix C. Within the time range considered here, $t \leq 5 \cdot 10^5$, neither quantity attains stationarity, indicating that the coarsening process is still in progress at the latest times. This is in line with the aging behavior of the autocorrelation function $C_\theta(t, t_\mathrm{w})$ reported before [44]. A natural limit for the growth of λ^* is the system size $L_\parallel$, corresponding to $k_\parallel^{*,\mathrm{max}} = 2\pi/L_\parallel \approx 0.012$ for $L_\parallel = 55\lambda_0$. On the other hand, there is no *a priori* reason for the peak intensity S_θ^* to saturate. Below, we will investigate the influence of the system's dimensions on its long-time behavior by turning to small systems where a stationary state is reached.

B. Finite-size effects

As we have seen in the previous section, the structure factor of the orientation does not reach a stationary state in systems with $L = 55\lambda_0$ even at the latest accessible times. This agrees with our findings for the two-time autocorrelation function $C_\theta(t, t_\mathrm{w})$ [44]. As we are interested in the final state which the stripe-forming system approaches, reducing the system size provides a way to follow the evolution until stationarity is attained. Due to the inherently anisotropic nature of the ordered stripe-forming system, finite-size effects may be introduced in different ways [see Fig. 25(a)]. The simplest approach is to reduce the system size $L = L_\perp = L_\parallel$, thus maintaining a square system. Additionally, only one side can be made small while keeping the other one large. This results in a rectangular geometry, which either contains numerous short stripes ($L_\parallel \ll L_\perp$) or only a few but long stripes ($L_\perp \ll L_\parallel$). Examples for the concentration fields $\psi(\mathbf{r}, t)$ at a late time $t = 5 \cdot 10^5$ are presented in Fig. 25(a). The orientation field $\theta(\mathbf{r}, t)$, as shown in Fig. 25(b) and (c), turns out to be more informative regarding the state of the different systems. In addition to the orientation field $\theta(\mathbf{r}, t)$ [Fig. 25(b)], we have also computed a filtered orientation field, where structures smaller than one wave length λ_0 have been removed [Fig. 25(c)]. Our rationale for doing so is the observed behavior of the structure factor (see Fig. 24), where no evolution takes place at large wave numbers. The small square system [bottom left of Fig. 25(c), shown in full] exhibits a modulation of the orientation field which spans the whole extent of the system parallel to the stripes, whereas almost no variation is seen in the perpendicular direction. The latter also holds for the system where $L_\perp \ll L_\parallel$ (top left), although the orientation fluctuations parallel to the stripes are longer. In comparison, the amplitude of the fluctuations observed in the large square system (top right) is smaller, and there is a

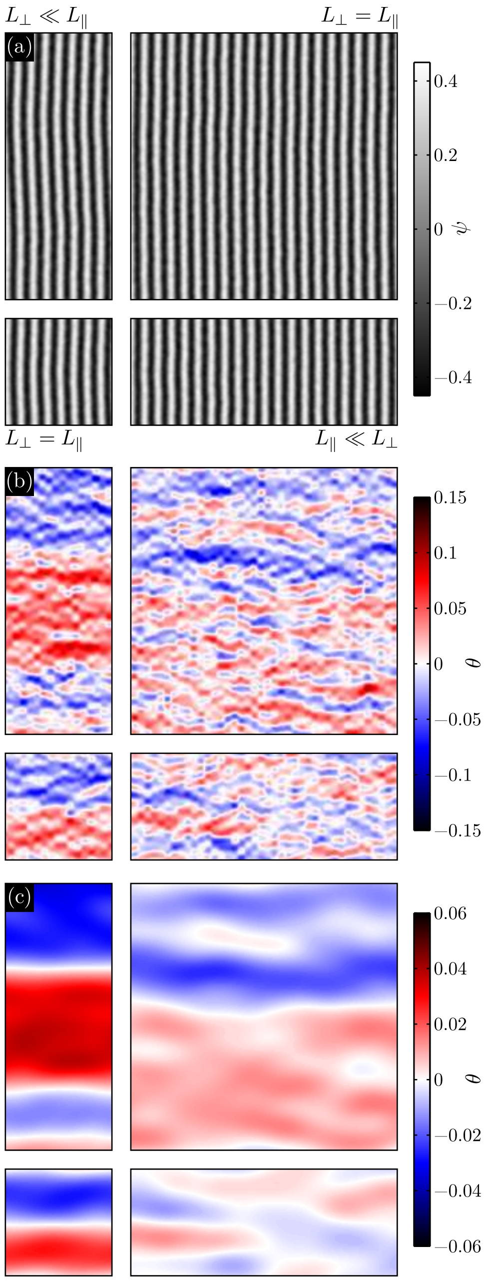

FIG. 25. Examples of confined stripe-forming systems. (a) Concentration fields $\psi(\mathbf{r}, t = 5 \cdot 10^5)$. Top left: A $8\lambda_0 \times 20\lambda_0$ section from a $8\lambda_0 \times 384\lambda_0$ system. Top right: A $20\lambda_0 \times 20\lambda_0$ section from a $55\lambda_0 \times 55\lambda_0$ system. Bottom left: A snapshot from a $8\lambda_0 \times 8\lambda_0$ system. Bottom right: A $20\lambda_0 \times 20\lambda_0$ section from a $384\lambda_0 \times 8\lambda_0$ system. (b) Orientation fields $\theta(\mathbf{r}, t)$ corresponding to (a). (c) Orientation fields $\theta(\mathbf{r}, t)$ filtered with a Gaussian having a width $\sigma = \lambda_0$.

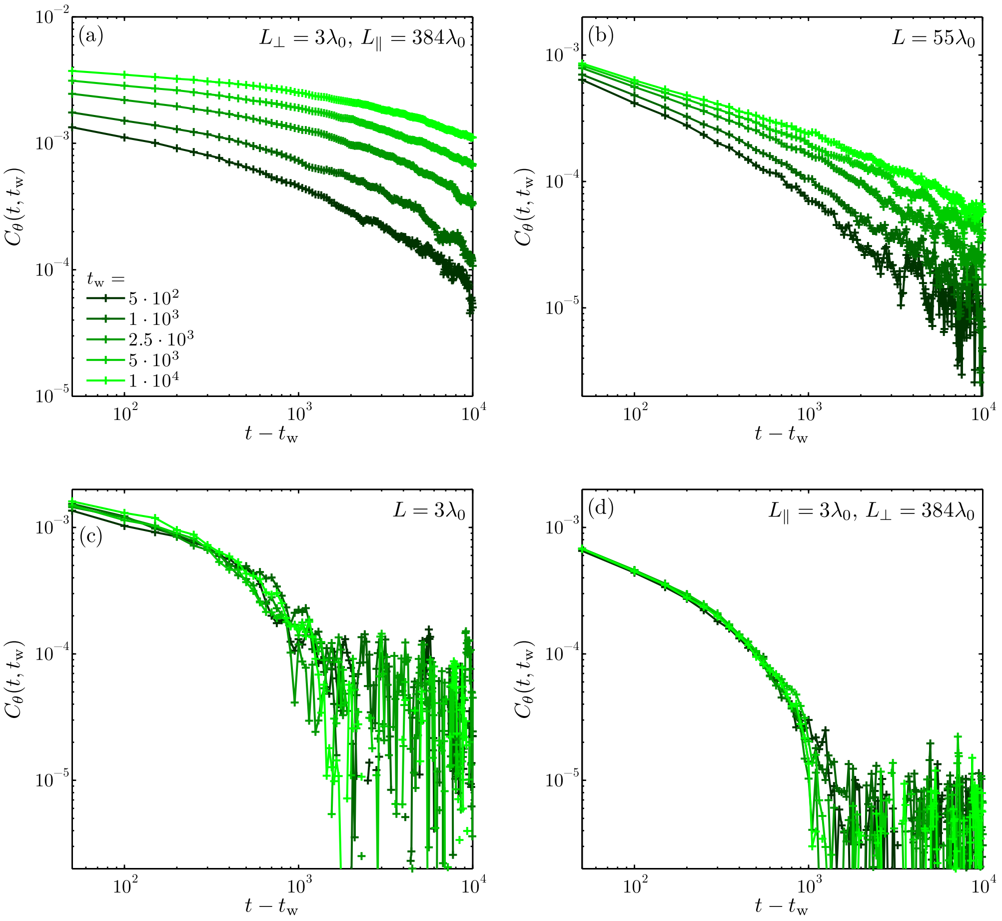

FIG. 26. Influence of a finite system size on aging. The orientation autocorrelation function $C_\theta(t, t_\mathrm{w})$ is presented for different waiting times t_w. Aging is present in (a,b), but not in (c,d). Data are shown for (a) long stripes ($L_\perp \ll L_\parallel$), (b) a large square system ($L = 55\lambda_0$, as in Ref. [44]), (c) a small square system with $L = 3\lambda_0$, and (d) short stripes ($L_\parallel \ll L_\perp$).

certain degree of variation perpendicular to the stripes. This is also the case for the system where $L_\parallel \ll L_\perp$ (bottom right). Below, we will demonstrate that these different geometries also have a profound influence on the dynamics of the system.

1. *Influence on the aging behavior*

In order to assess the influence of confinement on the stripe-forming system, we first consider the behavior of the orientation autocorrelation function $C_\theta(t, t_\mathrm{w})$. In Fig. 26, data from a system with $L = 55\lambda_0$ are juxtaposed with results from rectangular and small square systems. The former, which has been discussed in detail in Ref. 44, are shown in Fig. 26(b), serving as our point of reference. The decay of the autocorrelation function $C_\theta(t, t_\mathrm{w})$ depends on the waiting time t_w. The longer t_w is, the slower the relaxation becomes. In systems containing a small number of long stripes [Fig. 26(a)], the influence of the waiting time is even stronger than for the square system [Fig. 26(b)]. As the waiting time t_w increases, so does the magnitude of $C_\theta(t, t_\mathrm{w})$, while the shape of the function remains mostly unchanged. This indicates that the average of the orientation $\langle e^{2i\theta_{\mathbf{r},t}}\rangle_{\zeta,\mathbf{r}}$ (cf. the definition of $C_\theta(t, t_\mathrm{w})$), Eq. (7)), decreases considerably as the waiting time is increased, i.e., the system becomes more disordered over time. Furthermore, the detailed shape of $C_\theta(t, t_\mathrm{w})$ deviates from that observed in the large square system.

In the two remaining confined scenarios, namely, in a small square system [Fig. 26(c)] and in a system containing many short stripes [Fig. 26(d)], the dynamics of the autocorrelation function $C_\theta(t, t_\mathrm{w})$ is very different. In both cases, the relaxation is notably faster, and $C_\theta(t, t_\mathrm{w})$ does not depend on the waiting time t_w. From these observations we conclude that the orientation dynamics reaches a stationary state in systems where $L_\parallel$ is small. In contrast, a small system size perpendicular to the stripes ($L_\perp \ll L_\parallel$) does not inhibit the aging process. The detailed influence of the system dimensions on the structure factor and related quantities will be investigated in the next section.

2. Small square systems ($L_\perp = L_\parallel$)

We first consider square systems where the side length $L = L_\perp = L_\parallel$ is a small integer multiple of the stripe wavelength λ_0. All results shown have been averaged over at least 80 independent realizations. As seen in Fig. 27(a), the structure factor $S_\theta(k_\perp = 0, k_\parallel, t)$ undergoes an evolution similar to the one seen in the larger system (Fig. 24), with the peak shifting to smaller wave numbers $k_\parallel$ and the peak intensity S_θ^* growing in time. However, for times $t \gtrsim 2500$, the peak position has reached the lowest possible value, $k_\parallel^* = 2\pi/L$, while the peak intensity S_θ^* continues to grow. Therefore, we omit the fitting procedure used before and determine S_θ^* directly as the maximum of $S_\theta(k_\perp = 0, k_\parallel, t)$ over all $k_\parallel$. In Fig. 27(b), S_θ^* is plotted as a function of time for two different system sizes, showing initial growth followed by a cross-over to saturation. To quantify this behavior, we have fitted an exponential function $f(t) = A[1 - \exp(t/\tau_S)]$ to $S_\theta^*(t)$, which yields the crossover time τ_S. The saturation value $S_\theta^{*,\mathrm{sat}}$ has been computed as the average of $S_\theta(k_\perp = 0, k_\parallel^*, t)$ over

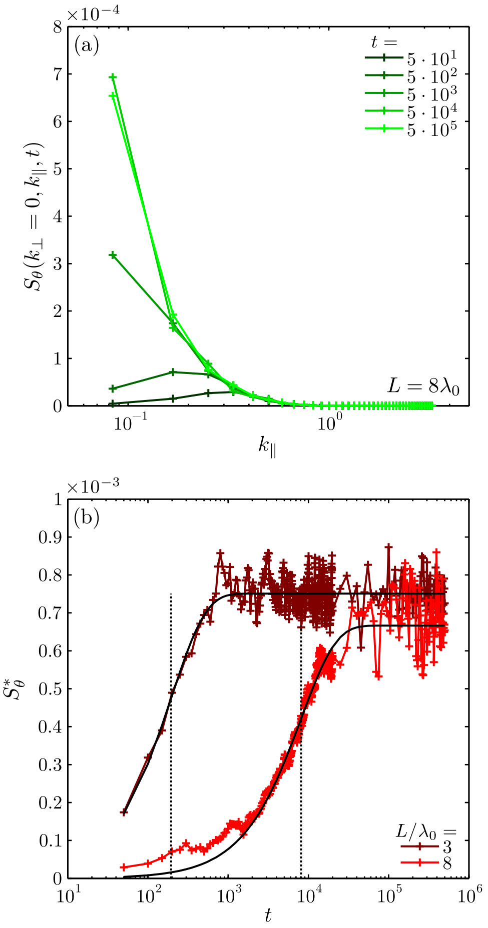

FIG. 27. Evolution and finite-size behavior of the structure factor $S_\theta(k_\perp = 0, k_\parallel, t)$ in small square systems. (a) $S_\theta(k_\perp = 0, k_\parallel, t)$ is plotted at different times t for $L = 8\lambda_0$. (b) The peak intensity S^*_θ is plotted as a function of time for two different system sizes. The continuous black lines are fits to the data. The dashed black lines indicate the cross-over time τ_S.

times $t > 10^5$, for which the intensity has saturated for all system sizes we consider. The corresponding standard deviation serves as a measure of the statistical uncertainty. We note that the difference of the saturation values suggested by the fit functions shown in Fig. 27(b) is less than this uncertainty and thus not significant.

The two quantities S^*_θ and τ_S are plotted as a function of the system size L in Fig. 28(a) and (b). While the saturated peak intensity S^*_θ remains constant as L is increased, the cross-over time τ_S exhibits a power-law dependence on L, $\tau_S \sim L^4$. Having determined these two relationships on the system size, we can attempt a scaling plot using data from different systems. This is shown in Fig. 28(c), where a collapse is observed upon rescaling the time

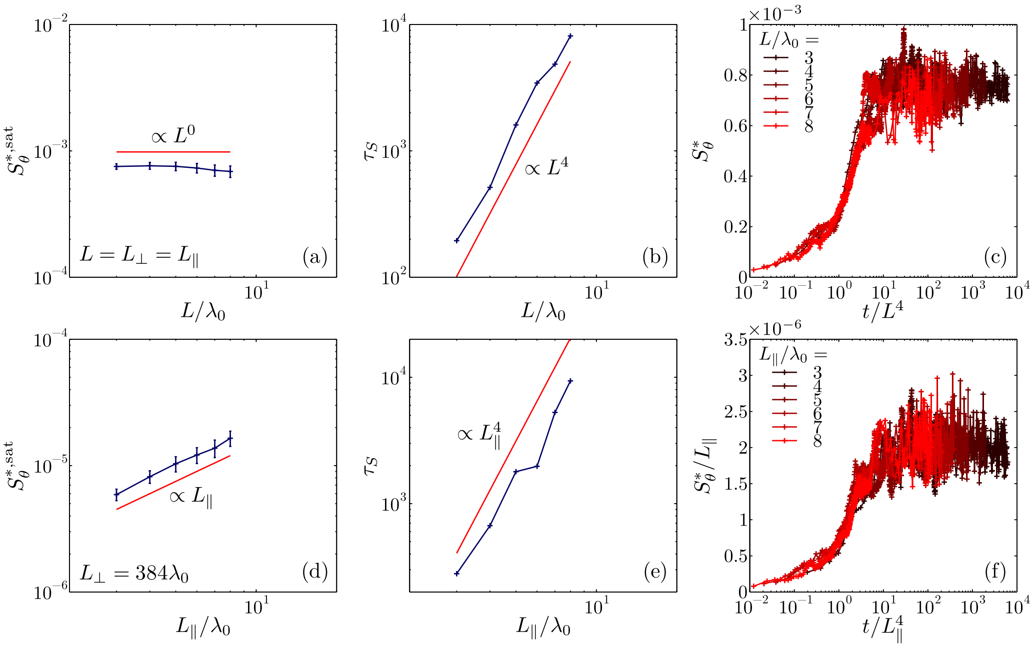

FIG. 28. Finite-size scaling in (a–c) square systems and (d–f) rectangular systems containing short stripes. In (a, d) and (b, e), the saturation value $S_\theta^{*,\mathrm{sat}}$ and the corresponding cross-over time τ_S are plotted as a function of the system sizes L and $L_\parallel$, respectively. The red lines represent power laws with the indicated exponents. Rescaled data are presented in (c) and (f), demonstrating a scaling collapse.

by L^4, confirming the functional dependence of the structure factor on the system size L. We note that the divergence of the cross-over time $\tau_S \sim L^z$ is consistent with the growth of the dominant wave length $\lambda^* \sim t^{\frac{1}{z}}$ observed earlier (see Fig. 24). Both relations express an equivalent connection between time and length scales, which can be used to determine the dynamic exponent [97] $z = 4$. The scaling laws and exponents will be further discussed in the following section.

3. Short stripes ($L_\parallel \ll L_\perp$)

a. Structure factor We have performed a similar analysis of the finite-size scaling behavior for rectangular systems containing numerous short stripes ($L_\parallel \ll L_\perp$). Here, the extension $L_\parallel$ parallel to the stripes has been varied, while $L_\perp = 384\lambda_0$ has been kept constant. All results have been averaged over 40 realizations. The quantities describing the structure factor $S_\theta(k_\perp = 0, k_\parallel, t)$ are shown in Fig. 28(d–f). The saturated peak intensity $S_\theta^{*,\mathrm{sat}}$ and the cross-over time τ_S both exhibit power-law growth as a function of the system size $L_\|$, corresponding to the length of the stripes. $S_\theta^{*,\mathrm{sat}}$ grows linearly with $L_\|$, while $\tau_S \sim L_\|^4$. In the latter case, the exponent is the same as the one observed in small square systems. The scaling of the peak intensity S_θ^* with time and system size is confirmed by the scaling collapse shown in Fig. 28(d). These observations indicate that when $L_\perp$ is large, $L_\|$ not only limits the growth of the dominant wave length λ^*, but also controls the saturation of the intensity S_θ^*.

The results shown in Figs. 27 and 28 suggest that the structure factor should scale as $S_\theta^{\mathrm{sat}}(k_\perp = 0, k_\|) \sim \hat{f}_1(k_\| L_\|)$ and $S_\theta^{\mathrm{sat}}(k_\perp = 0, k_\|) \sim \hat{f}_2(k_\| L_\|) L_\|$ in square and rectangular systems, respectively, where $\hat{f}_1(k_\| L_\|)$ and $\hat{f}_2(k_\| L_\|)$ are two possibly different scaling functions. We test these scaling forms in Fig. 30. Double-logarithmic plots reveal that there is a collapse of the structure factor for different system sizes, but only for the data point corresponding to $k_\| = 2\pi/L$ $(2\pi/L_\|)$, the smallest wave number in a given system. At higher values of $k_\|$, the curves for different system sizes deviate considerably. However, the magnitude of $S_\theta^{\mathrm{sat}}(k_\perp = 0, k_\|)$ decays rapidly with increasing $k_\|$, making the deviations from scaling less significant. At this point, we recall that the structure factor does not scale with time for sufficiently large wave numbers $k_\| \gtrsim 0.5$, either (see Fig. 24). Therefore we conclude that scaling behavior in $S_\theta(k_\perp = 0, k_\|, t)$ is limited to long wave lengths.

The shapes of the functions plotted in Fig. 29(a) and (b) appear visually very similar, while their magnitude differs by several decades. As it turns out, the structure factors for square systems and for rectangular systems with $L_\| \ll L_\perp$ collapse onto a single curve according to the common scaling form

$$S_\theta^{\mathrm{sat}}(k_\perp = 0, k_\|) \sim \hat{f}(k_\| L_\|) L_\| / L_\perp, \tag{13}$$

which unifies the two expressions discussed before. This is shown in Fig. 30. However, the scaling behavior is still restricted to small wave numbers $k_\|$. Regarding the shape of the scaling function $\hat{f}(k_\| L_\|)$, we note that as the system size $L_\|$ is increased, the structure factor approaches a power law $\sim (k_\| L_\|)^{-2}$. The larger the system, the wider the range over which this behavior is observed.

b. Averaged correlation function Up to this point, we have focused on the influence of the system size and the aspect ratio on the structure factor of the orientation. Now we turn to the spatial orientation correlation function $C_\theta(\mathbf{r}, t)$. It follows from Eq. (12) that the cut through

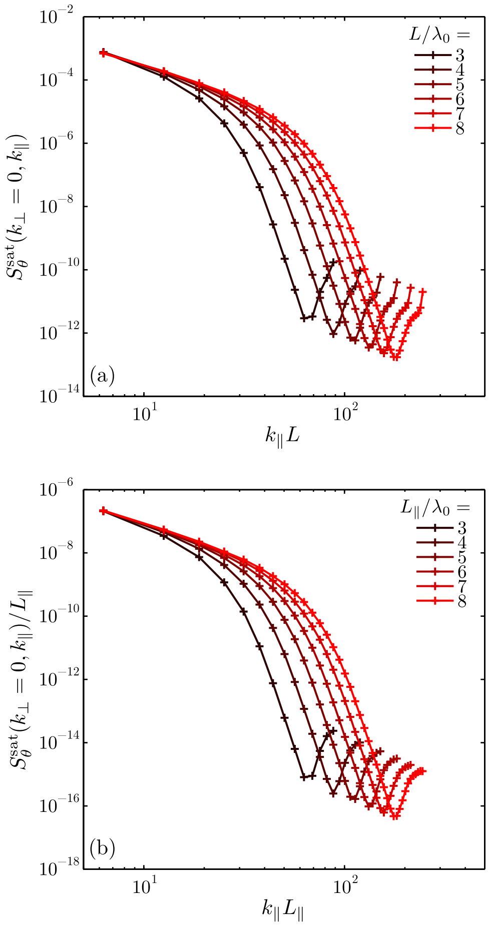

FIG. 29. Scaling behavior of the stationary structure factor $S_\theta^{\mathrm{sat}}(k_\perp = 0, k_\parallel)$. Data are shown for (a) small square systems and (b) systems containing many short stripes.

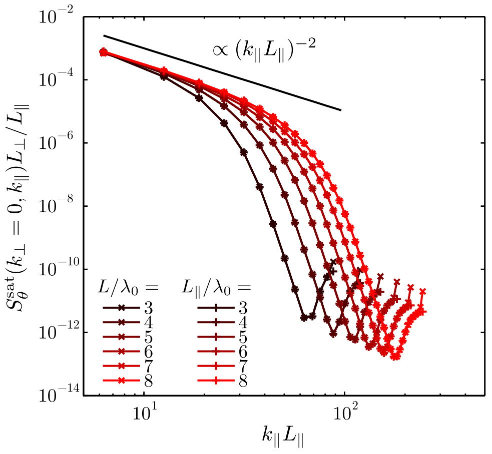

FIG. 30. Common scaling behavior of the structure factor in small square systems (×) and systems containing many short stripes (+). $S_\theta^{\mathrm{sat}}(k_\perp = 0, k_\parallel)$ is plotted in scaling form for different system sizes. The black line represents a power law drawn as a guide to the eye.

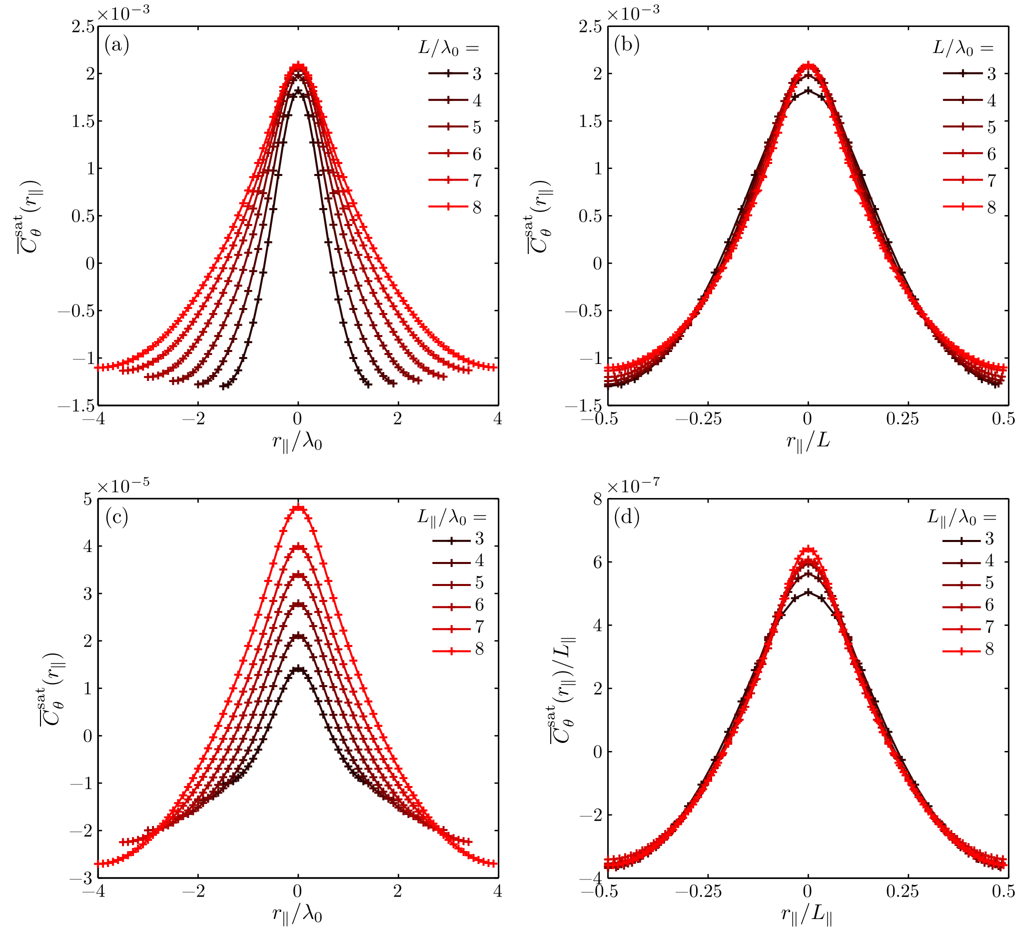

FIG. 31. Scaling behavior of the averaged correlation function $\overline{C}_\theta^{\mathrm{sat}}(r_\parallel)$. Data are shown for (a,b) small square systems and (c,d) systems containing many short stripes. In (b) and (d), the correlation function is plotted in scaling form.

the structure factor given by $S_\theta(k_\perp = 0, k_\parallel, t)$ is the one-dimensional Fourier transform of the averaged spatial orientation correlation function $\overline{C}_\theta(r_\parallel, t) = L_\perp^{-1} \int_0^{L_\perp} C_\theta(\mathbf{r}, t) dr_\perp$. Since we already know the scaling form of the structure factor, the stationary averaged correlation function should scale as

$$\overline{C}_\theta^{\mathrm{sat}}(r_\parallel) \sim f(r_\parallel/L_\parallel) L_\parallel/L_\perp, \tag{14}$$

where $\overline{C}_\theta^{\mathrm{sat}}(r_\parallel)$ is defined as the temporal average of $\overline{C}_\theta(r_\parallel, t)$ for $t > 10^5$. It will be interesting to see how the deviations from scaling seen in case of the structure factor affect the corresponding correlation function. For clarity, we first address different types of confinement seperately. In Fig. 31(a) and (c), we present unscaled data for small square systems and for rectangular systems where $L_\parallel \ll L_\perp$ and $L_\perp = 384\lambda_0$, respectively. In

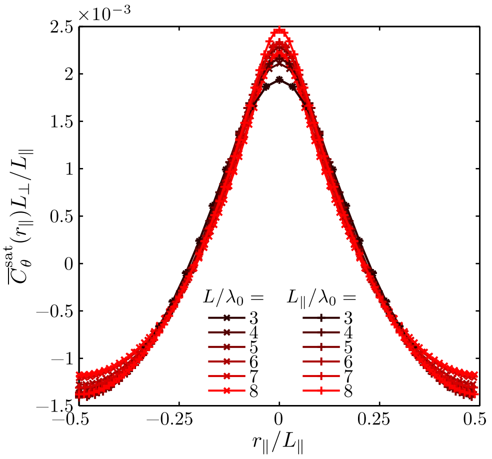

FIG. 32. Common scaling behavior of the averaged correlation function in small square systems (×) and systems containing many short stripes (+). $\overline{C}_\theta^{\rm sat}(r_\parallel)$ is plotted in scaling form for different system sizes.

both cases, we observe a broadening of the correlation function as L ($L_\parallel$) is increased. In rectangular systems, $\overline{C}_\theta^{\rm sat}(r_\parallel)$ also exhibits an increase of its magnitude. To check for finite-size scaling behavior, we have plotted $\overline{C}_\theta^{\rm sat}(r_\parallel)/L$ for small square systems as a function of the scaling variable $r_\parallel/L$ in Fig. 31(b). This results in a collapse of the data onto a master curve. The same can be achieved for rectangular systems where $L_\parallel \ll L_\perp$ by multiplying $C_\theta^{\rm sat}(r_\parallel)$ with a factor $L_\parallel^{-1}$, as shown in Fig. 31(d). In both cases, the collapse is very good, with minor deviations observed at small distances $r_\parallel$ and also for $r_\parallel \approx L/2$ in Fig. 31(b). These aberrations are likely connected to the behavior of the structure factor at high wave numbers seen in Fig. 30, in addition to statistical fluctuations.

Finally, we present a master plot of the averaged correlation function $\overline{C}_\theta^{\rm sat}(r_\parallel)$ for both types of confinement. This is shown in Fig. 32, where the rescaled data fall onto a single curve. According to Eq. (14), for $L_\parallel$ constant, $\overline{C}_\theta^{\rm sat}(r_\parallel = 0)$ decreases with increasing $L_\perp$. On the other hand, if $L_\perp$ is kept constant, the correlation function grows linearly with $L_\parallel$. For square systems, the two prefactors cancel out, resulting in $\overline{C}_\theta^{\rm sat}(r_\parallel) \sim f(r_\parallel/L_\parallel)$, as observed in Fig. 31(b).

With these results in mind, we now return to the temporal evolution observed in the stripe-forming system at early times $t \ll \tau_S$. Following the same reasoning we outlined before, time-dependent length scales should play the roles of effective system sizes in Eq. (14). Therefore, we replace the length scale $L_\parallel$ with the time-dependent dominant wave length

$\lambda^* \sim t^{0.25}$. This yields the following expression for the time-dependent averaged correlation function:

$$\overline{C}_\theta(r_\parallel, t) \sim t^{0.25} g(r_\parallel / t^{0.25}) / L_\perp. \tag{15}$$

For testing the validity of Eq. (15), we us data from square systems with $L = 55\lambda_0$, for which the dynamics is not impeded by finite-size effects even at late times. In Fig. 33(a), we show the unscaled correlation function $\overline{C}_\theta(r_\parallel, t)$ for times $5 \cdot 10^1 \leq t \leq 5 \cdot 10^5$. As the correlation function evolves, the central peak grows and broadens, while the positions of the two symmetric minima shift to larger values of $r_\parallel$. Upon rescaling both, the magnitude and the spatial distance by $t^{0.25}$ respectively, the data collapse onto a single curve. Only the data for the earliest time, $t = 5 \cdot 10^1$, show notable deviations, with the height of the peak less than that observed at later times. Otherwise, the collapse is very good, thus confirming Eq. (15).

At this point, we note that Eq. (15) conforms to the Family-Vicsek scaling [153] typically encountered in interfacial growth and roughening phenomena [152]. This can be seen by writing $\overline{C}_\theta(r_\parallel, t) L_\perp \sim t^{2\beta} g(r_\parallel / t^{\frac{1}{z}})$, where we have introduced the growth exponent $\beta = 0.125$ and the dynamic exponent $z = 4$ as before. A third exponent, the so-called roughness exponent $\alpha = 0.5$, can be read off from the prefactor of the static correlation function, Eq. (14), where $L_\parallel \equiv L_\parallel^{2\alpha}$. It is well known that only two of these exponents are independent, since $z = \alpha/\beta$ [152].

When studying the dynamics of a surface or interface, it is often assumed to be initially flat. Under the influence of thermal fluctuations or the influx of particles, a roughening of the surface is observed [152]. In the stripe-forming system, an analogous process occurs as orientation fluctuations grow under the influence of noise. Their amplitude, as expressed by the averaged correlation function $\overline{C}_\theta(r_\parallel, t)$, saturates at that point in time when the corresponding correlation length, which could be measured as, e.g., the width of the peak seen in Fig. 33, reaches the system size $L_\parallel$.

c. Correlations perpendicular to the stripes In the preceding section, we have discussed the behavior of the averaged correlation function $\overline{C}_\theta(r_\parallel, t)$, which does not capture the dynamics of correlations perpendicular to the stripes. From our previous study [44] of square systems with $L = 55\lambda_0$, we know that the spatial orientation correlation function perpendicular to the stripes $C_\theta(r_\perp, r_\parallel = 0, t)$ decays exponentially at early times, with a correlation length growing as $\xi_\theta^\perp \sim t^{0.5}$. At late times, a cross-over from an exponential to a

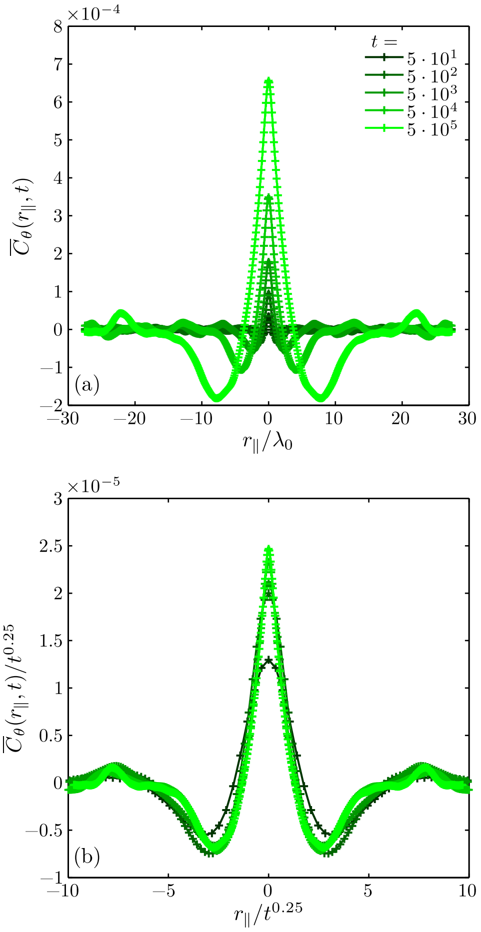

FIG. 33. Scaling behavior of the time-dependent averaged correlation function $\overline{C}_\theta(r_\parallel, t)$. Data are shown for a square system with $L = 55\lambda_0$ in (a) unscaled and (b) scaled form. In (b), only the central portion of the correlation function is plotted, as the curves remain close to zero outside of the indicated range.

power-law decay is observed. Translating this behavior to the case of rectangular systems with $L_\parallel \ll L_\perp$, one might expect the correlation length $\xi_\theta^\perp$ to grow for a much longer period of time until it becomes comparable to the system size $L_\perp$. As it turns out, $\xi_\theta^\perp$ exhibits a very different behavior, since it saturates at much earlier times. We have extracted the time-dependent correlation length by fitting $C_\theta(r_\perp, r_\parallel = 0, t)$ with an exponential $\propto \exp(-r_\perp/\xi_\theta^\perp)$. The results, which we plot as a function of the system size $L_\parallel$, are shown in Fig. 34(a) and (b). The saturated correlation length scales as $\xi_\theta^{\perp,\mathrm{sat}} \sim L_\parallel^2$. Furthermore, the corresponding cross-over time increases as $\tau_\xi \sim L^4$, with the same exponent as observed for τ_S. These results are confirmed by the scaling collapse demonstrated in Fig. 34(c).

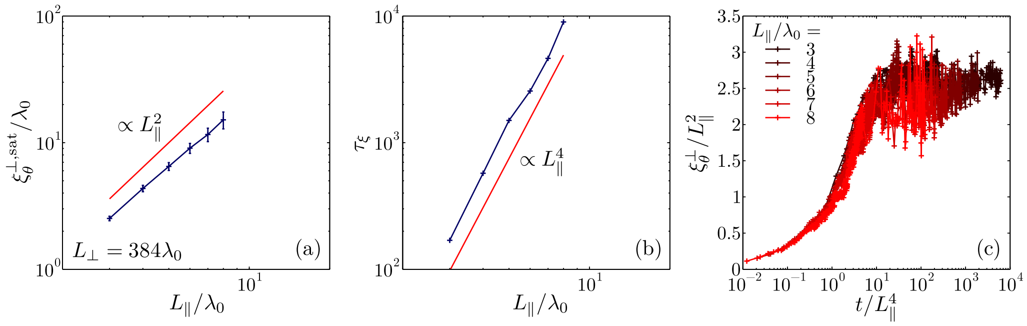

FIG. 34. Finite-size scaling behavior of the correlation length $\xi_\theta^\perp$. (a) The saturated correlation length $\xi_\theta^{\perp,\mathrm{sat}}$ and (b) the corresponding cross-over time τ_ξ determined from rectangular systems are plotted as a function of $L_\parallel$. (c) The correlation length $\xi_\theta^\perp(t)$ has been rescaled to obtain a collapse onto a single curve.

The dynamics of the spatial correlation length in systems where $L_\parallel \ll L_\perp$ which we just described can be directly observed in the behavior of the correlation function $C_\theta(r_\perp, r_\parallel = 0, t)$. In Fig. 35(a), the temporal evolution of $C_\theta(r_\perp, r_\parallel = 0, t)$ is exemplified using data from a system with $L_\parallel = 8\lambda_0$. Initially, the correlation function decays rapidly and resembles an exponential, with a growing correlation length $\xi_\theta^\perp$ readily apparent. This correlation length is plotted in the inset as a function of time on a log-log scale, showing the initial growth, $\xi_\theta^\perp \sim t^{0.5}$, that is also seen in square systems [44]. At late times $t \gtrsim 5 \cdot 10^4$, $\xi_\theta^\perp$ approaches a constant value, as $C_\theta(r_\perp, r_\parallel = 0, t)$ becomes stationary and also changes its shape at small distances $r_\perp$. From Fig. 34(a), we can determine the dependence of the saturated correlation length on the system size,

$$\xi_\theta^{\perp,\mathrm{sat}} \sim L_\parallel^2. \tag{16}$$

This equation holds for both, the growth and the saturation regime. In the latter state, the dominant wave length λ^* is equal to the system size $L_\parallel$. At early times $t \ll \tau_S$, $\lambda^*(t)$ represents an effective system size, assuming that λ^* is the only important length scale in the system. Similar arguments lead to the scaling hypothesis describing the dynamics in many phase-ordering systems [16]. Thus it is natural to replace $L_\parallel$ in Eq. (16) with $\lambda^* \sim t^{0.25}$. This procedure results in $\xi_\theta^\perp \sim t^{0.5}$, as observed in Ref. 44 and in the inset of Fig. 35(a).

Using Eq. (16), we can also plot the stationary correlation function $C_\theta^{\mathrm{sat}}(r_\perp, r_\parallel = 0)$, which we compute as the average of $C_\theta(r_\perp, r_\parallel = 0, t)$ over times $t > 10^5$, as a function of the scaling variable $r_\perp/L_\parallel^2$. Data from systems with different values of $L_\parallel$ plotted in this manner

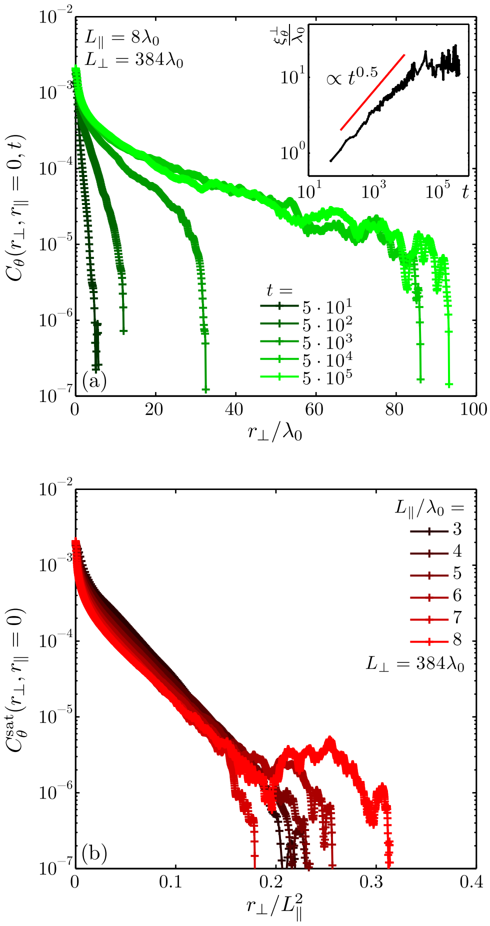

FIG. 35. Scaling behavior of the spatial orientation correlation function $C_\theta(r_\perp, r_\parallel = 0, t)$ in rectangular systems containing short stripes ($L_\parallel \ll L_\perp$). (a) Temporal evolution in a system with $L_\parallel = 8\lambda_0$. The inset shows the correlation length $\xi_\theta^\perp$ as a function of time. (b) The stationary correlation function $C_\theta^{\text{sat}}(r_\perp, r_\parallel = 0)$ plotted as a function of the scaling variable $r_\perp/L_\parallel^2$.

collapse onto a single curve [Fig. 35(b)]. Small deviations mainly result from differences in the magnitude of the correlation function. The scaling collapse confirms Eq. (16) directly, without having to extract the correlation length.

Another important aspect for understanding the behavior of the spatial orientation corrrelation function is the relation between the correlation length $\xi_\theta^\perp$ and the system size $L_\perp$. We can estimate the system size L_ξ for which the correlation length becomes comparable to the system size in a square system with $L_\xi = L_\perp = L_\parallel$. Using the dependence of $\xi_\theta^{\perp,\text{sat}}$ on $L_\parallel$ shown in Fig. 28(g), $\xi_\theta^{\perp,\text{sat}}/\lambda_0 \simeq 0.25 L_\parallel^2$, we set both $\xi_\theta^{\perp,\text{sat}}$ and $L_\parallel$ equal to L_ξ, resulting in $L_\xi \approx 4\lambda_0$. This means that in most of the small square systems studied in Fig. 28(a–c), the saturated correlation length $\xi_\theta^{\perp,\mathrm{sat}}$ exceeds the system size.

To summarize, we have found that the structure factor $S_\theta^{\mathrm{sat}}(k_\perp = 0, k_\parallel)$ in rectangular systems with $L_\parallel \ll L_\perp$ exhibits finite-size scaling as a function of the system size $L_\parallel$. This behavior can be reconciled with the one seen in small square systems [see Eq. (13)]. Related to the structure factor is the averaged orientation correlation function $\overline{C}_\theta(r_\parallel)$, which we studied in both, the stationary and the time-dependent regime. Concerning spatial correlations perpendicular to the stripes, the orientational correlation length $\xi_\theta^\perp$ only grows up to a maximum value determined by $L_\parallel$ [see Eq. (16)]. Therefore we conclude that the system size $L_\parallel$ limits the growth of orientation fluctuations in both, square systems and rectangular systems with $L_\parallel \ll L_\perp$.

4. *Long stripes ($L_\perp \ll L_\parallel$)*

The third type of confinement is realized in systems containing few but long stripes ($L_\perp \ll L_\parallel$), where we fix $L_\parallel = 384\lambda_0$. All results have been averaged over 40 realizations. Again, we are interested in the behavior of cuts through the structure factor parallel to the stripes, given by $S_\theta(k_\perp = 0, k_\parallel, t)$. In Fig. 36, we present data from a system with $L_\perp = \lambda_0$. As observed before in systems with different dimensions, the structure factor exhibits a single peak. The dashed lines in Fig. 36 indicate its position and height at different times t. Both quantities have been determined from fits to the structure factor as described before. The peak position, which can be read off from the abscissa, shifts to smaller wave numbers $k_\parallel$ as the time increases. Since the data are shown on a log-log plot, the constant distance of the dashed lines indicates power-law behavior. In contrast, the lines representing the height of the peak on the ordinate move closer together at later times. This points to the onset of saturation.

We quantify the behavior observed in Fig. 36 in terms of the dominant wave length λ^* and the peak intensity S_θ^* at the wave number $k_\parallel^* = 2\pi/\lambda^*$. The wave length λ^* is plotted as a function of time in Fig. 37(a). Over more than three decades, λ^* grows as a power law $\sim t^{0.25}$, independent of the system size $L_\perp$. This is in accordance with results seen in large square systems (see Fig. 24). While the dynamics of λ^* suggests that the growth of orientation fluctuations is not impeded by perpendicular confinement, the peak intensity S_θ^* does not increase indefinitely. Fig. 37(b) shows S_θ^* as a function of time for different system widths

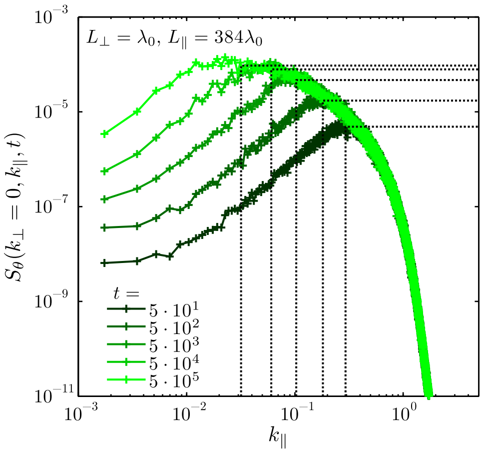

FIG. 36. Temporal evolution of the structure factor $S_\theta(k_\perp = 0, k_\parallel, t)$ in rectangular systems containing long stripes. The dashed lines indicate the peak position and the peak height on the abscissa and the ordinate, respectively.

$L_\perp$. As $L_\perp$ and thus the number of stripes in the system increases, the magnitude of S^*_θ decreases. Futhermore, there is a clear slowdown of the growth at late times observed for all values of $L_\perp$, although S^*_θ does not reach a stationary state for larger values of $L_\perp$. We tentatively fit a stretched exponential $f(t) = S^{*,\mathrm{sat}}_\theta\{1 - \exp[-(t/\tau^\perp_S)^\gamma]\}$ to the data, with the exponent $\gamma = 0.5$. These fit functions are plotted as continuous lines in Fig. 37(b). The results for the fit parameters, shown in Fig. 38, indicate that the saturated peak intensity decreases as $S^{*,\mathrm{sat}}_\theta \sim L_\perp^{-0.5}$, whereas the cross-over time $\tau^\perp_S$ increases linearly with $L_\perp$. These relations allow us to plot the data for S^*_θ in scaling form, as presented in Fig. 37(c). The collapse thus obtained is very good at early times, but fluctuations are present at late times. In conclusion, perpendicular confinement does not inhibit the growth of the dominant wave length λ^*. However, the peak intensity of the structure factor, extrapolated to its saturation value, scales as $S^{*,\mathrm{sat}}_\theta \sim L_\perp^{-0.5}$. This indicates that fluctuations are dampened as more stripes are added to the system, although this relation is not expected to hold for $L_\perp \gg \lambda_0$, since we still observe fluctuations in large square systems (see Fig. 24). Finally, the cross-over time diverges as $\tau^\perp_S \sim L_\perp$. These observations constitute a mechanism for dampening the growth of orientation fluctuations different from the one due to confinement parallel to the stripes. This interplay of finite-size effects can be analyzed further. For square systems, we can estimate the system size $L_{\mathrm{eq}} = L_\perp = L_\parallel$ for which the two cross-over times characterizing the saturation due to confinement in the parallel and perpendicular directions are equal:

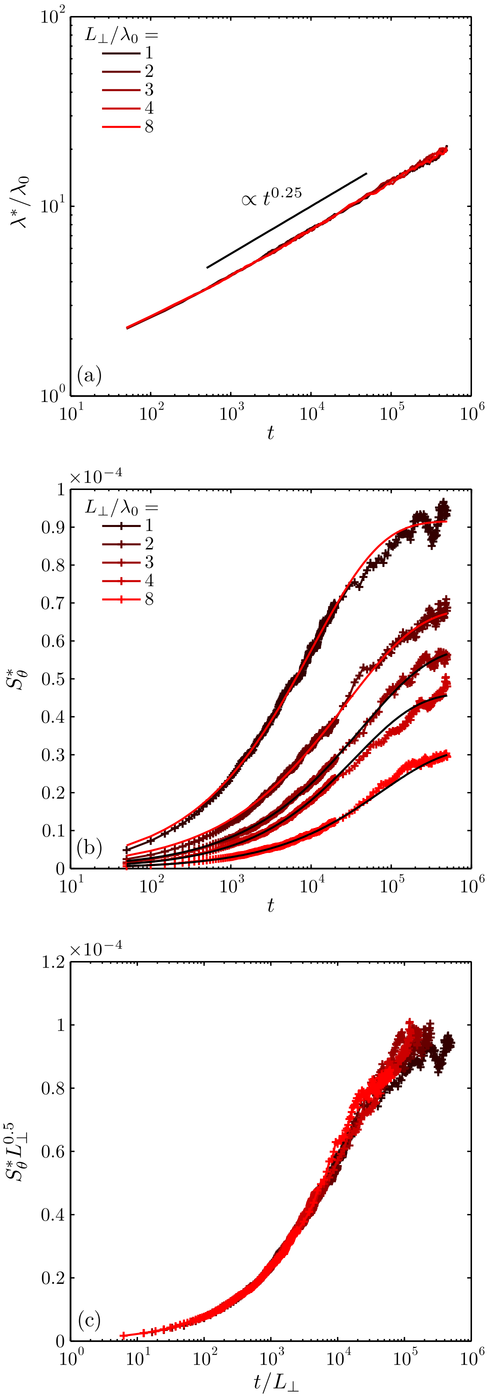

FIG. 37. Scaling behavior of the structure factor in rectangular systems containing long stripes ($L_\parallel = 384\lambda_0$). (a) Growth of the dominant wave length λ^*. The black line is a power law. (b) Temporal evolution of the peak intensity. The continuous lines are fits with a function $f(t)$ discussed in the text. (c) The rescaled intensity $S^*_\theta/L_\perp^{0.5}$ is plotted as a function of $t/L_\perp$.

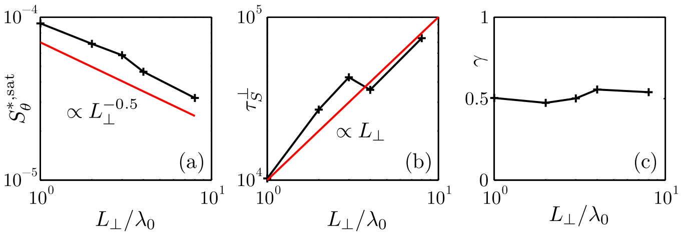

FIG. 38. Fit parameters describing the structure factor as a function of the system width $L_\perp$. (a) Saturated intensity $S_\theta^{*,\mathrm{sat}}$, (b) cross-over time $\tau_S^\perp$, (c) exponent γ.

$L_{\mathrm{eq}}/\lambda_0 = \sqrt[3]{5 \cdot 10^3} \approx 17$. Here we have equated the expressions $\tau_S \simeq 2(L_\parallel/\lambda_0)^4$ extracted from Fig. 28(b) and $\tau_S^\perp \simeq 10^4(L_\perp/\lambda_0)$, which we read off from Fig. 38(b). We note, however, that the crossover time $\tau_S^\perp$ appears in a stretched exponential, while τ_S describes a simple exponential approach to saturation. The calculation shows that for $L \gtrsim L_{\mathrm{eq}} = 17\lambda_0$ the intensity S_θ^* will saturate not because the dominant wave length parallel to the stripe pattern reaches the system size, but rather because of confinement in the perpendicular direction. This would be observable as a change of the cross-over time from $\tau_S \sim L^4$ to $\tau_S \sim L$ for L sufficiently large. The exact mechanism causing the saturation of orientation fluctuations due to perpendicular confinement is not clear yet, as there is no single relationship between time and length scales. While the continuous growth of the dominant wave length $\lambda^* \sim t^{0.25}$ describes the evolution parallel to the stripes, the scaling of the cross-over time $\tau \sim L_\perp$ suggests the presence of a growing length scale $\xi_\perp \sim t$ perpendicular to the stripes, at least for times $t \ll \tau_S^\perp$. Furthermore, we note that, contrary to the two types of confinement addressed before, the systems with $L_\perp \ll L_\parallel$ do not reach a stationary state in the accessible time frame.

C. Discussion and summary

To recapitulate, we have presented a detailed investigation of the non-equilibrium dynamics of a stripe-forming system evolving from an ordered state under the influence of noise. Using the structure factor of the stripe orientation $S_\theta(\mathbf{k}, t)$, we indentified a growing modulation length λ^* of the orientation field parallel to the stripes. In finite systems, the intensity S_θ^* corresponding to this modulation generally saturates as a function of the system size. We have found that square systems ($L_\perp = L_\parallel$) and systems containing many short stripes

($L_{\|} \ll L_{\perp}$) exhibit the same finite-size scaling behavior of the averaged correlation function $\overline{C}_{\theta}(r_{\|}, t)$, as expressed by the scaling forms, Eqs. (14) and (15). In particular, the relaxation time diverges as $\tau_S \sim L_{\|}^4$, indicating that even moderately large stripe-forming systems remain out of equilibrium for a very long time. Conversely, this means that the coarsening dynamics stops once the cross-over time has been exceeded, resulting in stationary behavior of the two-time autocorrelation function (see Fig. 26). These results complete the picture of aging in the stripe-forming system due to growing length scales [44]. As it turns out, the dynamics is driven by the increase of the dominant modulation length $\lambda^* \sim t^{0.25}$ parallel to the stripe pattern. Simultaneously, the orientational correlation length perpendicular to the stripes grows as $\xi_{\theta}^{\perp} \sim t^{0.5}$, but only up to a limit determined by the system size $L_{\|}$ [see Eq. (16)]. Fig. 39 summarizes the temporal evolution due to the two different growing length scales. The orientation field $\theta(\mathbf{r}, t)$ is shown at different times t, overlaid with stream lines representing the detailed shape of the stripes [Fig. 39(a) and (b)]. The two length scales we identified, λ^* and $\xi_{\theta}^{\perp}$, are plotted as a function of time in Fig. 39(c).

A possible explanation of these phenomena proceeds along the following lines: Bending the stripes carries an energy cost, which increases as the radius of curvature gets smaller. Thus, strong deviations from the initial orientation are only possible if the orientation changes slowly in the direction parallel to the stripes. Therefore, a growing length scale parallel to the stripes is necessary if we assume that an increasing amplitude of the orientation fluctuations is entropically favored. Once this length scale reaches the system size, the amplitude of the orientation fluctuations saturates. On the other hand, increasing correlations perpendicular to the stripes imply that neighboring stripes are in phase with respect to their orientation. This can be achieved regardless of the system size perpendicular to the stripes. However, the saturation of $\xi_{\theta}^{\perp}$ as a function of $L_{\|}$ indicates that there exists a mechanism which decorrelates neighboring stripes over long enough distances. We presume that the degree of correlations in the perpendicular direction increases with the amplitude of the fluctuations parallel to the stripes, thus coupling the coarsening phenomena parallel and perpendicular to the stripes.

In contrast to the aforementioned systems, a finite system size perpendicular to the stripes has a comparatively weak effect on the dynamics in systems containing few but very long stripes ($L_{\perp} \ll L_{\|}$). The growth of the dominant wave length λ^* is not impeded, whereas the intensity S_{θ}^* slowly approaches saturation as a stretched exponential. We have proposed a

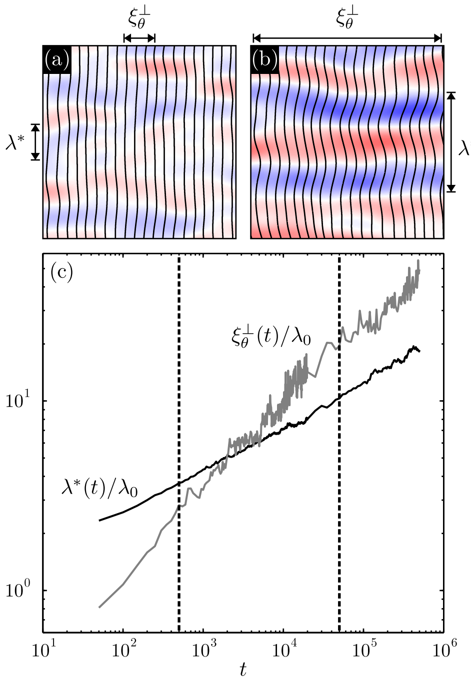

FIG. 39. Growing length scales in the stripe-forming system. (a, b) Portions ($20\lambda_0 \times 20\lambda_0$) of the coarse-grained orientation field $\theta(\mathbf{r}, t)$ at different times $t = 5 \cdot 10^2$ (a) and $t = 5 \cdot 10^4$ are shown for a system with $L = L_\perp = L_\parallel = 55\lambda_0$. The same color scale as in Fig. 25(c) is used. The black lines are stream lines representing the vector field $(\cos\theta, \sin\theta)^\intercal$, where the angle θ has been magnified by a factor of 20. The arrows indicate the values of the dominant wave length λ^* and the orientation correlation length $\xi_\theta^\perp$. (c) λ^* and $\xi_\theta^\perp$ are plotted as a function of time. The dashed lines indicate the times corresponding to (a) and (b). We note that the correlation length $\xi_\theta^\perp$ cannot be reliably determined for times $t \gtrsim 5 \cdot 10^4$, since the spatial correlation function changes from an exponential to a power-law decay [44].

scaling form for the quantity S_θ^*, but were unable to identify consistent scaling behavior in the averaged correlation function $\overline{C}_\theta(r_\parallel, t)$.

In this work, we have studied the structure factor of the orientation and the corresponding averaged correlation function. Focusing on their respective finite-size scaling behavior, we have found that the non-equilibrium dynamics of the stripe-forming system is characterized by two growing length scales parallel and perpendicular to the stripe pattern, which describe the anisotropic fluctuations of the orientation field. Given the simplicity and wide applicability of the model we consider, it will be interesting to see whether this aging dynamics and finite-size scaling can also be observed in experiments.

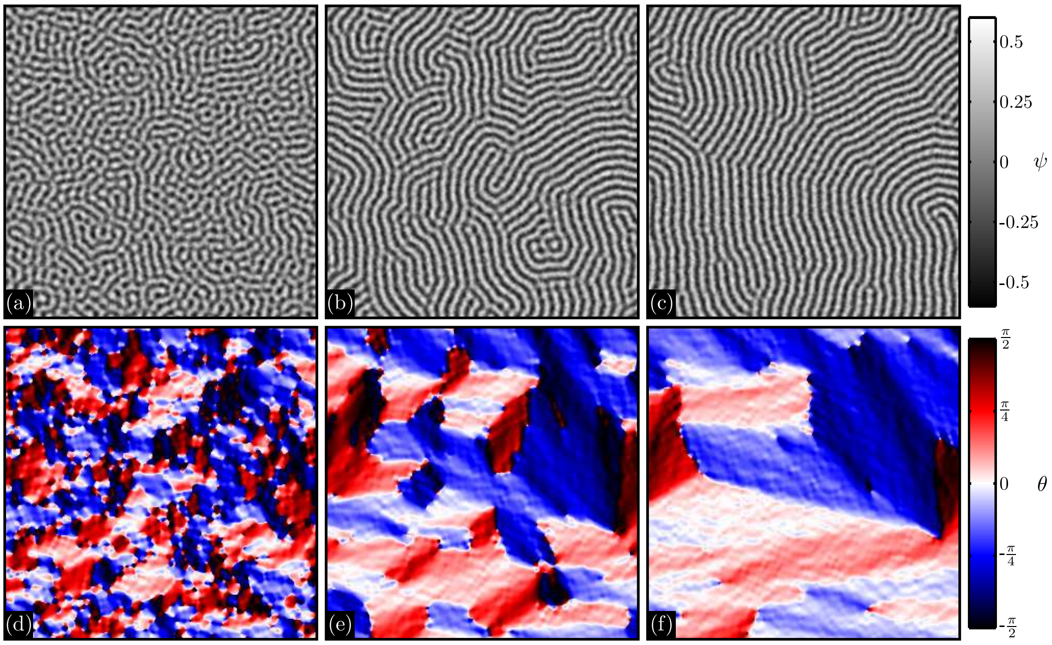

FIG. 40. Domain growth after a quench from homogeneous initial conditions. (a–c) The concentration field $\psi(\mathbf{r},t)$ is shown for times $t = 10^2$, 10^3, and 10^4. (d–f) The corresponding orientation field $\theta(\mathbf{r},t)$ is presented. The size of the snapshots is 300×300.

V. EVOLUTION FROM A HOMOGENEOUS INITIAL STATE

A. Introduction

In this section, we will discuss the dynamics of the stripe-forming system, given by Eq. (3), when it is supplied with a homogeneous initial condition, i.e. $\psi(\mathbf{r}, t = 0) = 0$. This procedure is used to model a quench from a high-temperature mixed state to a final state below the critical temperature. It is the most common approach when studying phase separation and phase ordering phenomena [16]. Quenches from a mixed state have also been investigated in stripe-forming systems, including the Swift-Hohenberg equation [38, 45, 47, 49, 50, 52, 53, 125, 164] as well as model B with Coulomb interactions [38, 64–67, 69, 163, 165, 166], which we consider here. The ordering process after the quench is usually described in terms of a growing length scale $\ell(t)$ representing the extent of order within the pattern.

Below, will confirm previous results for the scaling behavior of $\ell(t)$ and compare different approaches for extracting this length scale from the simulation data. Furthermore, we will investigate the aging behavior of the orientation autocorrelation function $C_\theta(t, t_\mathrm{w})$ (Sec. V C).

B. Domain growth

First, we will give a brief introduction to the phenomenology after a quench. There is an initial regime called microphase separation, where the two components demix on a length scale $\ell \lesssim \lambda_0$, driven by the linear instability against perturbations with a finite wave vector [65][167]. The result is a labyrinthine pattern of short stripes. These stripes subsequently form domains with uniform orientation, separated by grain boundaries and topological defects, as shown in Fig. 40. Domain growth then proceeds in a self-similar fashion, similar to macroscopic phase ordering [16]. In the following, we will focus on the latter process. It has been confirmed that dynamical scaling holds in this regime [38], which implies that the typical linear dimension of the pattern is described by a single length scale $\ell(t)$, found to depend on time as $\ell(t) \sim t^y$ [168]. However, the value of the exponent y seems to depend on the specific measure for $\ell(t)$ that is being considered, on the distance from the onset of stripe formation (i.e., the value of Γ), and on whether noise is incorporated ($\eta > 0$) into the simulation or not ($\eta = 0$). Growth exponents y in the range $\frac{1}{5} \leq y \leq \frac{1}{3}$ have been reported [38, 47, 49, 50, 52, 125], while other authors have argued that $y = \frac{1}{2}$ should be the long-time limit [45, 46, 169]. Notably, in Ref. 38, simulations of the Swift-Hohenberg equation and of model B with Coulomb interactions have been compared. The authors reported equal growth exponents for the two systems, with $y = 0.3$ describing the growth of the orientational correlation length ξ_θ at finite noise strength.

In the following, we will report on simulations of linear size $L = 1024$ with $\Delta x = 1$ and $\Delta t = 0.1$ at zero ($\eta/\eta_\mathrm{c} = 0$) and finite ($\eta/\eta_\mathrm{c} = \frac{1}{3}$) noise strength, starting from homogeneous initial conditions. All results have been averaged over ten independent realizations. The control parameter $\Gamma = 0.2$, as in Ref. [38].

The orientational correlation length ξ_θ has often been used as a measure for $\ell(t)$. It can be extracted from the decay of the spatial orientation correlation function $C_\theta(\mathbf{r}, t)$, where ξ_θ is defined as the value of the distance r for which the azimuthally averaged correlation function $C_\theta(r, t)$ first falls below a threshold α [38]. Examples for $C_\theta(r, t)$ at different times are shown in Fig. 41. Averaging over the angular dependence of $C_\theta(\mathbf{r}, t)$ is justified because

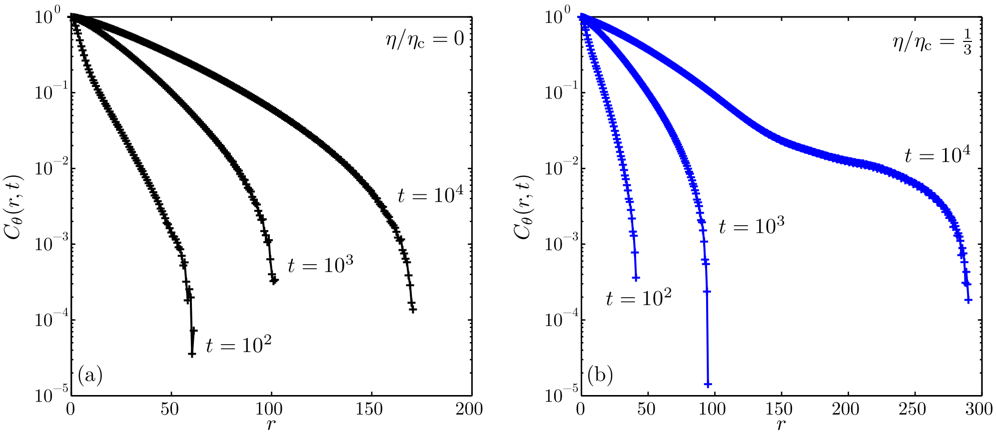

FIG. 41. Evolution of the spatial orientation correlation function $C_\theta(r,t)$ for (a) $\eta/\eta_c = 0$ and (b) $\eta/\eta_c = \frac{1}{3}$. The time $t = 10^2$, 10^3, and 10^4 (bottom to top).

the system is still isotropic during the time span we consider, i.e., the stripe pattern consists of many domains with different orientations. We have plotted the orientational correlation length ξ_θ as a function of time in Fig. 42(a, b) for zero and finite noise strength. In both cases, ξ_θ grows as a power law $\xi_\theta \propto t^y$ for $t \gtrsim 10^3$, with no significant dependence on the threshold α. The exponent y has been extracted by fitting the data for $\alpha = 0.2$ in the range $10^3 \leq t \leq 10^4$, resulting in $y = 0.24$ and 0.30 for $\eta/\eta_c = 0$ and $\eta/\eta_c = \frac{1}{3}$, respectively. These values are compatible with Ref. 38, where $y = 0.25$ and $y = 0.3$ have been reported.

We have also computed the excess free energy density $\Delta\rho_{\mathcal{F}}$ [49, 52]. For $\eta/\eta_c = 0$, the same definition as before applies (see Sec. III B 3), while for non-zero η, $\Delta\rho_{\mathcal{F}} \equiv (\mathcal{F} - \mathcal{F}_\eta)/L^2$, where $\mathcal{F}_\eta$ represents the value of $\mathcal{F}$ observed for $\eta/\eta_c = \frac{1}{3}$ at late times ($t = 5 \cdot 10^5$) when starting with ordered initial conditions. In Fig. 42(c), we see that $\Delta\rho_{\mathcal{F}}$ decays as a power law for $t > 1000$, with exponents 0.27 and 0.31 for zero and finite noise strength, respectively. Finally, we have computed the density of dislocations ρ_{Disloc}, following the procedure described before (Sec. III B 3). Note that this method does not discriminate between different types of defects. For instance, a grain boundary separating domains of stripes with different orientations can be seen as a string of point defects, i.e., dislocations. The results are shown in Fig. 42(d). Similar to the excess free energy density, the defect density decays with a power law following an initial regime observed for $t < 1000$. The corresponding exponents are similar as well, with values of 0.28 and 0.33 for zero and finite noise strength, respectively. This might seem surprising, as the dimension of the dislocation density $[\rho_{\text{Disloc}}] = [\ell^{-2}]$, which

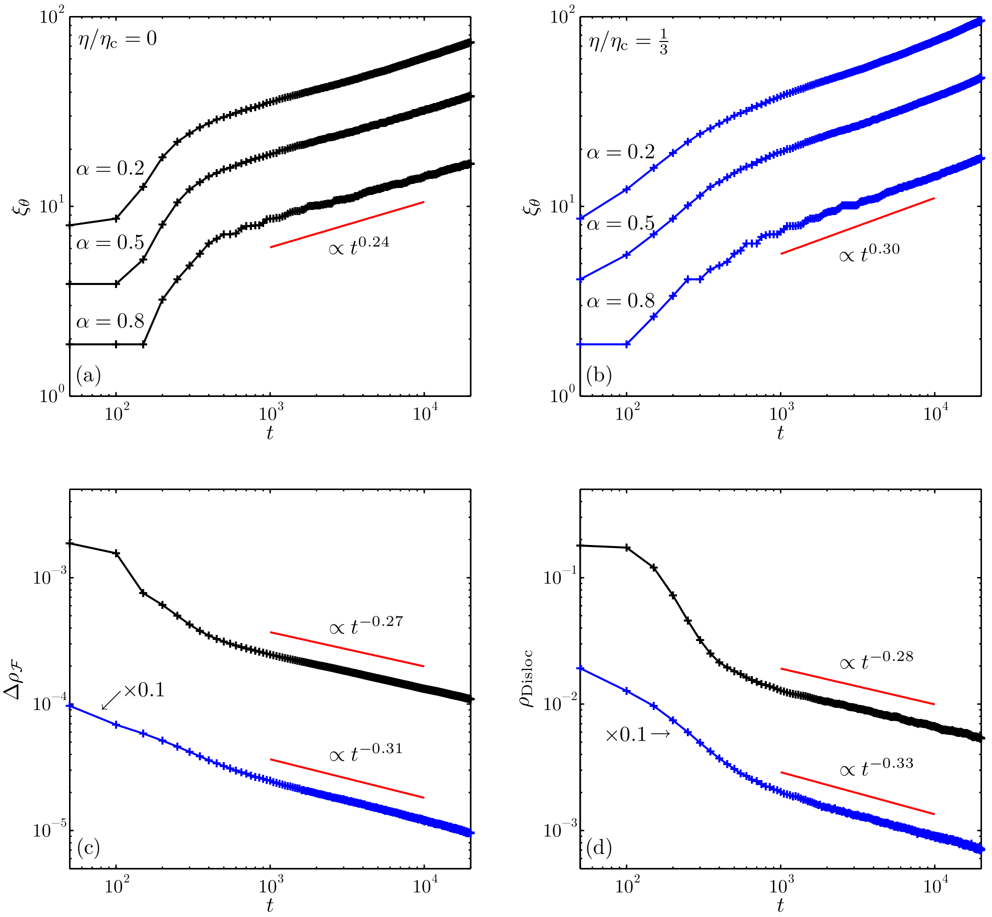

FIG. 42. Scaling behavior of different quantities after a quench from homogeneous initial conditions. Black (blue) curves denote $\eta/\eta_c = 0$ $(\frac{1}{3})$. The straight red lines correspond to power laws with the indicated exponents. (a, b) Orientational correlation length ξ_θ, computed for different values of the threshold α. (c) Excess free energy density $\Delta\rho_{\mathcal{F}}$. (d) Density of dislocations ρ_{Disloc}. For clarity, the curves in (c) and (d) have been shifted in magnitude as indicated.

implies that $\rho_{\mathrm{Disloc}}^{-1/2}$ should reflect the average distance between defects, as opposed to $\rho_{\mathrm{Disloc}}^{-1}$. However, as mentioned before, the domain growth within the stripe pattern is dominated by the annihilation of grain boundaries [52], which in turn are built from dislocations. This renders the mutual distance between dislocations less meaningful.

While so far we have considered derived quantities, it is also possible to extract $\ell(t)$ directly from the concentration field $\psi(\mathbf{r}, t)$ using the azimuthally averaged spatial correlation function $C_\psi(r, t) \equiv \langle \psi(\mathbf{r}, t)\psi(\mathbf{r}' + \mathbf{r}, t)\rangle_{\zeta,\mathbf{r}'}$. Its functional form for models with competing short- and long-range interactions has been derived using a Hartree approximation by Mulet

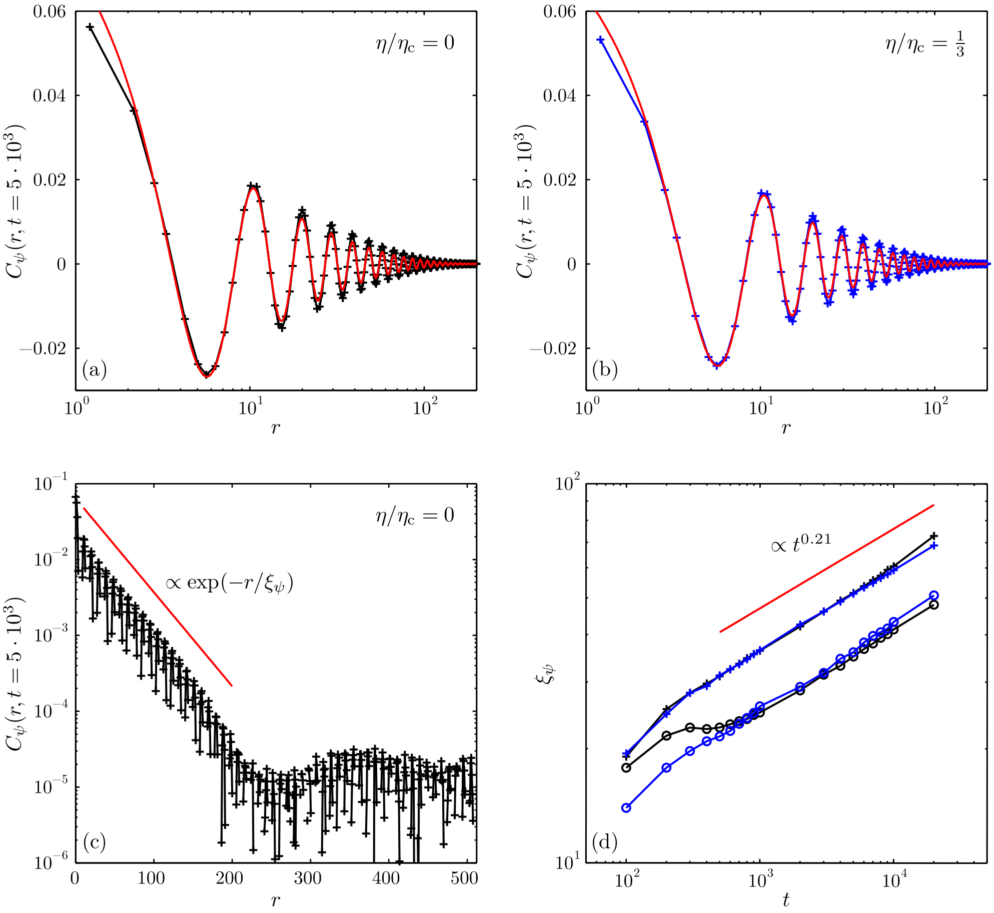

FIG. 43. Evolution of spatial concentration correlations. (a, b) Spatial correlation function $C_\psi(r,t)$ for $t = 5 \cdot 10^3$ and zero and finite noise strength η, respectively. Fits with Eq. (17) are shown in red. (c) Positive values of $C_\psi(r, t = 5 \cdot 10^3)$ plotted on a semilogarithmic scale. The red line represents an exponential. (d) Correlation length $\xi_\psi(t)$ extracted by fitting $C_\psi(r,t)$ with Eq. (17) (+) as well as by fitting an exponential to the maxima of $C_\psi(r,t)$ (○). Data are shown for both, $\eta/\eta_c = 0$ and $\eta/\eta_c = \frac{1}{3}$. The straight red line is a power law drawn as a guide to the eye.

and Stariolo [170]. For temperatures $T > 0$ and $d = 2$ dimensions, these authors find

$$C_\psi(r) \propto \cos(2\pi/\lambda_0 r - \varphi)\exp(-r/\xi_\psi) r^{-\frac{1}{2}} \tag{17}$$

in the static limit $t \to \infty$, where φ is a parameter representing a phase shift, and ξ_ϕ is the correlation length. A slightly different form for $C_\psi(r,t)$ had been obtained earlier, based on a perturbation technique [48]. We will use least-square fits with Eq. (17) to extract the (now time-dependent) correlation length ξ_ψ from $C_\psi(r,t)$. The results are shown in Fig. 43(a) and (b). Eq. (17) provides a satisfactory fit to the correlation function $C_\psi(r,t)$ for both, vanishing and finite noise strength η within the time range we consider. This is not obvious, as a different functional form has been derived in Ref. [170] for the case $T = 0$, where the exponential in Eq. (17) is replaced by an algebraic decay. However, plotting $C_\psi(r,t)$ for η/η_c on a semilogarithmic scale clearly shows an exponential decay of the envelope [Fig. 43(c)]. The time-dependent correlation length $\xi_\psi(t)$ is plotted in Fig. 43(d), obtained from both, fits to Eq. (17) as well as fitting the local maxima of $C_\psi(r,t)$ with an exponential $\propto \exp(-r/\xi_\psi)$. We have included the latter approach because it does not rely on assumptions about the detailed form of the corrrelation function.

Two conclusions may be drawn: First, both methods we implemented yield the same time dependence of the correlation length ξ_ψ, which grows at late times as a power law $\xi_\psi \sim t^{y_\psi}$ with an exponent $y_\psi \approx 0.2$. Second, a finite noise strength does not have a significant influence on the growth of ξ_ψ for $t \gtrsim 1000$. Comparing these results with the literature, we find agreement with the results of Ref. [38] for $\eta = 0$, where $y_\psi = \frac{1}{5}$ was reported based on the scaling of the structure factor, which is given by the Fourier transform of $C_\psi(\mathbf{r},t)$. However, we observe the same exponent for $\eta > 0$, whereas a value of $\frac{1}{4}$ was found in Ref. [38] for a finite noise strength. On the other hand, there is a strong disagreement with the value $y_\psi \approx 0.5$ reported in Ref. [48], also based on fitting $C_\psi(r,t)$.

To recapitulate, we have studied the growing length scale $\ell(t)$ in the stripe-forming system after a quench from homogeneous initial conditions. There are a number of possible definitions for $\ell(t)$. While we always observe power-law behavior at late times, this ambiguity makes it difficult to pin down the exact value of the growth exponent. However, our results are compatible with some of those reported in the literature. Furthermore, when comparing the orientational correlation length ξ_θ, the excess free energy density $\Delta\rho_{\mathcal{F}}$, and the dislocation density ρ_{Disloc}, we observe a consistent difference (≈ 0.05) between the exponents at zero and finite noise strength, respectively. On the other hand, the correlation length ξ_ψ computed directly from the concentration field $\psi(\mathbf{r},t)$, yields a significantly smaller value of the exponent y_ψ, which does not change when noise is added to the system. We note that there is no consensus yet in the literature on how to interpret the behavior of the different measures for the length scale $\ell(t)$.

C. Aging

The scaling hypothesis, i.e., the existence of a single length scale $\ell(t)$ growing as a power law of time, has been crucial for the description of domain growth processes [16]. It has been recognized a long time ago that this implies the following scaling form of the corresponding autocorrelation function, valid for times $1 \ll t_{\mathrm{w}} \ll t$ [15, 16, 171]:

$$C(t, t_{\mathrm{w}}) \sim f(t/t_{\mathrm{w}}), \tag{18}$$

where $f(x)$ is a scaling function, and the two-time dependence only enters *via* the ratio $x \equiv t/t_{\mathrm{w}}$. This relation has subsequently been confirmed for a number of systems exhibiting domain growth [18, 21]. Eq. (18) is equivalent to the scaling form encountered in Sec. III A, Eq. (11), for the special case $b = 0$. The scaling function $f(x)$ is expected to decay as a power law for large arguments [97, 98, 172].

In the preceding section, we have demonstrated the existence of a growing length scale $\ell(t)$ in the stripe-forming system after a quench form homogeneous initial conditions. Now we are interested in the behavior of the orientation autocorrelation function $C_\theta(t, t_{\mathrm{w}})$. In Fig. 44(a), we plot $C_\theta(t, t_{\mathrm{w}})$ as a function of t/t_{w} in order to check if Eq. (18) holds. We only present data for which both, t and t_{w} are in the scaling regime ($t_{\mathrm{w}} > 10^3$, cf. the preceding section). There is a collapse of the data onto individual curves for $\eta/\eta_{\mathrm{c}} = 0$ and $\eta/\eta_{\mathrm{c}} = \frac{1}{3}$, respectively. While minor flucutations are prensent, scaling of the form given by Eq. (18) is observed over more than a decade in t/t_{w}. The scaling function $f(t/t_{\mathrm{w}})$ resembles a power law of t/t_{w} for both, vanishing and finite noise strength. The exponents, 0.22 and 0.27, respectively, are similar to the growth exponents y computed from the the evolution of the orientational correlation length ξ_θ, but slightly smaller.

Another way to probe the scaling behavior of the autocorrelation function is to choose a small fixed waiting time t_{w} and plot $C_\theta(t, t_{\mathrm{w}})$ as a function of t [98]. Scaling begavior is then expected for late times t. The results of this approach are shown in Fig. 44(b). For $\eta/\eta_{\mathrm{c}} = 0$, the correlation with the initial condition is plotted ($t_{\mathrm{w}} = 0$), whereas data for $t_{\mathrm{w}} = 50$ are presented for both, zero and finite noise strength. Since the dynamics is deterministic in the absence of noise, the orientation field $\theta(\mathbf{r}, t)$ retains correlations with its initial state. In contrast, these correlations decay rapidly for $\eta > 0$, as the noise strength is comparable to the amplitude of $\psi(\mathbf{r}, t)$ at early times. For both waiting times, a power-law decay is observed for $t \gtrsim 10^3$. The exponents extracted by least-squares fitting a power law to the

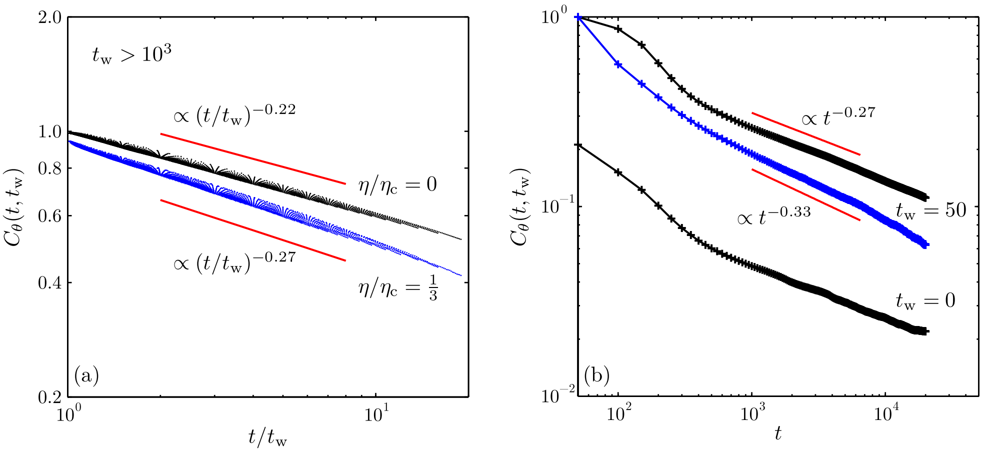

FIG. 44. Scaling of the orientation autocorrelation function. (a) $C_\theta(t, t_{\mathrm{w}})$ is plotted as a function of t/t_{w} for systems quenched from homogeneous initial conditions. Only data for $t_{\mathrm{w}} > 10^3$ are shown. Black (blue) points denote $\eta/\eta_{\mathrm{c}} = 0$ $\left(\frac{1}{3}\right)$. The red lines correspond to power laws. (b) $C_\theta(t, t_{\mathrm{w}})$ is plotted as a function of t for short waiting times $t_{\mathrm{w}} = 0$ (bottom) and $t_{\mathrm{w}} = 50$ (top).

data are slightly larger than those extracted from the scaling function $f(t/t_{\mathrm{w}})$ [Fig. 44(a)], the difference being about 0.05. We presume these differences to be a result of insufficient statistics.

In summary, our results confirm the picture of aging due to domain growth for the stripe-forming system quenched from a homogeneous initial state. The orientation autocorrelation function scales as $C_\theta(t, t_{\mathrm{w}}) \sim f(t/t_{\mathrm{w}})$ for both, zero and finite noise strength. The scaling function f decays as a power law characterized by an exponent similar in magnitude to the exponent y describing the growth of the correlation length ξ_θ.

Non-equilibrium dynamics in other modulated phases

Motivated by our findings of a slow dynamics and aging in the stripe-forming system, we have performed numerical simulations of other examples for modulated phases [23], which we will present in the second part of this thesis. We begin with a model for stripe formation similar to model B with Coulomb interactions, namely the Swift-Hohenberg equation (Sec. VI). The system is also prepared in an ordered state, and its evolution under the influence of noise is analyzed using the local stripe orientation (Sec. VI B). We also investigate the influence of a conservation law on the dynamics.

In Sec. VII, we turn to a generalization of the stripe-forming system we studied in the first part of this work, which allows for the formation of hexagonal patterns. The evolution from an ordered state under the influence of noise is analyzed in terms of the correlation functions of both, the orientation and the translation field (Sec. VII B). Furthermore, we address the role of topological defects (Sec. VII C) and investigate the dynamics of the system when the noise is switched off (Sec. VII D). Results describing the ordering process after a quench from a homogeneous initial state are presented in Sec. VII E. We conclude in Sec. VII F.

VI. THE SWIFT-HOHENBERG EQUATION

A. Introduction

The model defined by Eq. (3) is by far not the only one used to describe stripe-forming systems [34, 37, 39]. When restricting the scope to simple Langevin-type equations, there is at least one other important system, namely the Swift-Hohenberg (SH) equation, which has been developed to model Rayleigh-Bénard convection [53]. It is defined by the effective free energy functional [173]

$$\mathcal{F}_{\mathrm{SH}}[\psi] = \int \mathrm{d}^2 r \left\{ -\frac{\epsilon}{2}\psi(\mathbf{r},t)^2 + \frac{1}{4}\psi(\mathbf{r},t)^4 - k_0^2[\nabla\psi(\mathbf{r},t)]^2 + \frac{1}{2}[\nabla^2\psi(\mathbf{r},t)]^2 \right\}, \tag{19}$$

where the control parameter ϵ is the dimensionless distance from the onset of convection, and k_0 is the wave vector favored by the stripe pattern. The dynamic equation is given by

$$\frac{\partial\psi}{\partial t} = -\frac{\delta\mathcal{F}_{\mathrm{SH}}}{\delta\psi} + \zeta, \tag{20}$$

which represents a simple relaxational dynamics without conservation of the order parameter. Although it has the same form as model A [54], the SH system does not belong to this class [53]. Similar to model B with Coulomb interactions, it can be classified as a pattern-forming system of type $\mathrm{I_S}$ acording to Ref. 39. The Gaussian noise $\zeta(\mathbf{r},t)$ has zero mean and correlations $\langle\zeta(\mathbf{r},t)\zeta(\mathbf{r}',t')\rangle = 2\eta\delta(t-t')\delta(\mathbf{r}-\mathbf{r}')$. It is also possible to obtain a system with a conserved order parameter by inserting the free energy, Eq. (19), into the following dynamic equation, referred to as model B [54]:

$$\frac{\partial\psi}{\partial t} = \nabla^2\frac{\delta\mathcal{F}_{\mathrm{SH}}}{\delta\psi} + \zeta, \tag{21}$$

with $\langle\zeta(\mathbf{r},t)\zeta(\mathbf{r}',t')\rangle = -2\eta\delta(t-t')\nabla^2\delta(\mathbf{r}-\mathbf{r}')$. While Eq. (20) represents a paradigm for pattern-forming sytems [39], the model given by Eq. (21) has received renewed attention in recent years in the context of phase field models for crystal growth on atomic length scales [174, 175].

At this point, a few comments are in order regarding the conservation of the order parameter in the systems we study. Eq. (1) represents a conserved dynamics for general free energies $\mathcal{F}$. Nevertheless, the special form of the free energy given by Eq. (2), which was the subject of the first part of this work, breaks this mechanism. This is due to a cancellation effect between the interaction kernel $G(\mathbf{r}-\mathbf{r}')$ and the Laplacian in Eq. (1). Consequently, in

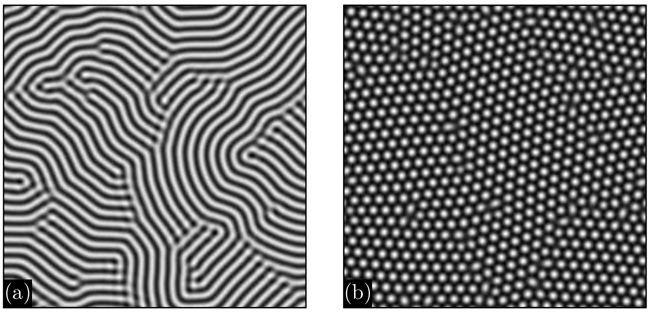

FIG. 45. Different patterns obtained from simulations of the Swift-Hohenberg equation with (a) non-conserved and (b) conserved order parameter, starting from identical homogeneous initial conditions with $\langle\psi(\mathbf{r},t=0)\rangle_{\mathbf{r}}=-0.25$. The time $t=1000$ and the noise strength $\eta=0$ in both cases.

model B with Coulomb interactions, the spatial average $\langle\psi(\mathbf{r},t)\rangle_{\mathbf{r}}$ decays exponentially with time if it is initially non-zero [176]. Therefore, the simulation results shown so far do not achieve a strict conservation of the order parameter.

In contrast, the conserved SH equation, Eq. (21), which uses the free energy given by Eq. (19), represents a dynamics which truly conserves the order parameter, i.e., $\partial_t\langle\psi(\mathbf{r},t)\rangle_{\mathbf{r}}=0$ for any inital condition. This is demonstrated in Fig. 45, where we show simulation results of both, the non-conserved and the conserved SH equation, starting from identical initial conditions for which $\langle\psi(\mathbf{r},t=0)\rangle_{\mathbf{r}}=-0.25$. In case of the non-conserved SH equation, the spatial average of the order parameter decays to zero, whereas the conserved system maintains the inital value. The formation of a stripe pattern is observed in the former case [Fig. 45(a)], while spherical domains with short-range hexagonal order appear in the latter case [Fig. 45(b)]. In this work we always prepare the system in a state with $\langle\psi(\mathbf{r},t=0)\rangle_{\mathbf{r}}=0$. Our results allow for a direct evaluation of the effect of a conservation law on the dynamics of a stripe pattern.

B. Evolution from an ordered initial state

In the following, we investigate aging effects in the orientation autocorrelation function and the dynamics of spatial orientation correlations in the Swift-Hohenberg equation with both, a conserved and a non-conserved order parameter. Proceeding analogously to the case of model B with Coulomb interactions (see Ref. 44 and Sec. III), we prepare both systems in an inital state corresponding to perfectly ordered stripes, and monitor the subsequent evolution under the influence of noise.

We have used the same numerical algorithm [73] as before to perform simulations on a two-dimensional lattice of size $L \times L$, with $L = 128\lambda_0$. The parameters $\epsilon = \frac{1}{4}$ and $k_0 = 2\pi/\lambda_0 = 1$, as in Ref. 38. In order to obtain a sufficient number of lattice sites per stripe wavelength λ_0, the lattice spacing has been set to $\Delta x = 2\pi/9$ [38]. In a single-mode approximation, where $\psi(\mathbf{r}) = A\cos(k_0 r_\perp)$, Eq. (19) is minimized by setting $A = 2\sqrt{\epsilon/3}$ and $k = k_0$ [52, 173]. These values were used for preparing the initial condition, for which $\langle\psi(\mathbf{r},t)\rangle_\mathbf{r} = 0$. The noise strength η was set to 0.01, which is far away from the order-disorder transition [45, 46].

Fig. 46 shows our results for the orientation autocorrelation function $C_\theta(t, t_\mathrm{w})$. In Fig. 46(a) and (b), $C_\theta(t, t_\mathrm{w})$ is plotted as a function of the time difference $t - t_\mathrm{w}$ for different waiting times t_w. For both, the non-conserved (a) and the conserved case (b), there is a strong dependence on the waiting time, with a slower decay of the correlation function for larger values of t_w. There is no significant difference in the shape of the curves for non-conserved and conserved order parameter, which both resemble power laws. As in Sec. III, we check for scaling of the form $C_\theta(t, t_\mathrm{w}) \sim t_\mathrm{w}^{-b} \cdot f(t/t_\mathrm{w})$. In Fig. 46(c), we have plotted $C_\theta(t, t_\mathrm{w})$ as a function of t_w while keeping the ratio $t/t_\mathrm{w} = 3/2$ constant. The data for the conserved SH equation have been shifted by half a decade, as the two curves would otherwise fall on top of each other. Both orientation autocorrelation functions decay as a power law $\propto t_\mathrm{w}^{-b}$. Least-squares fitting yields the exponent $b = 0.23$ in both cases. With this exponent, we are able to check the aforementioned scaling form by plotting the rescaled autocorrelation function $C_\theta(t, t_\mathrm{w}) \cdot t_\mathrm{w}^{b}$ as a function of $(t - t_\mathrm{w})/t_\mathrm{w}$ [Fig. 46(c)]. For both variants of the SH equation, a collapse of the data onto a single curve is obtained. Regarding the form of the scaling function $f(t/t_\mathrm{w})$, the same considerations apply as in the case of model B with Coulomb interactions. Both a stretched exponential and a product of power laws can be fitted to the data. We show a fit to $f(x) \propto x^{-\alpha} \cdot (x-1)^{-\beta}$, where $\alpha = 0.67$ and $\beta = 0.35$. These values are comparable to the ones obtained from model B with Coulomb interactions, where $\alpha = 0.89$ and $\beta = 0.34$ (see Sec. III A). Thus we conclude that the dynamics of the stripe orientation obtained from the non-conserved and conserved SH equations exhibits aging of the same form as observed in model B with Coulomb interactions. This is in line with results from previous works, where close similarities between model B with Coulomb

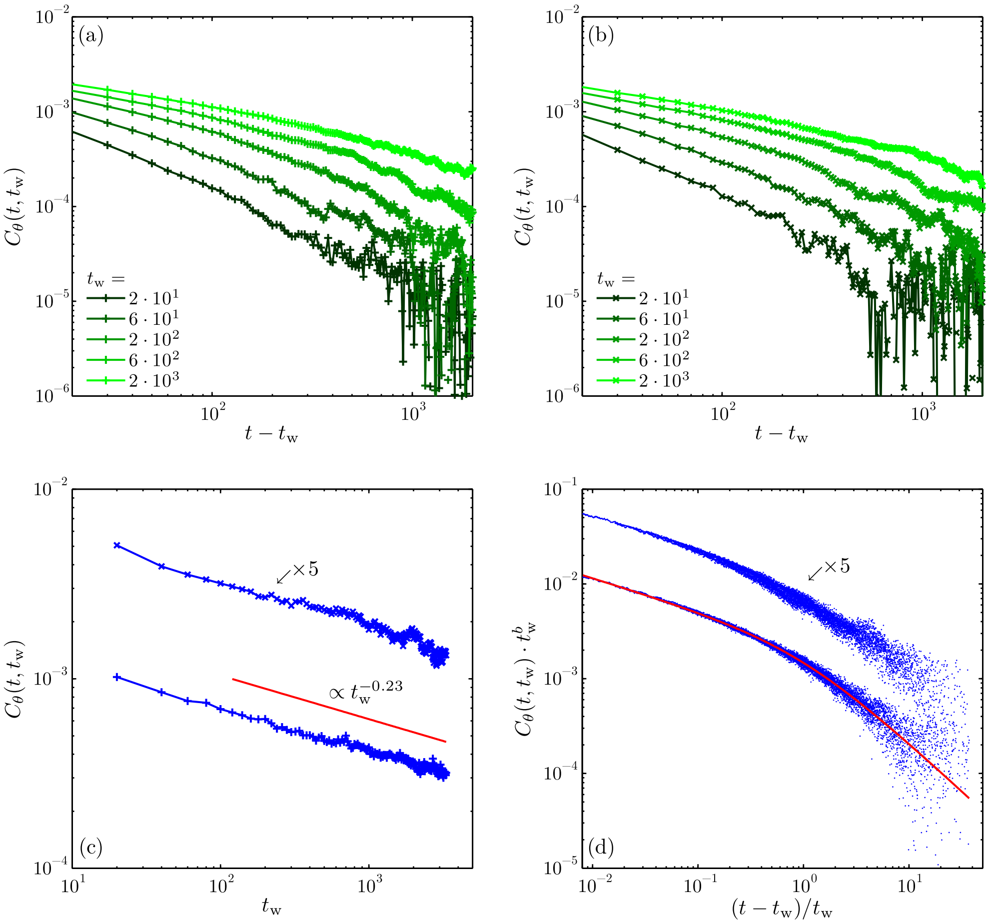

FIG. 46. Aging and scaling in the Swift-Hohenberg equation. (a, b) Orientation autocorrelation function $C_\theta(t, t_\mathrm{w})$ as a function of $t - t_\mathrm{w}$ for the Swift-Hohenberg equation with non-conserved (a, $+$) and conserved order parameter (b, $\times$). The waiting time t_w increases from bottom to top. (c) $C_\theta(t, t_\mathrm{w})$ as a function of t_w for a constant ratio $t/t_\mathrm{w} = 3/2$. The thin red line corresponds to a power law. (d) Rescaled autocorrelation function $C_\theta(t, t_\mathrm{w}) \cdot t_\mathrm{w}^b$ as a function of $(t - t_\mathrm{w})/t_\mathrm{w}$. The red line is a fit function discussed in the text. In (b) and (c), the data for the conserved case have been shifted for clarity.

interactions and the Swift-Hohenberg have been pointed out [38, 50, 177].

As in Sec. III, we have also investigated spatial correlations of the stripe orientation. The correlation function $C_\theta(\mathbf{r}, t)$ is anisotropic, comparable to the case of model B with Coulomb interactions discussed previously. We have plotted $C_\theta(\mathbf{r}, t)$ in the direction perpendicular to the stripes in Fig. 47(a). Clearly, orientation correlations grow as time progresses. The orientational correlation length $\xi_\theta^\perp$ has been extracted by fitting the data with exponential

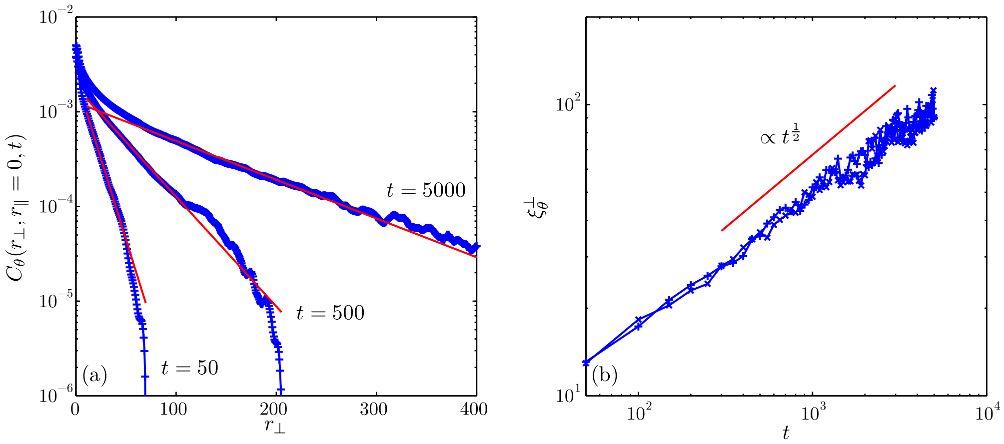

FIG. 47. Growth of spatial orientation correlations perpendicular to the stripes. (a) $C_\theta(r_\perp, r_\parallel, t)$ computed from the non-conserved SH equation is plotted for different times t. The red lines are fits with exponential functions $\propto \exp(-r_\perp/\xi_\theta^\perp)$. (b) Temporal evolution of the orientational correlation length $\xi_\theta^\perp$ for both, the conserved ($\times$) and the non-conserved ($+$) case. The red line represents a power law with an exponent $\frac{1}{2}$.

functions $\propto \exp(-\xi_\theta^\perp/r_\perp)$. The evolution of $\xi_\theta^\perp$ is shown in Fig. 47(b). For both, the conserved and the non-conserved case, the correlation length grows as a power law with an exponent ≈ 0.5.

We have also studied the spatial correlation function $C_\theta(\mathbf{r}, t)$ at very late times. The results are presented in Fig. 48. $C_\theta(\mathbf{r}, t)$ exhibits a slow evolution long after the begin of the simulation. There is a clear trend towards a power-law decay for large distances $r_\perp$, although the cross-over process from an exponential to a power-law shape is still in progress at the latest times we have attained [Fig. 48(a)]. This is probably due to the larger system size we consider compared to our simulations of model B with Coulomb interactions, where the typical system size $L = 55\lambda_0$. In contrast, $C_\theta(\mathbf{r}, t)$ decreases quickly parallel to the stripes within a distance $r_\parallel < 10$, and there is no significant relaxation at late times [Fig. 48(b)].

C. Conclusion

In summary, we have investigated the nonequilibrium dynamics of ordered stripe patterns described by the conserved and non-conserved variants of the Swift-Hohenberg equation. In

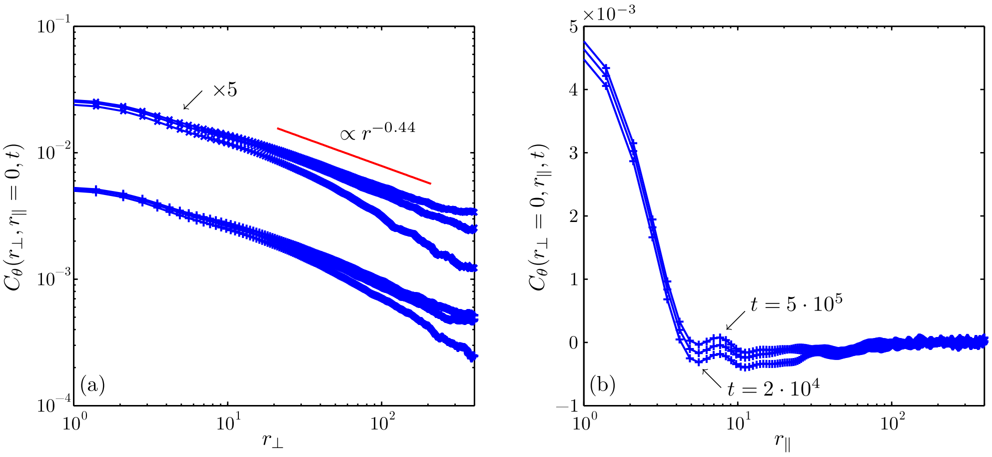

FIG. 48. Late-stage behavior of spatial orientation correlations. (a, b) Cuts through the spatial orientation correlation function $C_\theta(\mathbf{r}, t)$ perpendicular and parallel to the stripe pattern, respectively. In (a), data for the conserved (×, shifted by half a decade) and non-conserved SH equation (+) are shown. The red line is a power law drawn as a guide to the eye. In (b), $C_\theta(r_\perp = 0, r_\parallel, t)$ is shown only for the nonconserved case. In both panels, the time $t = 2 \cdot 10^4$, 10^5, and $5 \cdot 10^5$ (bottom to top).

both cases, the orientation correlation function behaves very similarly to the one obtained from model B with Coulomb interactions, discussed in Secs. III A and III B. The two-time correlation function fulfills the same scaling relation, Eq. (11), with the same form of the scaling function $f(t/t_\mathrm{w})$. The parameters describing $f(t/t_\mathrm{w})$ were found to be slighty different, but comparable in magnitude. Similarly, the spatial correlation function perpendicular to the stripes exhibits a growing orientational correlation length, with its evolution described by a power law with the exponent $\frac{1}{2}$. At very late times, there is a cross-over to a power-law decay of the spatial correlation function perpendicular to the stripes.

The influence of a conservation law on the properties of modulated phases has been discussed before [177–181]. It has been argued that the Laplacian in Eq. (21), the appearance of which is a consequence of the conservation law, should not bring about different behavior when compared to the non-conserved case. This can be made plausible in Fourier space. If the intensity $|\widehat{\psi}(\mathbf{k}, t)|^2$ is assumed to be sharply peaked at wave vectors with $|\mathbf{k}| = k_0$, the application of the Laplacian $-k^2$ just amounts to multiplication with a constant $-k_0^2$. Our results for the aging behavior of the SH equation support this claim, since we observe no significant differences between the conserved and the non-conserved case.

VII. HEXAGONAL PATTERNS

A. Introduction

In this section, we will investigate the non-equilibrium dynamics of a simple model for hexagonal patterns in two spatial dimensions. The model, to be defined below, has been widely used in computer simulations of the microphase separation in symmetric and asymmetric block copolymers [64, 66, 67, 69, 165]. Similar hexagon-forming systems, called phase-field crystals, have recently gained much attention in the context of crystallization processes on atomic length scales [174, 175, 182, 183]. Our focus will be on the relaxation from an ordered state under the influence of noise, in part motivated by our findings of aging in ordered stripe-forming systems (see Sec. III). Hexagonal patterns can be thought of as the superposition of three density waves [39], and are thus among the most simple examples of a modulated phase [23]. Preparing the system in an ordered state avoids the slow relaxation associated with topological defects, which is commonly encountered when the system is initially in a homogeneous state [16, 184]. Our approach bears some resemblance to a melting experiment, where the begin of the simulation marks a jump from zero to finite temperature. The melting of 2D crystals has attracted tremendous interest over the last decades [185–188]. Experimental studies devoted to this phenomenon have been performed in a variety of systems, such as thin films of block copolymers [189–193], colloidal particles [194–201], dusty plasmas [202–204], as well as driven granular matter [205]. It has long been known that crystals in two dimensions are unstable due to strong fluctuations [138]. The most successful theory for the melting process, referred to as the Kosterlitz-Thouless-Halperin-Nelson-Young (KTHNY) theory [100, 206–208], predicts a two-stage scenario, where each phase exhibits characteristic topological defects. For temperatures $0 < T < T_\mathrm{m}$, where T_m is the melting temperature, spatial translation correlations decay with a power law, while the system is orientationally ordered. This state is alternately called a 2D solid or a 2D crystal [209], and topological defects occur in the form of bound dislocation pairs [207]. For $T_\mathrm{m} < T < T_\mathrm{i}$, the system is in the hexatic phase [207], where unbound dislocations are prevalent. Translation correlations are now short-range, while orientation correlations are of power-law type. Finally, at a temperature T_i, dislocations unbind into disclinations, and all correlations become short-range. The system is now in an isotropic liquid state. Given the success of the KTHNY theory in explaining the properties of hexagonal patterns, we will make comparisons with our results where appropriate.

The remainder of this paper is organized as follows: Below, we will introduce the model and define the quantities used for analyzing the simulation data. In Sec. VII B, the main results for the dynamics starting from an ordered state are presented. Data for homogeneous initial conditions are shown in Sec. VII E, mainly for purposes of comparison with other works in the literature. A conclusion is given in Sec. VII F.

1. *Model and initial conditions*

The model we investigate here is almost identical to the one studied in the first part of this work (see Sec. II). A mixture of two components A and B is represented by the scalar concentration field $\psi(\mathbf{r}, t)$, where $\psi = \psi_A - \psi_B$. The free energy functional must be slightly modified to account for disparate volume fractions of the two components [55, 64]:

$$\mathcal{F}[\psi] = \int f_{\mathrm{GL}} d^d r + \frac{\Gamma}{2} \int [\psi(\mathbf{r}) - \psi_0)] G(\mathbf{r} - \mathbf{r}') [\psi(\mathbf{r}') - \psi_0)] d^d r, \tag{22}$$

where d is the spatial dimension, $f_{\mathrm{GL}} \equiv (\nabla\psi)^2 - \frac{1}{2}\psi^2 + \frac{1}{4}\psi^4$ represents the usual Ginzburg-Landau free energy density, $\Gamma > 0$ is a parameter controlling the long-range Coulomb interaction, and $G(\mathbf{r} - \mathbf{r}')$ is the Green's function satisfying $\nabla^2 G(\mathbf{r} - \mathbf{r}') = -\delta(\mathbf{r} - \mathbf{r}')$. The quantity ψ_0 is equal to the spatial average of the concentration field $\langle\psi(\mathbf{r})\rangle_{\mathbf{r}}$, which reflects the volume fraction f of one of the two components (say, ψ_A) in the system according to $\psi_0 \equiv 2f - 1$ [165]. As before, the evolution of the concentration field $\psi(\mathbf{r}, t)$ is described by the following dynamic equation, known as model B [54]:

$$\frac{\partial\psi}{\partial t} = \nabla^2 \frac{\delta\mathcal{F}[\psi]}{\delta\psi} + \zeta. \tag{23}$$

The Gaussian noise term $\zeta(\mathbf{r}, t)$ has zero mean and correlations $\langle\zeta(\mathbf{r}, t)\zeta(\mathbf{r}', t')\rangle = -2\eta\nabla^2\delta(\mathbf{r} - \mathbf{r}')\delta(t - t')$, where η is the noise strength.

Simulations were performed in $d = 2$ dimensions on a square lattice with periodic boundary conditions, using an efficient pseudo-spectral algorithm [73]. Time and space have been discretized, with $\Delta t = 0.1$ and $\Delta x = 1$, respectively. The system size $L_x \times L_y = 1710 \times 1150$, the control parameter $\Gamma = 0.2$ and the spatial average $\psi_0 = -0.1$. All results have been averaged over ten independent realizations. The lattice dimensions were chosen to be commensurate with the initial condition, which is prepared as follows. In a single–wave-number approximation, the concentration field in the ordered hexagonal phase can be written as the sum of three plane waves [210],

$$\psi(\mathbf{r}) = A \sum_{l=0}^{2} \cos(\mathbf{k}_l \cdot \mathbf{r}), \tag{24}$$

where A is the amplitude and the wave vectors $\mathbf{k}_l = k_0 \left(\begin{smallmatrix} \cos 2l\pi/3 \\ \sin 2l\pi/3 \end{smallmatrix}\right)$. The free energy, Eq. (22), is then minimized by setting $k_0 = \Gamma^{\frac{1}{4}}$ and $A = 2\sqrt{(1 - 12\psi_0^2/5 - 2\sqrt{\Gamma})/15} - \frac{2}{5}\psi_0$ [210]. The initial state for the given lattice dimensions contains 19292 circular domains located on a hexagonal lattice.

2. *Data analysis and correlation functions*

The results of our simulations are time series of the concentration field $\psi(\mathbf{r}, t)$. In the present section, we briefly describe the algorithms used to extract the relevant physical quantities, following established procedures (see, e.g., Refs. 189 and 211.

As a first step, the locations of the circular domains $\mathbf{r}_{\mathrm{D}}^{j}(t)$ are identified using a recently proposed algorithm [212]. Similar to other modulated phases, such as a stripe-forming system, a hexagonal phase may exhibit orientational as well as translational order. Due to the nature of the hexagonal lattice, the orientation $\theta(\mathbf{r}, t)$ can only be evaluated at certain points in the 2D plane. In practice, we first compute the Delaunay triangulation [213–215] of the set of points $\mathbf{r}_{\mathrm{D}}^{j}(t)$ representing the domain locations, which yields the edges connecting those points. The periodicity of the lattice is taken into account by also considering the eight neighboring replicas of the system, although more sophisticated algorithms exist [216–218]. We then obtain the orientation $\theta(\mathbf{r}_{\mathrm{e}}^{j}, t)$ at the midpoint of each edge by evaluating its angle with the x axis. In order to compute the correlation functions of the orientation, we interpolate the values $\theta(\mathbf{r}, t)$ on a regular lattice with the same dimensions as the simulation lattice. We have carefully checked that the interpolation step does not introduce any artifacts.

To investigate the non-equilibrium dynamics, we compute various spatio-temporal correlation functions. The two-time orientation autocorrelation function is defined as

$$C_\theta(t, t_\mathrm{w}) \equiv \mathrm{Re}\langle e^{6i[\theta(\mathbf{r},t)-\theta(\mathbf{r},t_\mathrm{w})]}\rangle_{\mathbf{r},\zeta} - \langle e^{6i\theta(\mathbf{r},t)}\rangle\langle e^{-6i\theta(\mathbf{r},t_\mathrm{w})}\rangle_{\mathbf{r},\zeta}, \quad (25)$$

where $\langle\cdot\rangle_{\mathbf{r},\zeta}$ stands for an average over both, spatial locations $\mathbf{r}$ and realizations of the noise ζ. The terms involving 6θ account for the sixfold symmetry of the pattern [207]. The spatial orientation correlation function is given by

$$C_\theta(\mathbf{r}, t) \equiv \mathrm{Re}\langle e^{6i[\theta(\mathbf{r}+\mathbf{r}',t)-\theta(\mathbf{r}',t)]}\rangle_{\mathbf{r}',\zeta} - \langle e^{6i\theta(\mathbf{r}+\mathbf{r}',t)}\rangle\langle e^{-6i\theta(\mathbf{r}',t)}\rangle_{\mathbf{r}',\zeta} \quad (26)$$

and the orientational order parameter $S \equiv \left|\langle e^{6i\theta(\mathbf{r},t)}\rangle_{\mathbf{r},\zeta}\right|$.

The translation correlation functions to be defined below are also based on the locations of the circular domains $\mathbf{r}_\mathrm{D}^j(t)$. First, we define the quantity $g(\mathbf{r}_\mathrm{D}^j) \equiv e^{i\mathbf{k}_0\cdot\mathbf{r}_\mathrm{D}^j}$, which is then interpolated on a regular lattice as in the case of the orientation correlation functions, yielding the function $g(\mathbf{r}, t)$. The wave vector $\mathbf{k}_0$ may be any one of the three wave vectors characterizing the initial condition [see Eq. (24)], over which we average. The translation autocorrelation function is defined as

$$C_\mathrm{T}(t, t_\mathrm{w}) \equiv \mathrm{Re}\langle g(\mathbf{r}, t)g^*(\mathbf{r}, t_\mathrm{w})\rangle_{\mathbf{r},\zeta} - \langle g(\mathbf{r}, t)\rangle\langle g^*(\mathbf{r}, t_\mathrm{w})\rangle_{\mathbf{r},\zeta}, \quad (27)$$

while the spatial translation correlation function is given by

$$C_\mathrm{T}(\mathbf{r}, t) \equiv \mathrm{Re}\langle g(\mathbf{r}+\mathbf{r}', t)g^*(\mathbf{r}', t)\rangle_{\mathbf{r}',\zeta} - \langle g(\mathbf{r}+\mathbf{r}', t)\rangle\langle g^*(\mathbf{r}', t)\rangle_{\mathbf{r}',\zeta}. \quad (28)$$

The translational order parameter $U \equiv |\langle g(\mathbf{r}, t)\rangle_{\mathbf{r},\zeta}|$.

Finally, using the Voronoi diagram [214, 215], which is the dual of the Delaunay triangulation [213], it is possible to determine the number of nearest neighbors of each domain, given by the number of edges of the corresponding polygon in the Voronoi diagram. Let N_i denote the number of sites with i neighbors present in a system. The defect density is then defined as $\rho_\mathrm{NN}^i \equiv N_i/(L_x L_y)$. An example of the data analysis procedure is shown in Fig. 49. The three steps shown are (a) locating the domains and obtaining the set of points $\mathbf{r}_\mathrm{D}^j(t)$, (b) obtaining the Delaunay triangulation to compute the local orientation, and (c) computing the Voronoi diagram in order to identify topological defects.

B. Evolution from an ordered initial state

In this section, we will present the results of our simulations of the hexagon-forming system starting with ordered initial conditions. Examples for the time series of the concentration

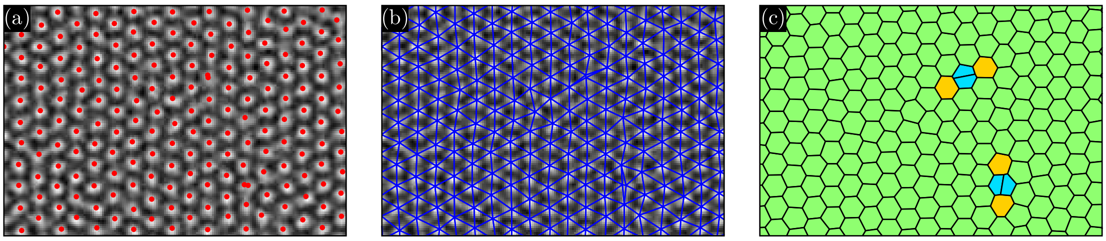

FIG. 49. Illustration of the data analysis procedure. (a) Concentration field $\psi(\mathbf{r},t)$. The positions of the circular domains where $\psi > 0$ have been marked with red dots. (b) The Delaunay triangulation of the set of vertices from (a) superimposed on the concentration field. (c) The corresponding Voronoi diagram. Two topological defects, specifically dislocations pairs, are visible.

field $\psi(\mathbf{r},t)$ thus obtained are shown in Fig. 50. While Fig. 50(a) shows the initial state, snapshots of systems having evolved at finite noise strengths for a time $t = 5000$ are presented in Fig. 50(b) and (c), with $\eta = 0.005$ and $\eta = 0.0125$, respectively. Although the patterns are perturbed by fluctuations, they retain a certain degree of order. In contrast, the pattern becomes disordered above a critical value of the noise strength, $\eta_{\rm c}$. The value of $\eta_{\rm c}$ seems to be comparable to that of the related stripe-forming system, where we found $\eta_{\rm c} = 0.02(03)$, as we observe a complete destruction of long-range order at $\eta = 0.025$ [Fig. 50(d)]. In the following, we will study the hexagon-forming system in the ordered phase, choosing a finite noise strength $0 < \eta < \eta_{\rm c}$.

1. *Order parameters*

First, we quantify the degree of order present in the hexagonal patterns by computing the translational order parameter U and the orientational order parameter S at late times t (Fig. 51). For clarity, we have plotted the deficiencies of the order parameters with respect to unity. The quantity $1-U$ grows slowly at first for both noise strengths, $\eta = 0.005$ and $\eta = 0.0125$, indicating the decay of translational order. For times $t \gtrsim 10^5$, $1-U$ tends to saturate. However, the order parameter exhibits rather strong fluctuations at late times, which makes it difficult to judge wether a stationary value has been reached or not [Fig. 51(a)]. In contrast, the quantity $1-S$ shows no sign of a decline over two decades in time [Fig. 51(b)], reflecting constant and finite orientational order. Furthermore, the value of S is always

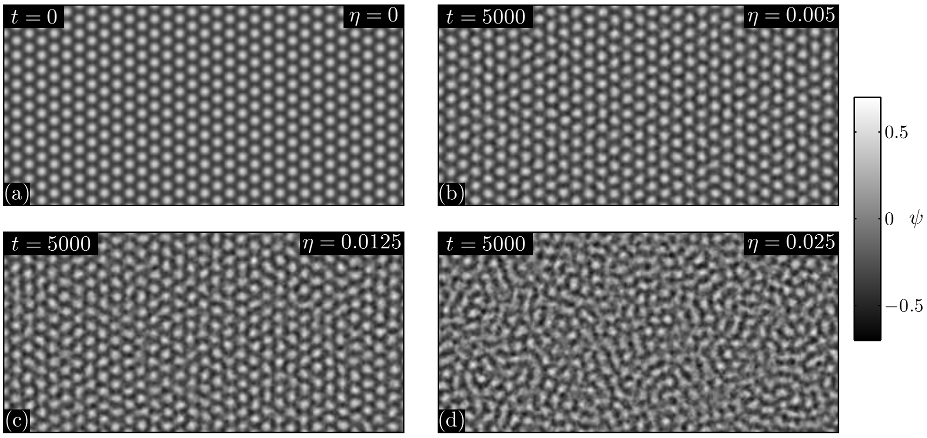

FIG. 50. Snapshots sized 150 × 300 of the concentration field $\psi(\mathbf{r}, t)$ at different times t and noise strengths η. (a) The ordered initial state. (b, c) The concentration field $\psi(\mathbf{r}, t = 5 \cdot 10^3)$ for two noise strengths $\eta < \eta_c$, (b) $\eta = 0.005$ and (c) $\eta = 0.0125$. (d) Snapshot of a system above the critical noise strength η_c ($\eta = 0.025$).

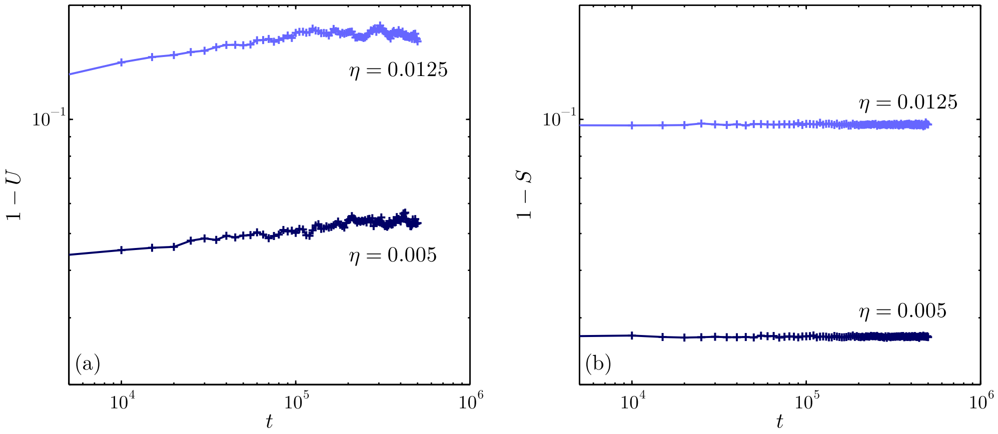

FIG. 51. (a) Translational order parameter U and (b) orientational order parameter S as a function of time for $\eta = 0.005$ (dark blue) and $\eta = 0.0125$ (light blue), respectively.

greater than that observed for U at the same noise strength. These results suggest that the system exhibits a slow dynamics related to the decay of translational order, but quickly reaches a stationary state with respect to orientational order. Below, we will explain this observation in terms of the spatio-temporal correlation functions.

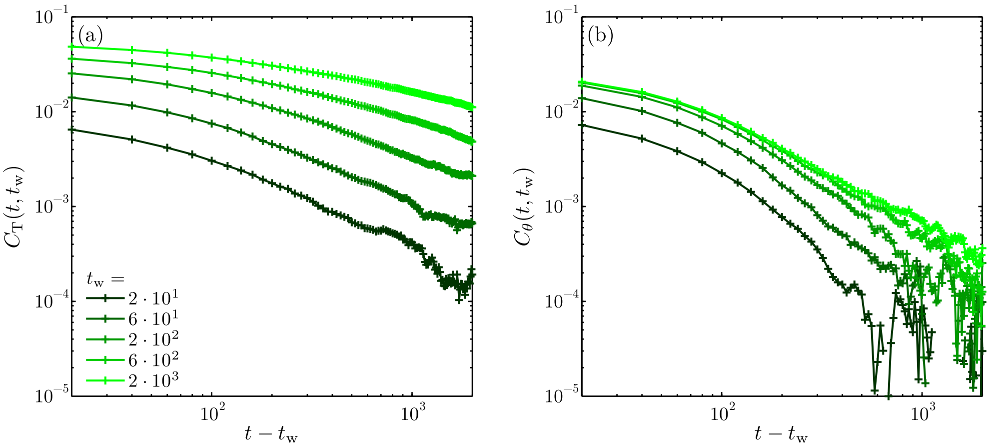

FIG. 52. Test for time translation invariance. The two-time autocorrelation functions (a) $C_\mathrm{T}(t,t_\mathrm{w})$ and (b) $C_\theta(t,t_\mathrm{w})$ are plotted as a function of the time difference $t-t_\mathrm{w}$. The waiting time t_w increases from dark to bright. The noise strength $\eta=0.005$.

2. *Two-time autocorrelation functions*

A clear sign for a non-equilibrium dynamics is the violation of time-translational invariance, i.e., the dependence of two-time correlation functions on both of their arguments [97]. We have performed a test for time translational invariance for both, the translation and the orientation autocorrelation function for a noise strength $\eta=0.005$ (Fig. 52). When plotted as a function of the difference $t-t_\mathrm{w}$, the translation autocorrelation function $C_\mathrm{T}(t,t_\mathrm{w})$ exhibits a pronounced dependence on the waiting time t_w as the latter is varied from $t_\mathrm{w}=2\cdot10^1$ to $t_\mathrm{w}=2\cdot10^3$ [Fig. 52(a)]. The longer the waiting time, the slower the relaxation. A different behavior is observed for the orientation autocorrelation function $C_\theta(t,t_\mathrm{w})$ [Fig. 52(b)]. While the magnitude of the correlation function grows significantly as the waiting time is increased from $t_\mathrm{w}=2\cdot10^1$ to $t_\mathrm{w}=2\cdot10^2$, the shape of the curves does not change much. Almost no further evolution takes place when going from $t_\mathrm{w}=2\cdot10^2$ to $t_\mathrm{w}=2\cdot10^3$. This indicates that the aging process slows down or even becomes interrupted at a rather early time.

Next, we investigate the scaling properties of the autocorrelation functions in order to understand the aging effect we have just found. In Fig. 53, the translation autocorrelation function $C_\mathrm{T}(t,t_\mathrm{w})$ is plotted as a function of the waiting time t_w for different ratios t/t_w. Apart from an initial increase, $C_\mathrm{T}(t,t_\mathrm{w})$ remains approximately constant for each of the different values of t/t_w. This suggests that the correlation function depends only on the ratio

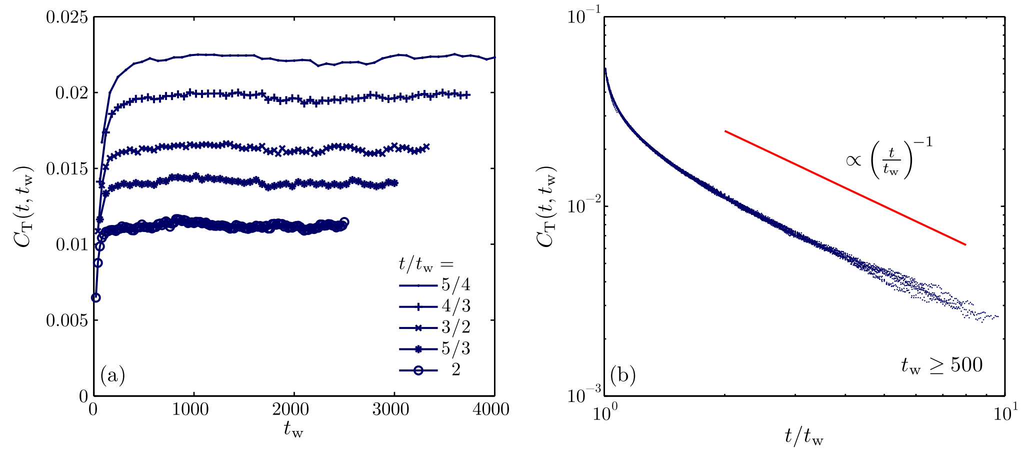

FIG. 53. Scaling of the translation autocorrelation function. (a) $C_\mathrm{T}(t,t_\mathrm{w})$ is shown as a function of the waiting time t_w for different ratios t/t_w. In (b), $C_\mathrm{T}(t,t_\mathrm{w})$ is plotted as a function of t/t_w, resulting in a collapse of the data. The red line is a power law $\propto (t/t_\mathrm{w})^{-1}$ drawn as a guide to the eye.

t/t_w, which is confirmed in Fig. 53(b). The data points for $C_\mathrm{T}(t,t_\mathrm{w})$ collapse onto a single curve when plotted as a function of t/t_w, where waiting times $t_\mathrm{w} < 500$ have been omitted to account for the transient initial regime. The translation autocorrelation function thus follows the scaling form $C_\mathrm{T}(t,t_\mathrm{w}) \propto f(t/t_\mathrm{w})$, which is typical for domain-growth processes below the critical temperature [16, 97]. For $t/t_\mathrm{w} > 2$, the decay of the scaling function $f(t/t_\mathrm{w})$ can be approximately described by a power law $\propto (t/t_\mathrm{w})^{-1}$.

A similar analysis can be performed for the orientation autocorrelation function $C_\theta(t,t_\mathrm{w})$. In Fig. 54(a), $C_\theta(t,t_\mathrm{w})$ is plotted as a function of the waiting time for different ratios t/t_w. In contrast to the translation autocorrelation function, it decays as a power law $\propto t_\mathrm{w}^{-1}$ for sufficiently long waiting times. Plotting the rescaled function $C_\theta(t,t_\mathrm{w}) \cdot t_\mathrm{w}$ for waiting times $t_\mathrm{w} \geq 400$ results in a collapse of the data onto a single curve, which can be fitted with the product of two power laws [Fig. 54(b)]. The data collapse indicates that the orientation autocorrelation function scales as $C_\theta(t,t_\mathrm{w}) \sim t_\mathrm{w}^{-1} \cdot f(t/t_\mathrm{w})$, a scaling form which is typical for critical coarsening [97]. However, our previous considerations point towards an interrupted aging process where the dynamics becomes stationary after a finite time (see Fig. 52). This pciture will be confirmed in the next section by analyzing the spatial orientation correlation function.

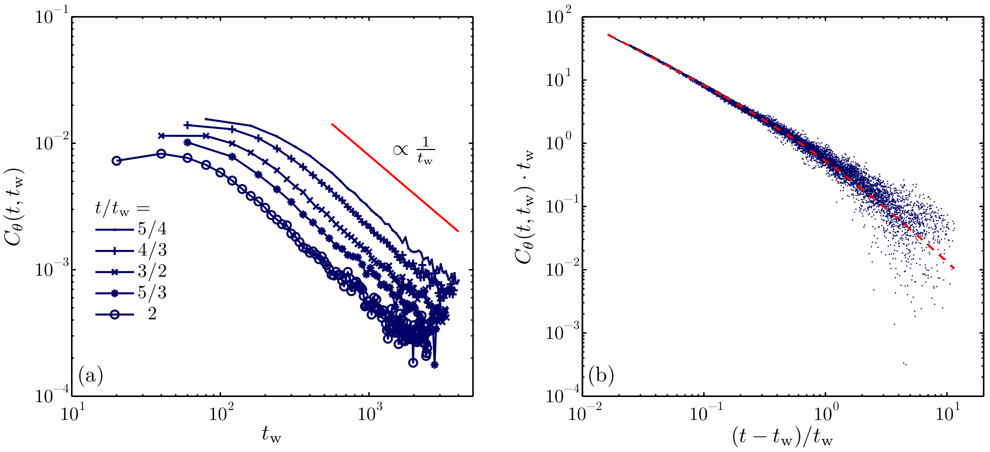

FIG. 54. Scaling of the orientation autocorrelation function. (a) $C_\theta(t, t_\mathrm{w})$ is plotted as a function of the waiting time t_w for constant ratios t/t_w. The red line is a power law $\propto t_\mathrm{w}^{-1}$. (b) The rescaled correlation function $C_\theta(t, t_\mathrm{w}) \cdot t_\mathrm{w}$ is plotted as a function of $(t - t_\mathrm{w})/t_\mathrm{w}$. The dashed red line is a fit with $f(x) = ax^{-b} \cdot (x - 1)^{-c}$, where $x \equiv t/t_\mathrm{w}$ and the parameters $a = 0.93$, $b = 0.83$, and $c = 0.98$.

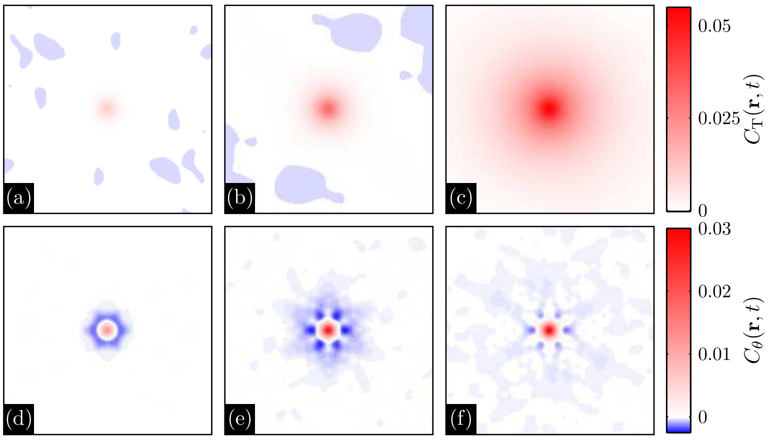

FIG. 55. Evolution of two different spatial correlation functions at $\eta = 0.005$. (a–c) The spatial translation correlation function $C_\mathrm{T}(\mathbf{r}, t)$ at times $t = 2 \cdot 10^1$, $2 \cdot 10^2$, and $2 \cdot 10^3$. (d–f) The spatial orientation correlation function $C_\theta(\mathbf{r}, t)$ at the same times. The central section sized 200×200 is shown for both correlation functions.

3. Spatial correlation functions

It is well known that a growing spatial correlation length leads to aging in the corresponding two-time correlation function [16, 171]. Therefore, to understand the origins of aging, it is important to analyse the dynamics of spatial correlations. In this section, we consider two

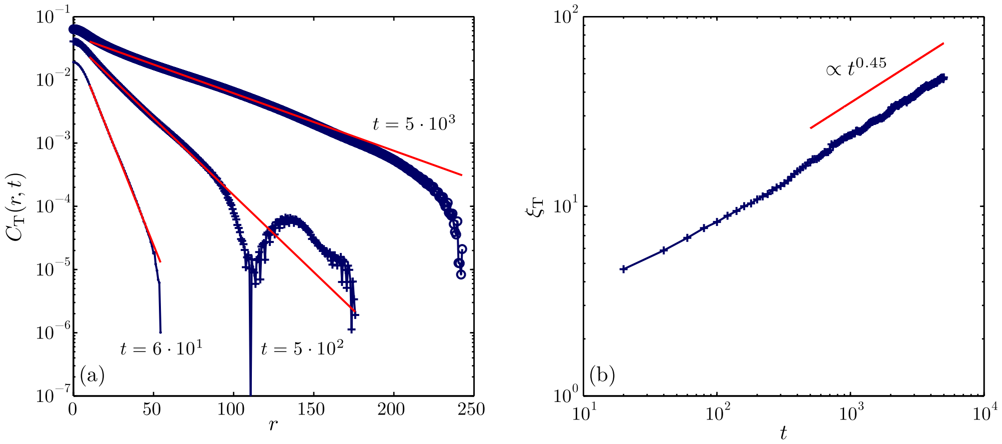

FIG. 56. Growth of the translation correlation length. (a) Spatial translation correlation function $C_{\mathrm{T}}(r,t)$ at early times. The red lines are fits with an exponential $\propto \exp(-r/\xi_{\mathrm{T}})$. (b) Translation correlation length ξ_{T} as a function of time. The red line is a power law drawn as a guide to the eye.

spatial correlation functions, namely the translation correlation function $C_{\mathrm{T}}(\mathbf{r},t)$ and the orientation correlation function $C_\theta(\mathbf{r},t)$. In Fig. 55, we present snapshots of both functions at different times $t = 2 \cdot 10^1$, $2 \cdot 10^2$, and $2 \cdot 10^3$. From a visual inspection, we conclude that $C_{\mathrm{T}}(\mathbf{r},t)$ is isotropic, i.e., it depends only on the distance $r \equiv |\mathbf{r}|$ [Fig. 55(a–c)]. There is a pronounced evolution of the translation correlation function over two decades in time, suggesting a growing correlation length. In contrast, the orientation correlation function $C_\theta(\mathbf{r},t)$, shown in Fig. 55(d–f), exhibits no signs of growing correlations, as evidenced by the constant diameter of the central peak. However, a sixfold anisotropy is visible in $C_\theta(\mathbf{r},t)$, which increases between $t = 2 \cdot 10^1$ and $t = 2 \cdot 10^2$, but has become weaker again at $t = 2 \cdot 10^3$. We note that the color scale amplifies the visual impression of the regions where $C_\theta(\mathbf{r},t)$ is negative. In the following we will treat both correlation functions as isotropic and average over their angular dependence.

The azimuthally averaged spatial translation correlation function $C_{\mathrm{T}}(r,t)$ is presented in Fig. 56(a) for times $t \leq 5 \cdot 10^3$. Within the indicated time range, it can be fitted with an exponential $\propto \exp(-r/\xi_{\mathrm{T}})$, from which the orientational correlation length ξ_{T} has been extracted. The evolution of the correlation length is shown in Fig. 56(b). For times $t \gtrsim 10^3$, ξ_{T} grows as a power law, with an exponent close to 0.45. This corresponds to a dynamic exponent [97] $z = 1/0.45 \approx 2.2$. Although we consider correlations of translation flucutations, we note that the value $z = 2$ is typical for phase-ordering phenomena with a non-conserved

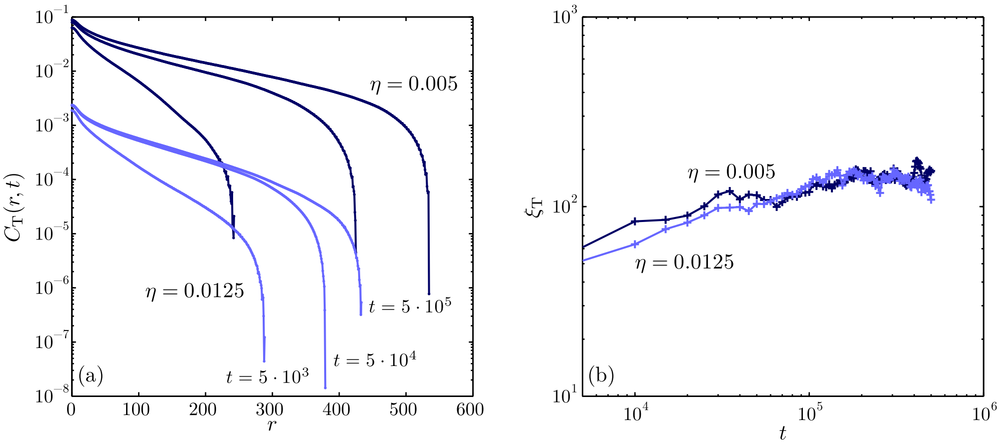

FIG. 57. (a) Spatial translation correlation function at late times. Data for noise strengths $\eta = 0.005$ and $\eta = 0.0125$ are shown, where the latter have been multiplied by a factor of 10^{-2} for clarity. (b) Translation correlation length ξ_{T} as a function of time.

order parameter [16]. While the data shown in Fig. 56 coincide with the time range in which we have observed aging (see Fig. 53), we have also computed $C_{\mathrm{T}}(r,t)$ at much later times [Fig. 57(a)]. For two noise strengths, $\eta = 0.005$ and $\eta = 0.0125$, the spatial translation correlation function exhibits a continuous relaxation. However, the correlation length ξ_{T} saturates at $\xi_{\mathrm{T}}^{\mathrm{sat}} \approx 150$ for times $t \gtrsim 10^5$, well below the size of the system, for which the smaller side $L_y = 1150$. Nevertheless, it would be desirable to check this result in even larger systems to exclude a finite-size effect. The observation of a finite correlation length $\xi_{\mathrm{T}}^{\mathrm{sat}}$ indicates that the aging of the translation correlation function $C_{\mathrm{T}}(t,t_{\mathrm{w}})$ might also become interrupted after a finite time, similar to what we have seen in the orientation autocorrelation function $C_\theta(t,t_{\mathrm{w}})$.

We conclude this section with a discussion of the spatial orientation correlation function $C_\theta(r,t)$. In Fig. 58(a), we plot $C_\theta(r,t)$ for $\eta = 0.005$ and early times $t \leq 5 \cdot 10^3$. The correlation function shows an evolution between $t = 6 \cdot 10^1$ and $t = 5 \cdot 10^2$, but almost none between the latter time and $t = 5 \cdot 10^3$. This corresponds to the behavior of the two-time correlation function $C_\theta(t,t_{\mathrm{w}})$ reported in Fig. 52. As expected, no further evolution is detected when even longer time scales are considered, independent of the noise strength [Fig. 58(b)]. The absence of a growing length scale indicates that the aging of the orientation correlation function $C_\theta(t,t_{\mathrm{w}})$ we reported before cannot be caused by a critical dynamics, where the correlation length diverges [97]. Another mechanism, based on a rough energy

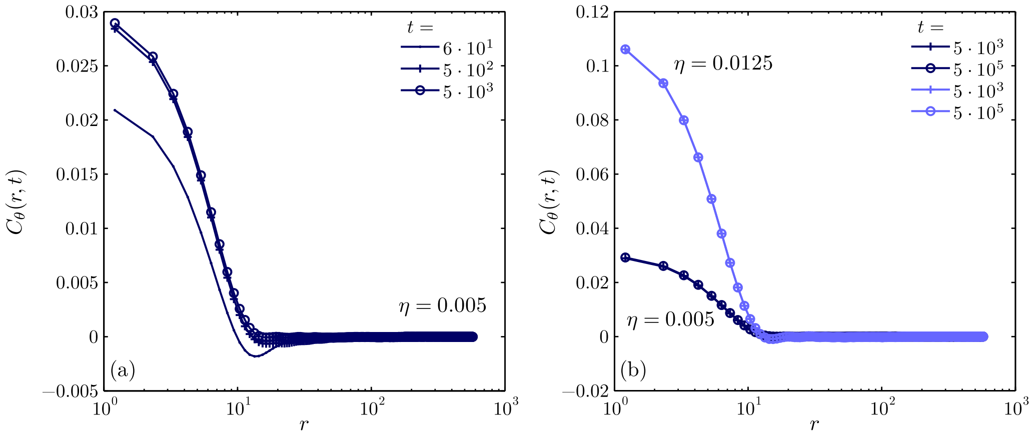

FIG. 58. The spatial orientation correlation function $C_\theta(r,t)$ at (a) early and (b) late times. In (b), data for noise strengths $\eta = 0.005$ and $\eta = 0.0125$ are shown. Here, no further evolution is discernible over two decades in time.

landscape will be tested and subsequently discarded in Sec. VII D. Therefore, we regard the aging effects in $C_\theta(t,t_{\mathrm{w}})$ as a transient phenomenon without implications for the equilibrium state of the hexagon-forming system, which exhibits long-range orientational order.

In this section, we have computed spatio-temporal correlation functions of both, translation and orientation fluctuations in the hexagon-forming system. The translation autocorrelation function exhibits aging, with a scaling form typical for domain growth, $C_{\mathrm{T}}(t,t_{\mathrm{w}}) \sim f_{\mathrm{T}}(t/t_{)}w$. The aging effects we observed could be linked to the presence of a growing spatial correlation length, ξ_{T}. However, this length scale was found to saturate after a long but finite time. In contrast, the dynamics of the orientation autocorrelation function $C_\theta(t,t_{\mathrm{w}})$ is interrupted after a short time, as the orientational correlation length ξ_θ remains on the order of one domain spacing. While there clearly is orientational order present in the hexagon-forming system, with the corresponding order parameter remaining constant over several decades in time, the results are less clear concerning translational order (Fig. 51). However, taking into account the saturation of the translational correlation length, we expect that the hexagon-forming system also has long-range translational order at finite noise strengths $\eta < \eta_{\mathrm{c}}$.

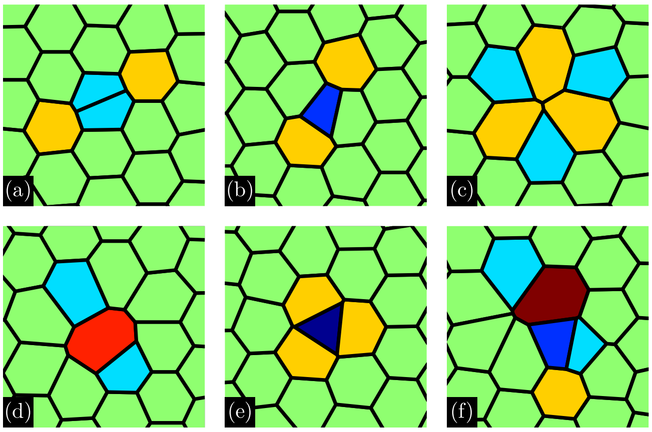

FIG. 59. Typical defects appearing in the ordered hexagonal phase at $\eta = 0.0125$. (a) A dislocation pair consisting of two ⑦- and two ⑤-defects (⑦-⑤-⑤-⑦-defect). (b) ⑦-④-⑦ defect. (c) Three dislocations in a flower-like configuration. (d) ⑤-⑧-⑤-defect. (e) Three ⑦-defects encircling one ③-defect. Note that there is a short edge extending from each vertex of the central triangle. (f) A more complex defect involving two ⑤-defects and one ⑨-, ⑦- and ④-defect each.

C. Topological defects

We now turn to the dynamics of topological defects in the hexagon-forming system, which we have neglected so far. Defects have been identified using the Voronoi construction, as described before (see Sec. VII A 2). At the lower noise strength, $\eta = 0.005$, the hexagon-forming system remains free of topological defects at all times. Examples of defects encountered at the higher noise strength $\eta = 0.0125$ are shown in Fig. 59, where they are represented by the corresponding Voronoi cell. The different colors correspond to the number of edges of the respective cell. In the following, we will use the term "defect configuration" to refer to a connected set of circular domains, as represented by their Voronoi cells, with a number of nearest neighbors other than six. One such defect configuration is shown in Fig. 59(a), consisting of two sites with seven neighbors, connect by two sites with five neighbors. Thus, we will name this defect configuration a ⑦-⑤-⑤-⑦-defect. We also note that this type of defect corresponds to a bound pair of elementary dislocations [185, 207].

We begin our analysis with an observation about the defect configurations we encounter. As before, let N_i denote the number of sites with i neighbors. N_i vanishes for $i < 3$, as there exist no corresponding polygons with less than three edges. We find that following relation

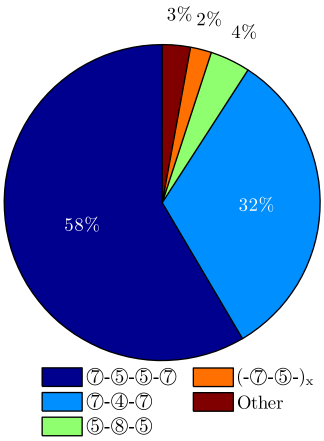

FIG. 60. Relative frequency of defect configurations for $\eta = 0.0125$. The chart is based on a total number of $24,073$ defects which have been identified in systems where $10^5 \leq t \leq 5 \cdot 10^5$.

holds for all connected defect configurations observed in the ordered hexagon-forming system:

$$\sum_i i \cdot (N_{6-i} - N_{6+i}) = 0. \tag{29}$$

Consequently, it also holds globally, when the N_i are replaced by the corresponding defect densities ρ^i_{NN}. However, the fact that Eq. (29) is fulfilled *individually* by each defect configuration leads us to interpret those defects as only a local perturbation of the ordered hexagonal phase. Such a pertubation could be caused by, e.g., the merging or splitting of neighboring circular domains (see Fig. 49). This might explain our observation that the hexagon-forming system behaves qualitatively the same, whether defects are present or not (cf. our comparison of different noise strengths in the preceding section). Eq. (29) would no longer be valid if, e.g., dislocations were to dissociate, as predicted for the hexatic-isotropic transition [185, 207]. A relation similar to Eq. (29) has been reported for vacancies induced in an ordered colloidal crystal [219, 220], which also constitute a local perturbation of the hexagonal lattice.

In Fig. 60, we have compiled a chart visualizing the relative frequencies of different defect configurations at late times. The most common defects are ⑦-⑤-⑤-⑦-defects, representing a bound pair of dislocations. The second most common defects are ⑦-④-⑦-defects, which can be interpreted as a "squeezed" dislocation pair, where two sites with five neighbors each have been replaced by one site with four nearest neighbors [see Fig. 59(b)]. Other types of defects account for less than 10% of the total number of defects.

The defect densities as a function of time are shown in Fig. 61, where the term ⓝ-defect

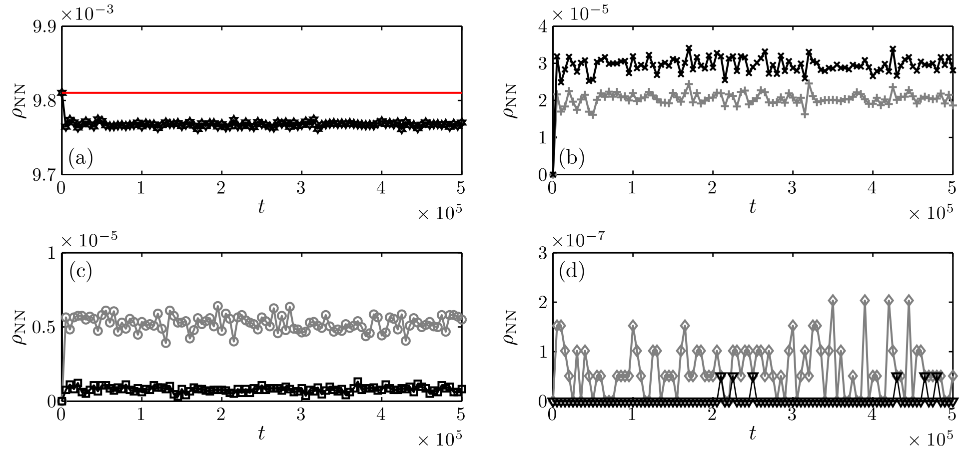

FIG. 61. Defect densities ρ_{NN} as a function of time for $\eta = 0.0125$. (a) Density of sites having six nearest neighbors. The red line marks the initial value. (b) ρ_{NN} for ⑤- and ⑦-defects (gray + and black ×). (c) ρ_{NN} for ④- and ⑧-defects (gray ○ and black □). (d) ρ_{NN} for ③- and ⑨-defects (gray ◇ and black ▽).

refers to sites with n nearest neighbors. Regardless of the type of defect, the corresponding densities are approximately constant at late times t, apart from small fluctuations. We conclude that there is no slow dynamics associated with topological defects present in the ordered hexagon-forming system. Most of the defects are pairs of dislocations (see Fig. 59), as expected for the low-temperature phase of a 2D crystal [185]. However, the behavior of the translation correlation functions, as discussed in Sec. VII B 3, does not match the latter phase. The absence of free dislocations (⑦–⑤-defects) rules out a hexatic phase, as predicted by KTHNY theory [207] for intermediate temperatures. Furthermore, the properties of the system do not change qualitatively upon the appearance of defects, which we have shown by comparing data for $\eta = 0.005$ and for $\eta = 0.0125$ in the previous section.

D. Quenches to $\eta = 0$

In the following, we present results from quenches to $\eta = 0$, where the noise is switched off in a system which had previously evolved at a noise strength $\eta > 0$ for a time t_{w}. After the noise strength is set to $\eta = 0$, the system performs a deterministic descent within the energy landscape given by Eq. (22) [65]. Investigating this dynamics might provide insights into the

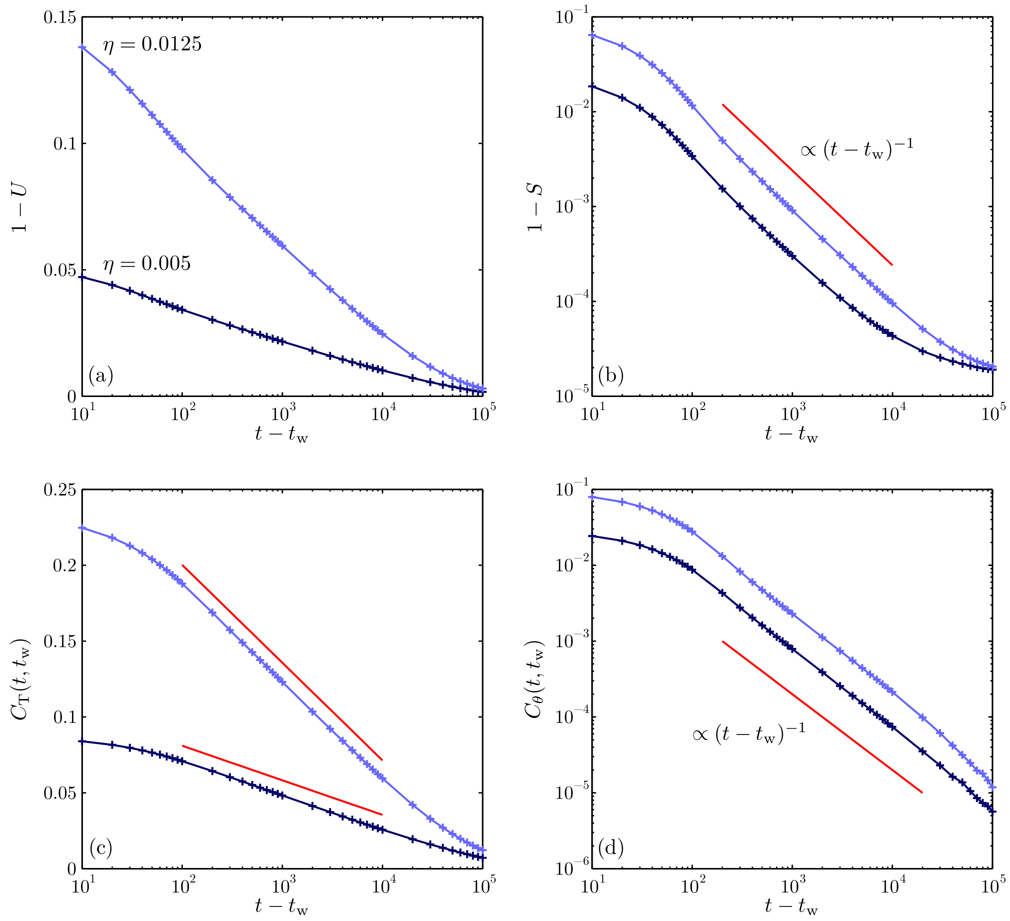

FIG. 62. (a) The translational order parameter U and (b) the orientational order parameter S plotted as a function of the time $t - t_\mathrm{w}$ after a quench to $\eta = 0$, with $t_\mathrm{w} = 5 \cdot 10^5$. (c) The translation correlation function $C_\mathrm{T}(t, t_\mathrm{w})$ and (d) the orientation correlation function $C_\theta(t, t_\mathrm{w})$ are also shown as a function of $t - t_\mathrm{w}$. The red lines in (c) correspond to functions $f(\tau) = a - b\log(\tau)$, where $\tau \equiv t - t_\mathrm{w}$. Note that the data are plotted on a lin-log scale in (a) and (c), while a log-log plot is shown in (b) and (d).

mechanisms of ordering and disordering in the hexagon-forming system. The existence of a huge number of metastable states within the free energy landscape is commonly accepted as one reason for glassy dynamics and aging [10]. Furthermore, a free energy functional similar to Eq. (22) was shown to exhibit a glass transition due to the proliferation of metastable states [115, 117]. The question of interest is therefore whether the system gets stuck in a local minimum upon being quenched to $\eta = 0$.

In Fig. 62, we present the temporal evolution of the two order parameters S and U and of the corresponding correlation functions after a quench at $t_{=}5 \cdot 10^5$. In all cases, a slow dynamics is observed, and no stationary state is reached even at the latest times we consider. However, there are differences in the way the quantities we consider evolve as the system approaches the perfectly ordered state. For the two initial noise strengths, both the translational order parameter, plotted here as $1 - U$, as well as the translation correlation function $C_{\mathrm{T}}(t, t_{\mathrm{w}})$ exhibit a logarithmic decrease over at least two decades as a function of the time $t - t_{\mathrm{w}}$ after the quench [Fig. 62(a, c)]. In contrast, the orientational order parameter (plotted as $1 - S$) and the correlation function $C_{\theta}(t, t_{\mathrm{w}})$ decay as power laws $\propto (t - t_{\mathrm{w}})^{-1}$ [Fig. 62(b, d)]. Thus, we have shown that the hexagon-forming system exhibits a slow dynamics not only when evolving from a perfectly ordered state at a finite noise strength, but also when approaching the ordered state after a quench to $\eta = 0$. The absence of an arrest of the dynamics reveals that the slow relaxation and the aging effects discussed before are not caused by a complex free energy landscape. Similar to the case of the stripe-forming system (see Sec. III C), the slow dynamics after a quench to $\eta = 0$ is most likely a consequence of the continuous symmetries (translational and orientational) present in the hexagonal pattern.

E. Evolution from a homogeneous initial state

In contrast to the ordered inital conditions used in the preceding section, most simulation studies in the literature have focused on hexagon-forming systems quenched from a homogeneous (disordered) initial state [165, 184, 221–224]. This situation has also been addressed in experimental works [211, 225–228]. Similar to the case of the stripe-forming system, microphase separation takes place during the early times after the quench, driven by a linear instability [229, 230]. In the present case, circular domains of the minority component are formed, which exhibit short-range hexagonal order. Subsequently, domain growth sets in, with domains now consisting of hexagons with uniform orientation. These domains are separated by grain boundaries built from dislocations, and possibly interspersed with point-like topological defects, such as disclinations (see Fig. 63). Various length scales describing the pattern have been reported to grow as power laws of time, analogous to macrophase-separating systems [16]. Our motivation to study this process is twofold: First, we are interested in the aging phenomena associated with domain growth in the hexagon-forming system. Although aging in this case is expected due to the presence of a growing

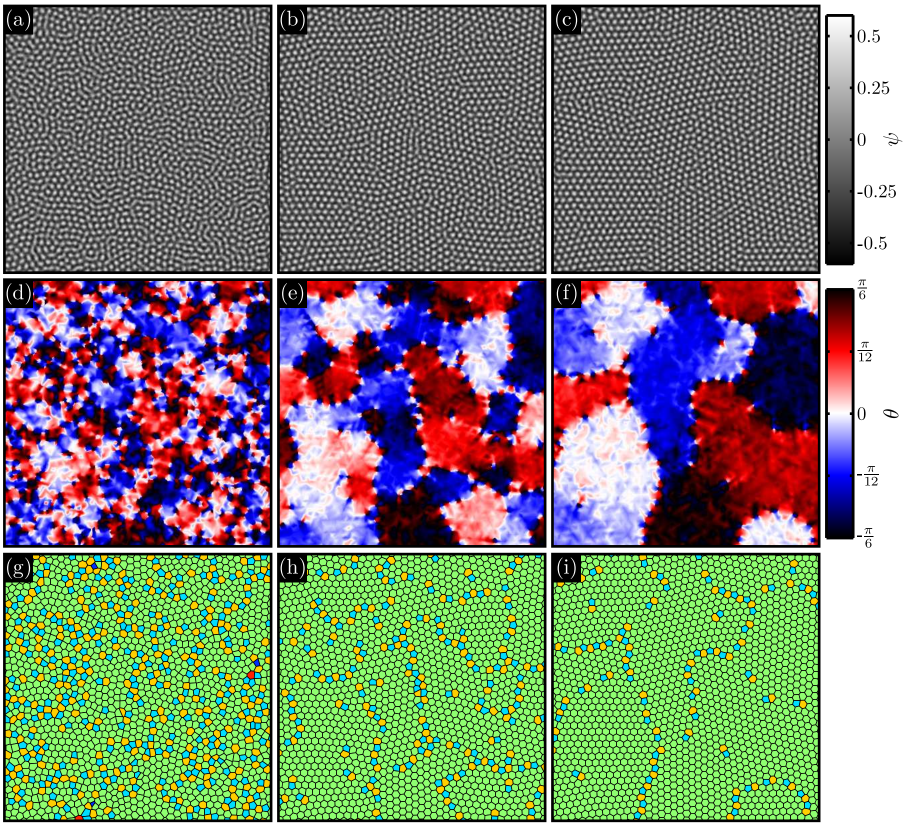

FIG. 63. Snapshots of the domain growth process in the 2D hexagon-forming system. (a–c) Concentration fields $\psi(\mathbf{r}, t)$. (d–f) Corresponding orientation fields $\theta(\mathbf{r}, t)$. (g–i) Voronoi diagrams showing topological defects. The cells are colored as in Fig. 59. Sections sized 400×400 taken from a larger system with $L = 1536$ are shown. The time $t = 2 \cdot 10^2$, $2 \cdot 10^3$, and $2 \cdot 10^4$ (left to right).

length scale [15, 16, 171], two-time quantities, such as the orientation autocorrelation function, have not been studied in this scenario before. Second, the data for the more familiar case of homogeneous initial conditions can serve as a benchmark for our analysis by comparing them to results from the literature.

Simulations with homogeneous initial conditions were performed on a square lattice with $L_x = L_y = 1536$ and periodic boundary conditions. The noise strength $\eta = 0.005$, and all other parameters were the same as in the case of ordered initial conditions. From the resulting data $\psi(\mathbf{r}, t)$, the local orientation $\theta(\mathbf{r}, t)$ has been extracted as described before (see Sec. VII A 2). From the orientation field, the autocorrelation function $C_\theta(t, t_\mathrm{w})$ as well as the spatial correlation function $C_\theta(\mathbf{r}, t)$ can be computed. The orientational correlation length ξ_θ is defined as the distance r for which the azimuthally averaged spatial orientation correlation function $C_\theta(r,t)$ first falls below a threshold α. Additionally, we have also computed the number of nearest neighbors of each circular domain by counting the edges of the associated Voronoi cell [213]. While a site on a regular hexagonal lattice has six nearest neighbors, a deviation from this number indicates a topological defect. The defect density ρ^i_{NN} is given by the count N_i of sites with i nearest neighbors divided by the system size $L_x \times L_y$.

Fig. 64(a) shows the orientational correlation length ξ_θ for three different values of the threshold α. After an initial regime at times $t \lesssim 2000$, ξ_θ grows as a power law, independent of the threshold. Least-squares fits to the data yield an exponent ≈ 0.30. There is no consensus yet in the literature about the value of this growth exponent. In the absence of noise ($\eta = 0$), Yokojima and Shiwa reported a value of 0.2 [223], while Vega *et al.* found a larger value of 0.25 at a finite noise strength $\eta > 0$ [184]. For related models, a continuous dependence of the exponent on the noise strength was reported [224, 231]. However, even a logarithmic growth of the correlation length has been observed in a certain parameter regime [232, 233]. We also note that different measures for the correlation length yield different exponents [184, 224], similar to the case of the stripe-forming system (see Sec. V). In Fig. 64(b), we plot the defect density ρ_{NN} for sites with four, five, seven and eight nearest neighbors, respectively. The densities of ⑤- and ⑦-defects as well as those for ④- and ⑧-defects are virtually identical. It has been pointed out before that most ⑤- and ⑦-defects are located on neighboring sites, thus forming dislocations, which in turn are part of grain boundaries [184]. This scenario is also observed in our simulations, as shown in Fig. 63(g–i). Isolated ⑤- or ⑦-defects, which can be classified as disclinations, are much more rare. Therefore, we do not count dislocations and disclinations separately, but only present the defect densities with respect to the number of nearest neighbors. ρ_{NN} for ⑤- and ⑦-defects decreases monotonically with time. There is again an initial stage for $t \lesssim 2000$, followed by power-law behavior with an exponent ≈ -0.27. In contrast, the density of ④- and ⑧-defects is about one order of magnitude smaller at the earliest times and decreases quickly for $t \lesssim 2000$, roughly as t^{-2}. Only a very small density remains at later times. While other types of defects exist in the disordered state shortly after the quench, their number becomes negligible even earlier (data not shown).

We now turn to the behavior of the orientation autocorrelation function $C_\theta(t, t_{\mathrm{w}})$. In Fig. 64(c), $C_\theta(t, t_{\mathrm{w}})$ is plotted as a function of the waiting time t_{w} for constant ratios t/t_{w}. For $t \gtrsim 2000$, there is very little variation, which is an indication that the scaling form $C(t, t_{\mathrm{w}}) \sim f(t/t_{\mathrm{w}})$

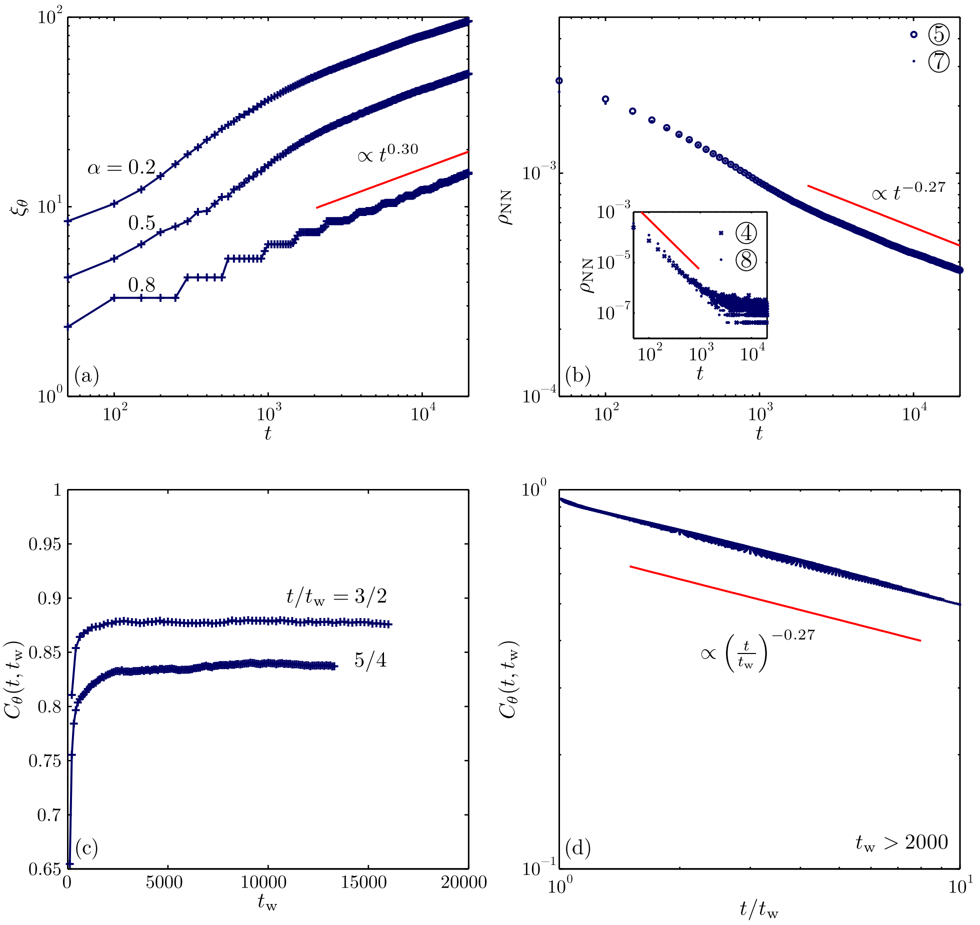

FIG. 64. Domain growth in the 2D hexagon-forming system evolving from a homogeneous initial state: (a) Orientational correlation length ξ_θ as a function of time for different values of the threshold α. The red line represents a power law with the exponent 0.30. (b) Defect density ρ_{NN} for ⑤- and ⑦-defects ($+$ and $\circ$). The straight red line is a power law with the indicated exponent. The inset shows ρ_{NN} for ④- and ⑧-defects ($\times$ and $\bullet$) together with a power law $\propto t^{-2}$. (d) The orientation correlation function $C_\theta(t, t_\mathrm{w})$ as a function of t_w for ratios $t/t_\mathrm{w} = \frac{3}{2}$ and $\frac{5}{4}$. (d) $C_\theta(t, t_\mathrm{w})$ as a function of t/t_w for waiting times $t_\mathrm{w} > 2000$. The red line is a power law drawn as aguide to the eye.

holds. We confirm this by plotting $C(t, t_\mathrm{w})$ as a function of t/t_w, discarding waiting times $t_\mathrm{w} < 2000$. This results in a collapse of the data onto a single curve over the whole range of t/t_w. The scaling function $f(t/t_\mathrm{w})$ is well described by a power law with the exponent 0.27, comparable to the exponents describing the coarsening of the correlation length ξ_θ and the defect density. We point out that these values closely match the respective exponents found for the stripe-forming system evolving from a homogeneous initial state (see Sec. V).

This concludes our study of the coarsening process after a quench from homogeneous initial conditions. In agreement with earlier studies, we find that the dynamics is dominated by the annihilation of grain boundaries, not by the interaction of point defects [184, 211]. A comparable polycrystalline structure has also been observed, e.g., in freezing experiments on 2D colloidal systems [228, 234]. The orientation autocorrelation function exhibits aging, with a scaling form typical for domain growth [16, 97].

F. Conclusion

To summarize, we have performed simulations of a 2D hexagon-forming system, focusing on the relaxation from an ordered state in the presence of noise. Below a critical noise strength η_{c}, the evolution of the translation correlation functions takes place on a long but finite time scale. Aging is observed in the two-time correlation function $C_{\mathrm{T}}(t, t_{\mathrm{w}})$, which fulfills a scaling relation typical for phase-ordering below the critical temperature [16, 97]. The corresponding spatial correlation length ξ_{T} grows until it reaches a value of about 15 domain spacings. In contrast, the spatial orientation correlations remain short-range, with a correlation length ξ_{θ} similar to the distance between the circular domains forming the hexagonal pattern.

A slow relaxation is also observed when quenching hexagon-forming systems from finite noise strengths to $\eta = 0$. The translation autocorrelation function relaxes logarithmically, while the orientation correlation function decays as a power law. We have also performed simulations with homogeneous initial conditions. Earlier results for the growing orientational correlation length ξ_{θ} and the decreasing density of topological defects ρ_{NN} could be reproduced. The two-time orientation autocorrelation function exhibits aging, with a scaling form is that expected for domain growth [16, 97].

The hexagonal pattern evolving from an ordered state as investigated in this work is related to the much-studied phenomenon of two-dimensional melting, for which a two-stage transition scenario has been predicted [206, 207]. Our results seem at first glance to be compatible with the so-called 2D crystal phase [185, 209] at low temperatures, where topological defects occur only in small numbers and are tightly bound, thus forming dislocation pairs (see Fig. 59). However, while orientational symmetry is broken in this phase, consistent with our results, the theory predicts quasi–long-range translational order and criticality for a range of temperatures $0 < T < T_\mathrm{m}$ [185]. This is at odds with the behavior of the translation correlation function we observe in the model system, where the spatial correlation length grows in time, but saturates at a finite value. Furthermore, the scaling form of the translation autocorrelation function, $C_\mathrm{T}(t, t_\mathrm{w}) \sim f(t/t_\mathrm{w})$, is indicative of a simple coarsening process, and not of a critical dynamics. Therefore, the hexagon-forming system we studied cannot be classified as a 2D crystal. While we have found no evidence for the existence of the hexatic phase [206, 207], our results leave a small window of noise strengths $0.0125 < \eta < \eta_\mathrm{c} \approx 0.02$ where it could possibly occur. Yet, we have seen in the stripe-forming system that dislocations remain bound in pairs until the system becomes isotropic at the critical noise strength η_c. Although the symmetries are different, we expect a similar scenario in the hexagon-forming system, and thus a single-stage transition without an intermediate phase.

It is unclear what the origin is of the aforementioned discrepancies with theory, considering that the model we studied is one of the simplest which allows for the formation of hexagonal patterns. If the observed differences turn out to be an inherent property of the coarse-grained model we studied, it remains to be seen what ingredients are missing to reproduce the 2D melting scenario.

Appendices

Appendix A: Simulation algorithm

In this work, we have performed computer simulations of Eq. (3) on a square lattice with size $L_\perp \times L_\parallel$, using a semi-implicit pseudo-spectral algorithm adapted from Ref. 73. Time and space are discretized in steps of Δt and Δx, respectively. In order to simulate an equation such as Eq. (3), the various differential operators must be suitably approximated. The pseudo-spectral method described below achieves this by performing all spatial derivatives in Fourier space and integrating the time derivative using a backwards-differences scheme. First, Eq. (3) is Fourier-transformed (denoted by $\widehat{\cdot}$), which renders it an ordinary differential equation (ODE) in time instead of a partial differential equation (PDE) in both time and space:

$$\frac{\partial}{\partial t}\widehat{\psi}(\mathbf{k},t) = \underbrace{\left(k^2 - k^4 - \Gamma\right)}_{d_0}\widehat{\psi}(\mathbf{k},t) - k^2\widehat{\psi}(\mathbf{k},t)^3 + \widehat{\zeta}(\mathbf{k},t) \tag{A1}$$

The task now consists of solving the initial-value problem

$$y'(t) = f(y,t), \text{ with } y(t=0) = y_0. \tag{A2}$$

To this end, the time derivative on the left-hand side is discretized using a backwards-differences (BDF) scheme. The formulas up to order $m=3$ are as follows [235]:

$$\begin{aligned} m=1: &\quad y_{n+1} - y_n = \Delta t f_{n+1}, \\ m=2: &\quad \frac{3}{2}y_{n+1} - 2y_n + \frac{1}{2}y_{n-1} = \Delta t f_{n+1}, \\ m=3: &\quad \frac{11}{6}y_{n+1} - 3y_n + \frac{3}{2}y_{n-1} - \frac{1}{3}y_{n-2} = \Delta t f_{n+1}. \end{aligned} \tag{A3}$$

Furthermore, the terms linear in ψ on the right-hand side of Eq. (A2) are treated implicitly (i.e., assigned the time step $n+1$) in order to improve stability [73], while the nonlinear term is treated explicitly using an Adams-Bashforth scheme. At the mth order, this corresponds to interpolating the value f_{n+1} with a polynomial of degree $m-1$ using the previously computed values $f_{n-m+1}, \dots, f_n$. The interpolated values are given by

$$\begin{aligned} m=1: &\quad f_{n+1} \approx f_n, \\ m=2: &\quad f_{n+1} \approx -f_{n-1} + 2f_n, \\ m=3: &\quad f_{n+1} \approx f_{n-2} - 3f_{n-1} + 3f_n. \end{aligned} \tag{A4}$$

Applying this procedure to Eq. (A1), we arrive at the following formulas, where we have dropped the dependence of ψ and ζ on the discretized wave vectors $\mathbf{k}_i$:

$$m=1\colon\ \widehat{\psi}_{n+1} = \frac{1}{1-\Delta t\cdot d_0}\left[\widehat{\psi}_n - \Delta t\cdot k^2\widehat{\psi^3}_n + \widehat{\zeta}_{n+1}\right], \tag{A5}$$

$$m=2\colon\ \widehat{\psi}_{n+1} = \frac{1}{\frac{3}{2}-\Delta t\cdot d_0}\left[2\widehat{\psi}_n - \frac{1}{2}\widehat{\psi}_{n-1} - \Delta t\cdot k^2\left(-\widehat{\psi^3}_{n-1} + 2\widehat{\psi^3}_n\right) + \widehat{\zeta}_{n+1}\right], \tag{A6}$$

$$\begin{aligned} m=3\colon\ \widehat{\psi}_{n+1} = & \frac{1}{\frac{11}{6}-\Delta t\cdot d_0}\left[3\widehat{\psi}_n - \frac{3}{2}\widehat{\psi}_{n-1} + \frac{1}{3}\widehat{\psi}_{n-2}\right.\\ & \left. - \Delta t\cdot k^2\left(\widehat{\psi^3}_{n-2} - 3\widehat{\psi^3}_{n-1} + 3\widehat{\psi^3}_n\right) + \widehat{\zeta}_{n+1}\right]. \end{aligned} \tag{A7}$$

The term $\widehat{\zeta}_{n+1}(\mathbf{k}_i)$ is the Fourier transform of a field of random numbers $\zeta_{n+1}(\mathbf{r}_i)$ drawn from a Gaussian distribution with zero mean and correlations

$$\langle\zeta_n(\mathbf{r}_i)\zeta_m(\mathbf{r}_j)\rangle = -2\eta\Delta t\delta_{n,m}\nabla^2\delta(\mathbf{r}_i-\mathbf{r}_j), \tag{A8}$$

where the operator ∇^2 is approximated using finite differences [161, 236].
One step of the complete algorithm consists of evaluating the nonlinear term ψ_n^3 in real space, Fourier-transforming it, computing $\widehat{\psi}_{n+1}$, and transforming back the latter in order to obtain ψ_{n+1}. The first-order algorithm given by Eq. (A5) has been used before to simulate stripe-forming systems [74, 75]. In this work, we have used the third-order algorithm, Eq. (A7), with the lower-order formulas providing the necessary initial values for $\widehat{\psi^3}_{n-1}$ and $\widehat{\psi^3}_{n-2}$, respectively.

Appendix B: Comparison of algorithms

In order to check the validity of our numerical procedure as decribed in Appendix A, we have performed a comparison of different algorithms for simulating the evolution of $\psi(\mathbf{r},t)$ given by Eq. (3). While variants of pseudo-spectral algorithms have been used to simulate modulated phases in the past [49, 74, 75, 77, 237], the most simple method for numerically solving a partial differential equation such as Eq. (3) consists of an Euler scheme for the time integration combined with a finite-differences approximation $\mathcal{L}$ of the Laplacian [38, 236, 238]. The cell dynamics technique [66, 69, 165] also follows this approach. We have chosen two algorithms based on finite differences for our comparison. They are characterized by different approximations of the Laplacian, namely the stencil used in Ref. 38 (see also Ref. 239):

$$\mathcal{L}_{3\times 3} \equiv \frac{1}{6\Delta x^2} \begin{bmatrix} 1 & 4 & 1 \\ 4 & -20 & 4 \\ 1 & 4 & 1 \end{bmatrix} , \tag{B1}$$

and the nine-point axial stencil [240], whose merits have been discussed before [241]:

$$\mathcal{L}_{9\mathrm{PA}} \equiv \frac{1}{12\Delta x^2} \begin{bmatrix} 0 & 0 & -1 & 0 & 0 \\ 0 & 0 & 16 & 0 & 0 \\ -1 & 16 & -60 & 16 & -1 \\ 0 & 0 & 16 & 0 & 0 \\ 0 & 0 & -1 & 0 & 0 \end{bmatrix} . \tag{B2}$$

We have taken a qualitative approach to assessing the performance of the different algorithms, consisting of simulations with ordered initial conditions, as described before, and subsequent comparison of the orientation correlation functions, which are computed from the simulation data. The noise strength $\eta/\eta_c = \frac{1}{30}$ and the lattice constant $\Delta x \equiv 1$ in all cases. From the simulation results $\psi(\mathbf{r}, t)$ we have computed the orientation autocorrelation function $C_\theta(t, t_\mathrm{w})$, averaged over ten independent realizations. At the bottom of Fig. 65, the result for $\mathcal{L}_{9\mathrm{PA}}$ and a time step $\Delta t = 0.005$ is shown. This rather small value of Δt is dictated by the stability requirements of the operator $\mathcal{L}_{9\mathrm{PA}}$ [238, 241]. The results from the pseudo-spectral algorithm [Eq. (A7)], are also shown. Note that the latter have been averaged over 40 independent realizations. There is excellent agreement between the two curves. At the top of Fig. 65, we plot $C_\theta(t, t_\mathrm{w})$ resulting from simulations using $\mathcal{L}_{3\times 3}$ in conjunction with an Euler scheme with $\Delta t = 0.05$ and 0.005, respectively. The data exhibit a peculiar behavior, with increasing correlations at late times, in stark difference to the curves discussed before. Also, the shift in magnitude with respect to the other curves is considerable, suggesting that the stripe system is in a state with less orientational order. Decreasing the time step Δt by a factor of ten does not change the overall behavior of $C_\theta(t, t_\mathrm{w})$.

These results give us confidence in the validity of our simulations, as there is very good agreement between the results from the pseudo-spectral algorithm and the finite-differences approach based on the operator $\mathcal{L}_{9\mathrm{PA}}$. The use of an alternative stencil, $\mathcal{L}_{3\times 3}$, results in a drastically different behavior of the orientation autocorrelation function, which we regard as spurious. On the other hand, the choice of the time integration scheme seems less crucial

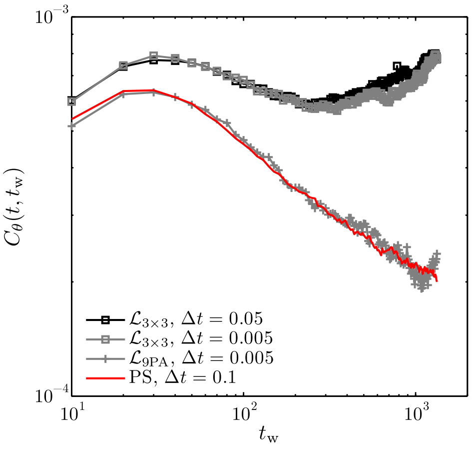

FIG. 65. Effect of different simulation algorithms for $\psi(\mathbf{r}, t)$ on the orientation autocorrelation function $C_\theta(t, t_\mathrm{w})$. Different time steps Δt and approximations to the Laplacian $\mathcal{L}$ have been used as indicated. PS denotes the pseudo-spectral algorithm given by Eq. (A7).

than that of the spatial differential operator. Finally, the efficiency of the pseudo-spectral algorithm is demonstrated, which allows for a far larger time step Δt compared to $\mathcal{L}_{9\mathrm{PA}}$.

Appendix C: Structure factor of the orientation

In this Appendix, we will briefly address two additional topics involving the structure factor of the orientation $S_\theta(\mathbf{k}, t)$, which we have discussed extensively in Sec. IV. First, we investigate the influence of the noise strength η on cuts through the two-dimensional structure factor, given by $S_\theta(k_\perp = 0, k_\parallel, t)$. We will use the same data as presented in Sec. III, corresponding to four different values of η ranging from $\eta/\eta_\mathrm{c} = \frac{1}{150}$ to $\eta/\eta_\mathrm{c} = \frac{2}{3}$. The results are shown in Fig. 66, where the dominant wave length λ^* and the peak intensity S_θ^* are plotted as a function of time. Both quantities grow as power laws of time, with exponents that are independent of the noise strength. The dominant wave length increases with time as $\lambda^* \sim t^{0.25}$, and curves for different noise strengths fall on top of each other. For the highest noise strength, $\eta/\eta_\mathrm{c} = \frac{2}{3}$, fluctuations of the structure factor cause deviations from power-law behavior at the latest times [Fig. 66(a)]. At early times $t \lesssim 10^4$, the peak intensity grows with time as $S_\theta^* \sim t^{0.5}$ [Fig. 66(b)]. This exponent is also independent of the noise strength η, although fluctuations become stronger at higher values of η. In contrast, the magnitude of S_θ^* increases with increasing η. At early times, S_θ^* is roughly proportional to η. At late times,

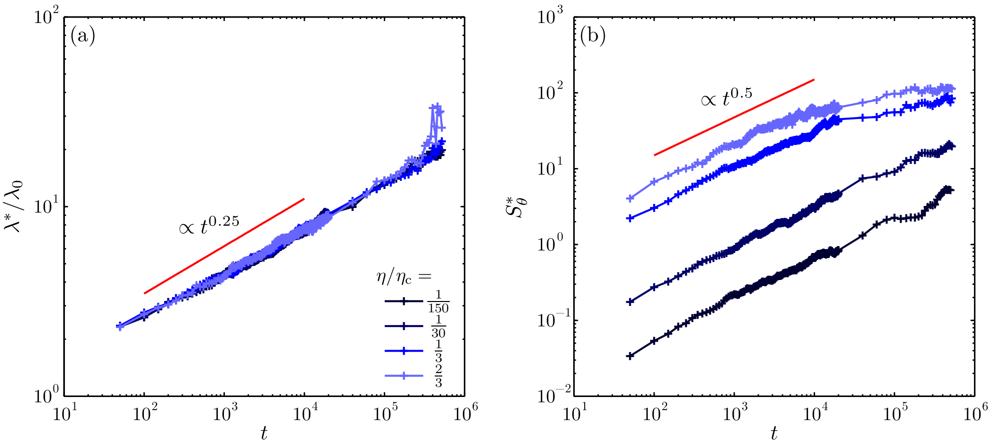

FIG. 66. Evolution of the structure factor at different noise strengths η/η_c. (a) Growth of the dominant wave length λ^*. (b) Peak intensity S^*_θ as a function of time. The straight red lines are power laws with the indicated exponents.

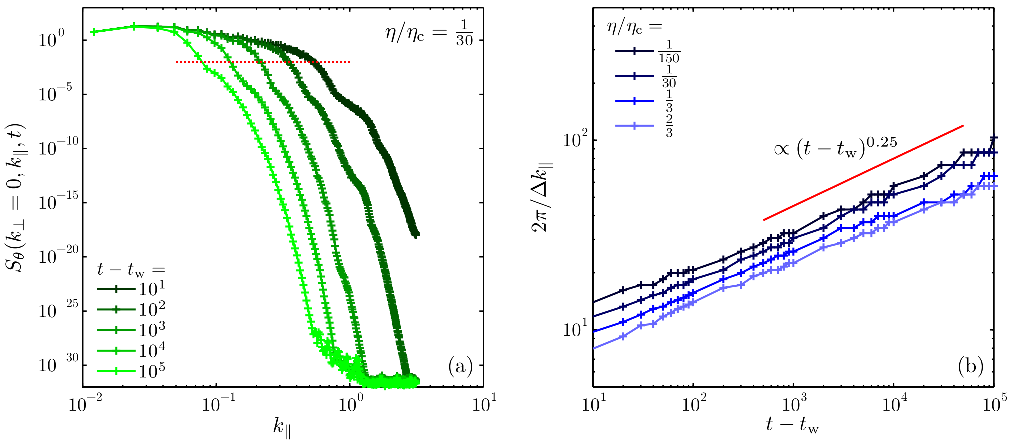

FIG. 67. Evolution of the structure factor parallel to the stripes after a quench to $\eta = 0$. (a) $S_\theta(k_\perp = 0, k_\parallel, t)$ at different times $t - t_w$ after the quench. The dashed red line represents a threshold at $S_\theta(k_\parallel) = 10^{-3}$, which is used to define the width $\Delta k_\parallel$. (b) Growth of the length scale $2\pi/\Delta k_\parallel$ as a function of $t - t_w$. The red line represents a power law with the exponent 0.25.

there seems to be a cross-over to saturation, especially for the two highest noise strengths. The results shown so far indicate that the growth exponents for the characteristic quantities λ^* and S^*_θ describing the structure factor do not depend on the noise strength.

We now turn to the relaxation of the structure factor after a quench to $\eta = 0$ (see Sec. III C), again focusing on the behavior of cuts $S_\theta(k_\perp = 0, k_\parallel, t)$ parallel to the stripes. As we have seen before (cf. Sec. IV), at finite noise strength $S_\theta(k_\perp = 0, k_\parallel, t)$ is characterized by a peak at $k_\parallel = k_\parallel^*$, which shifts to smaller wave numbers as time progresses, and a static part at large $k_\parallel$. The situation is reversed after quenching the system to $\eta = 0$. As seen in Fig. 67(a), the region around the peak remains virtually unchanged over four decades in the time $t - t_\mathrm{w}$ after the quench, indicating that large-scale structures in the orientation field decay very slowly. In contrast, the structure factor decreases sharply at higher wave numbers, with the location of the drop shifting to smaller values of $k_\parallel$ as $t - t_\mathrm{w}$ increases. This process can be quantified by introducing the width $\Delta k_\parallel$, which we define as the value of $k_\parallel$ for which $S_\theta(k_\perp = 0, k_\parallel, t)$ first falls below 10^{-3} [see the dashed red line in Fig. 67(a)]. The length scale $2\pi/\Delta k_\parallel$ is plotted as a function of $t - t_\mathrm{w}$ in Fig. 67(b). Independent of the noise strength imposed before the quench, $2\pi/\Delta k_\parallel$ grows as a power law of time, with an exponent close to 0.25. This can be seen as a reversal of the process observed before the quench, where the wave length λ^* corresponding to the peak position grows as $\lambda^* \sim t^{0.25}$ (see Sec. IV A). These results corroborate the notion that processes parallel to the stripe pattern are described by a dynamic exponent $z = 4$.

Summary

In the present work, we have investigated the dynamics of modulated phases out of equilibrium using numerical simulations. We have focused on a two-dimensional stripe-forming system, called model B with Coulomb interactions [55, 64], relaxing from an ordered inital state under the influence of a noise term. To quantify the dynamics, the local stripe orientation $\theta(\mathbf{r}, t)$ was extracted from the simulation data. The spatio-temporal correlation functions of this quantity have been analyzed in detail, which represents the main contribution of this work. In case of the two-time autocorrelation function, we found a slow dynamics and aging, with a scaling form known from critical systems [44]. The aging could be linked to growing orientational correlation lengths. The correlation length perpendicular to the stripes grows as $\xi_\theta^\perp \sim t^{0.5}$. As it becomes comparable to the system size, a cross-over to a power-law decay is observed in the spatial correlation function. This behavior remains qualitatively unchanged over a wide range of noise strengths for which the system is in an ordered state. To clarify the origins of the aging, we performed quenches of stripe-forming systems by switching off the noise after a sufficiently long evolution at a finite noise strength. The subsequent approach to the perfectly ordered state is also slow, and no local minima of the free energy could be identified. This rules out an explanation of the aging phenomena as the effect of a complex free energy landscape. While topological defects appear at higher noise strengths, they have no significant influence on the dynamics of the stripe-forming system as long as the system is in the ordered state.

Using the structure factor of the orientation and the corresponding averaged correlation function, a second growing length scale could be identified. The dominant modulation length parallel to the stripes grows as $\lambda^* \sim t^{0.25}$. To further elucidate its behavior, we have performed a finite-size scaling analysis involving various system sizes and aspect ratios. In square systems and systems containing many short stripes, the aging dynamics becomes arrested after a finite time when the dominant modulation length parallel to the stripes reaches the system size. In contrast, in systems containing few but long stripes, the growth of the dominant modulation length as well as the aging continues, while the intensity of correlations saturates as a function of the number of stripes. We conclude that the coarsening process parallel to the stripes is essential for the orientation dynamics.

In the second part of this work, we have extended our investigation to other modulated phases. In the Swift-Hohenberg equation [53], which represents a different stripe-forming system, we found aging of the orientation correlations for both, a conserved and a non-conserved order parameter. As in the case of model B with Coulomb interactions, we observed a growing correlation length perpendicular to the stripes. As an example for a system with a different symmetry, we finally considered a hexagon-forming system relaxing from an ordered state. Here, aging was found in the translation autocorrelation function. However, the corresponding spatial correlation length saturates at a finite value, indicating that the aging process becomes interrupted. We have compared our results with the well-known Kosterlitz-Thouless-Nelson-Halperin-Young theory [207] for two-dimensional melting, but found no agreement with the sequence of phases described therein.

In summary, we have studied the aging behavior of ordered modulated phases in the presence of noise. It is well-known that there is a slow dynamics associated with the ordering processes in such phases, driven by the annihilation of domain walls and topological defects [16, 242]. However, the fact that modulated phases can remain out of equilibrium even when evolving from an ordered initial state has not been appreciated before. Based on our results, it seems that aging is the rule in ordered modulated phases, rather than the exception. There are two contributing factors to this behavior. One is the inherent instability of low-dimensional modulations [138, 243]. For instance, stripe phases in $d = 2$ (lamellae in $d = 3$) are periodic in only one direction, as opposed to crystals. Furthermore, the strength of fluctuations generally increases in low spatial dimensions [114, 138].

Acknowledgment

First, I would like to thank my advisor Prof. Dr. Robert Magerle for giving me the opportunity to pursue these studies, and for many years of collaboration. I am also grateful to my co-advisor, Prof. Dr. Günter Radons, for numerous joint discussions leading up to the publication of Ref. [44]. Furthermore, I would like to thank Hugues Chaté, Michael C. Cross, Leticia F. Cugliandolo, Gilles Tarjus, and John J. Toner, who kindly made time to discuss my results. Finally, I acknowledge the Chemical Physics group, Institute of Physics, TU Chemnitz, for being great colleagues.

References

[1] H. E. Stanley, *Introduction to phase transitions and critical phenomena* (Oxford University Press, Oxford, 1971).

[2] L. P. Kadanoff, *Statistical physics: statics, dynamics and renormalization* (World Scientific, Singapore, 2000).

[3] M. Plischke and B. Bergersen, *Equilibrium statistical physics*, 3rd ed. (World Scientific, Hackensack, NJ, 2006).

[4] L. F. Cugliandolo, C. R. Phys. **14**, 685 (2013).

[5] D. Frenkel and B. Smit, *Understanding molecular simulation: from algorithms to applications* (Academic, San Diego, 2002).

[6] D. P. Landau and K. Binder, *A guide to Monte Carlo simulations in statistical physics*, 3rd ed. (Cambridge University Press, Cambridge, 2009).

[7] J.-L. Barrat, M. Feigelman, J. Kurchan, and J. Dalibard, eds., *Slow Relaxations and nonequilibrium dynamics in condensed matter*, Les Houches, Vol. 77 (Springer, Berlin, 2003).

[8] L. Cugliandolo, in *Slow Relaxations and nonequilibrium dynamics in condensed matter*, Les Houches, Vol. 77, edited by J.-L. Barrat, M. Feigelman, J. Kurchan, and J. Dalibard (Springer, Berlin, 2003).

[9] M. Henkel, M. Pleimling, and R. Sanctuary, eds., *Ageing and the Glass Transition*, Lect. Notes Phys., Vol. 716 (Springer, Berlin, 2007).

[10] L. Berthier and G. Biroli, Rev. Mod. Phys. **83**, 587 (2011).

[11] E. Vincent, J. Hammann, M. Ocio, J.-P. Bouchaud, and L. Cugliandolo, in *Complex Behaviour of Glassy Systems*, Lect. Notes Phys., Vol. 492, edited by M. Rub and C. Prez-Vicente (Springer, Berlin, 1997) pp. 184–219.

[12] A. P. Young, *Spin glasses and random fields* (World Scientific, Singapore, 1998).

[13] T. R. Kirkpatrick and D. Thirumalai, Transp. Theory Stat. Phys **24**, 927 (1995).

[14] T. Castellani and A. Cavagna, J. Stat. Mech: Theory Exp. **2005**, P05012 (2005).

[15] L. F. Cugliandolo, J. Kurchan, and G. Parisi, J. Phys. I France **4**, 1641 (1994).

[16] A. J. Bray, Adv. Phys. **43**, 357 (1994).

[17] J. Kurchan and L. Laloux, J. Phys. A: Math. Gen. **29**, 1929 (1996).

[18] C. Godrèche and J. M. Luck, J. Phys.: Condens. Matter **14**, 1589 (2002).

[19] P. Calabrese and A. Gambassi, J. Phys. A: Math. Gen. **38**, R133 (2005).

[20] L. Berthier, J. L. Barrat, and J. Kurchan, Eur. Phys. J. B **11**, 635 (1999).

[21] M. Zannetti, in *Kinetics of phase transitions*, edited by S. Puri and V. K. Wadhawan (CRC Press, Boca Raton, FL, 2009).

[22] F. Corberi, L. F. Cugliandolo, and H. Yoshino, "Growing length scales in aging systems," in *Dynamical heterogeneities in glasses, colloids, and granular media*, Internat. Ser. Monogr. Phys., Vol. 150, edited by L. Berthier, G. Biroli, J.-P. Bouchaud, L. Cipelletti, and W. van Saarloos (Oxford University Press, Oxford, 2011) pp. 370–406, arXiv:1010.0149v1.

[23] M. Seul and D. Andelman, Science **267**, 476 (1995).

[24] G. H. Fredrickson and F. S. Bates, Annu. Rev. Mater. Sci. **26**, 501 (1996).

[25] I. W. Hamley, *The physics of block copolymers* (Oxford University Press, Oxford, 1998).

[26] M. J. Fasolka and A. M. Mayes, Annu. Rev. Mater. Res. **31**, 323 (2001).

[27] M. Seul and R. Wolfe, Phys. Rev. A **46**, 7519 (1992).

[28] A. B. Kashuba and V. L. Pokrovsky, Phys. Rev. B **48**, 10335 (1993).

[29] K. De'Bell, A. B. MacIsaac, and J. P. Whitehead, Rev. Mod. Phys. **72**, 225 (2000).

[30] O. Portmann, A. Vaterlaus, and D. Pescia, Nature **422**, 701 (2003).

[31] V. J. Emery, S. A. Kivelson, and J. M. Tranquada, Proc. Natl. Acad. Sci. USA **96**, 8814 (1999).

[32] S. A. Kivelson, I. P. Bindloss, E. Fradkin, V. Oganesyan, J. M. Tranquada, A. Kapitulnik, and C. Howald, Rev. Mod. Phys. **75**, 1201 (2003).

[33] E. Bodenschatz, W. Pesch, and G. Ahlers, Annu. Rev. Fluid Mech. **32**, 709 (2000).

[34] M. Lappa, *Thermal Convection: Patterns, Evolution and Stability* (Wiley, Chichester, 2010).

[35] R. Shlomovitz, L. Maibaum, and M. Schick, Biophys. J. **106**, 1979 (2014).

[36] I. R. Epstein and K. Showalter, J. Phys. Chem. **100**, 13132 (1996).

[37] A. De Wit, in *Adv. Chem. Phys.*, Vol. 109, edited by I. Prigogine and S. A. Rice (John Wiley & Sons, Inc., 1999) pp. 435–513.

[38] J. J. Christensen and A. J. Bray, Phys. Rev. E **58**, 5364 (1998).

[39] M. C. Cross and P. C. Hohenberg, Rev. Mod. Phys. **65**, 851 (1993).

[40] S. Puri and V. K. Wadhawan, *Kinetics of phase transitions* (CRC Press, Boca Raton, FL, 2009).

[41] L. Berthier, P. C. W. Holdsworth, and M. Sellitto, J. Phys. A: Math. Gen. **34**, 1805 (2001).

[42] S. Abriet and D. Karevski, Eur. Phys. J. B **37**, 47 (2004).

[43] P. Calabrese, A. Gambassi, and F. Krzakala, J. Stat. Mech: Theory Exp. **2006**, P06016 (2006).

[44] C. Riesch, G. Radons, and R. Magerle, Phys. Rev. E **90**, 052101 (2014).

[45] K. R. Elder, J. Viñals, and M. Grant, Phys. Rev. Lett. **68**, 3024 (1992).

[46] K. R. Elder, J. Viñals, and M. Grant, Phys. Rev. A **46**, 7618 (1992).

[47] M. C. Cross and D. I. Meiron, Phys. Rev. Lett. **75**, 2152 (1995).

[48] Y. Shiwa, T. Taneike, and Y. Yokojima, Phys. Rev. Lett. **77**, 4378 (1996).

[49] Q. Hou, S. Sasa, and N. Goldenfeld, Physica A **239**, 219 (1997).

[50] D. Boyer and J. Viñals, Phys. Rev. E **64**, 050101 (2001).

[51] D. Boyer and J. Viñals, Phys. Rev. E **65**, 046119 (2002).

[52] H. Qian and G. F. Mazenko, Phys. Rev. E **67**, 036102 (2003).

[53] J. Swift and P. C. Hohenberg, Phys. Rev. A **15**, 319 (1977).

[54] P. C. Hohenberg and B. I. Halperin, Rev. Mod. Phys. **49**, 435 (1977).

[55] T. Ohta and K. Kawasaki, Macromolecules **19**, 2621 (1986).

[56] U. Löw, V. J. Emery, K. Fabricius, and S. A. Kivelson, Phys. Rev. Lett. **72**, 1918 (1994).

[57] P. Viot and G. Tarjus, Europhys. Lett. **44**, 423 (1998).

[58] M. Grousson, G. Tarjus, and P. Viot, Phys. Rev. E **62**, 7781 (2000).

[59] M. Grousson, G. Tarjus, and P. Viot, Phys. Rev. E **65**, 065103 (2002).

[60] M. Grousson, V. Krakoviack, G. Tarjus, and P. Viot, Phys. Rev. E **66**, 026126 (2002).

[61] S. C. Glotzer and A. Coniglio, Phys. Rev. E **50**, 4241 (1994).

[62] C. B. Muratov, Phys. Rev. E **66**, 066108 (2002).

[63] J. W. Cahn, Acta Metall. **9**, 795 (1961).

[64] Y. Oono and Y. Shiwa, Mod. Phys. Lett. B **01**, 49 (1987).

[65] F. Liu and N. Goldenfeld, Phys. Rev. A **39**, 4805 (1989).

[66] I. W. Hamley, Macromol. Theory Simul. **9**, 363 (2000).

[67] S. R. Ren and I. W. Hamley, Macromolecules **34**, 116 (2001).

[68] Z.-F. Huang and J. Viñals, in *Nanostructured Soft Matter*, NanoScience and Technology, edited by A. V. Zvelindovsky (Springer, Dordrecht, 2007) pp. 371–393.

[69] M. Pinna and A. Zvelindovsky, Eur. Phys. J. B **85**, 210 (2012).

[70] S. C. Glotzer, E. A. Di Marzio, and M. Muthukumar, Phys. Rev. Lett. **74**, 2034 (1995).

[71] J. J. Christensen, K. Elder, and H. C. Fogedby, Phys. Rev. E **54**, R2212 (1996).

[72] S. Qi and Z.-G. Wang, J. Chem. Phys. **111**, 10681 (1999).

[73] L. Q. Chen and J. Shen, Comput. Phys. Commun. **108**, 147 (1998).

[74] X.-F. Wu and Y. A. Dzenis, J. Chem. Phys. **125**, 174707 (2006).

[75] X.-F. Wu and Y. A. Dzenis, Phys. Rev. E **77**, 031807 (2008).

[76] H. Ceniceros and G. Mohler, Multiscale Model. Sim. **6**, 212 (2007).

[77] A. W. Bosse, Macromol. Theory Simul. **19**, 399 (2010).

[78] A. W. Bosse, Phys. Rev. E **85**, 042801 (2012).

[79] D. A. Egolf, I. V. Melnikov, and E. Bodenschatz, Phys. Rev. Lett. **80**, 3228 (1998).

[80] C. Harrison, D. H. Adamson, Z. Cheng, J. M. Sebastian, S. Sethuraman, D. A. Huse, R. A. Register, and P. M. Chaikin, Science **290**, 1558 (2000).

[81] C. Harrison, Z. Cheng, S. Sethuraman, D. A. Huse, P. M. Chaikin, D. A. Vega, J. M. Sebastian, R. A. Register, and D. H. Adamson, Phys. Rev. E **66**, 011706 (2002).

[82] N. Becker and G. Ahlers, J. Stat. Mech: Theory Exp. **2006**, P12002 (2006).

[83] M. Kass and A. Witkin, Comput. Vis. Graph. Image Process. **37**, 362 (1987).

[84] J. Bigün and G. H. Granlund, in *Proc. IEEE First International Conference on Computer Vision* (London, Great Britain, 1987) pp. 433–438.

[85] B. Jähne, *Digital image processing*, 6th ed. (Springer, Berlin, 2005).

[86] H. Knutsson, in *IEEE Computer Society Workshop on Computer Architecture for Pattern Analysis and Image Database Management - CAPAIDM : Miami Beach, Florida* (1985) pp. 175–182.

[87] B. Rieger and L. J. van Vliet, Image Vision Comput. **22**, 453 (2004).

[88] B. Rieger, L. J. van Vliet, and P. W. Verbeek, in *Image Analysis*, Lect. Notes Comp. Sci., Vol. 6688, edited by A. Heyden and F. Kahl (Springer, Berlin, 2011) pp. 774–783.

[89] L. J. van Vliet and P. W. Verbeek, in *ASCI'95, Proc. First Annual Conference of the Advanced School for Computing and Imaging* (Heijen, NL, 1995) pp. 442–450.

[90] J. v. d. Weijer, L. J. v. Vliet, P. W. Verbeek, and M. v. Ginkel, IEEE Trans. Pattern Anal. Mach. Intell. **23**, 1035 (2001).

[91] P.-G. de Gennes and J. Prost, *The physics of liquid crystals*, Internat. Ser. Monogr. Phys., Vol. 83 (Clarendon Press, Oxford, 1995).

[92] K. E. Daniels, O. Brausch, W. Pesch, and E. Bodenschatz, J. Fluid Mech. **597**, 261 (2008).

[93] A. W. Bosse, J. Vac. Sci. Technol. B **29**, 031803 (2011).

[94] A. W. Bosse, J. Vac. Sci. Technol. B **29**, 06F202 (2011).

[95] P. N. Patrone and G. M. Gallatin, Macromolecules **45**, 9507 (2012).

[96] J.-P. Bouchaud, L. F. Cugliandolo, J. Kurchan, and M. Mézard, "Out of equilibrium dynamics in spin-glasses and other glassy systems," in *Spin Glasses and Random Fields*, edited by A. P. Young (World Scientific, Singapore, 1998) Chap. 6, pp. 161–223, arXiv:cond-mat/9702070v1.

[97] M. Henkel and M. Pleimling, *Non-equilibrium phase transitions*, Vol. 2 (Springer, Dordrecht, 2010).

[98] D. A. Huse, Phys. Rev. B **40**, 304 (1989).

[99] V. L. Berezinskiĭ, Sov. Phys. JETP **32**, 493 (1971).

[100] J. M. Kosterlitz and D. J. Thouless, J. Phys. C: Solid State Phys. **6**, 1181 (1973).

[101] J. M. Kosterlitz, J. Phys. C: Solid State Phys. **7**, 1046 (1974).

[102] A. La Porta and C. M. Surko, Phys. Rev. E **56**, 5351 (1997).

[103] A. C. Newell, T. Passot, and J. Lega, Annu. Rev. Fluid Mech. **25**, 399 (1993).

[104] J. Toner and D. R. Nelson, Phys. Rev. B **23**, 316 (1981).

[105] N. D. Mermin and H. Wagner, Phys. Rev. Lett. **17**, 1133 (1966).

[106] N. D. Mermin, Phys. Rev. **176**, 250 (1968).

[107] S. T. Bramwell and P. C. W. Holdsworth, Phys. Rev. B **49**, 8811 (1994).

[108] S. T. Bramwell, K. Christensen, J.-Y. Fortin, P. C. W. Holdsworth, H. J. Jensen, S. Lise, J. M. López, M. Nicodemi, J.-F. Pinton, and M. Sellitto, Phys. Rev. Lett. **84**, 3744 (2000).

[109] N. G. van Kampen, *Stochastic processes in physics and chemistry* (Elsevier, Amsterdam, 2008).

[110] S. T. Bramwell, P. C. W. Holdsworth, and J.-F. Pinton, Nature **396**, 552 (1998).

[111] P. Archambault, S. T. Bramwell, J.-Y. Fortin, P. C. W. Holdsworth, S. Peysson, and J.-F. Pinton, J. Appl. Phys. **83**, 7234 (1998).

[112] S. T. Bramwell, J.-Y. Fortin, P. C. W. Holdsworth, S. Peysson, J.-F. Pinton, B. Portelli, and M. Sellitto, Phys. Rev. E **63**, 041106 (2001).

[113] P. Archambault, S. T. Bramwell, and P. C. W. Holdsworth, J. Phys. A: Math. Gen. **30**, 8363 (1997).

[114] P. M. Chaikin and T. C. Lubensky, *Principles of condensed matter physics* (Cambridge University Press, Cambridge, 1995).

[115] J. Schmalian and P. G. Wolynes, Phys. Rev. Lett. **85**, 836 (2000).

[116] H. Westfahl, J. Schmalian, and P. G. Wolynes, Phys. Rev. B **64**, 174203 (2001).

[117] C.-Z. Zhang and Z.-G. Wang, Phys. Rev. E **73**, 031804 (2006).

[118] A. C. Ribeiro Teixeira, D. A. Stariolo, and D. G. Barci, Phys. Rev. E **87**, 062121 (2013).

[119] M. Goldstein, J. Chem. Phys. **51**, 3728 (1969).

[120] F. H. Stillinger and T. A. Weber, Science **225**, 983 (1984).

[121] T. B. Schrøder, S. Sastry, J. C. Dyre, and S. C. Glotzer, J. Chem. Phys. **112**, 9834 (2000).

[122] M. S. Heutmaker, P. N. Fraenkel, and J. P. Gollub, Phys. Rev. Lett. **54**, 1369 (1985).

[123] M. S. Heutmaker and J. P. Gollub, Phys. Rev. A **35**, 242 (1987).

[124] Y. Hu, R. E. Ecke, and G. Ahlers, Phys. Rev. Lett. **74**, 391 (1995).

[125] T. Galla and E. Moro, Phys. Rev. E **67**, 035101 (2003).

[126] A. D. Rutenberg and A. J. Bray, Phys. Rev. E **51**, R1641 (1995).

[127] N. Goldenfeld, *Lectures on phase transitions and the renormalization group* (Addison-Wesley, Reading, MA, 1992).

[128] S. A. Brazovskiǐ, Sov. Phys. JETP **41**, 85 (1975).

[129] F. S. Bates, J. H. Rosedale, G. H. Fredrickson, and C. J. Glinka, Phys. Rev. Lett. **61**, 2229 (1988).

[130] F. S. Bates, J. H. Rosedale, and G. H. Fredrickson, J. Chem. Phys. **92**, 6255 (1990).

[131] Y. Shiwa, H. Matsunaga, M. Yoshikawa, and H. Yoshitomi, Phys. Rev. E **49**, 2082 (1994).

[132] S. Komura, J.-i. Fukuda, and G. C. Paquette, Phys. Rev. E **53**, R5588 (1996).

[133] N. A. Gross, M. Ignatiev, and B. Chakraborty, Phys. Rev. E **62**, 6116 (2000).

[134] P. L. Geissler and D. R. Reichman, Phys. Rev. E **69**, 021501 (2004).

[135] P. C. Hohenberg and J. B. Swift, Phys. Rev. A **46**, 4773 (1992).

[136] J. Oh and G. Ahlers, Phys. Rev. Lett. **91**, 094501 (2003).

[137] T. Taneike and Y. Shiwa, J. Phys.: Condens. Matter **11**, L147 (1999).

[138] L. D. Landau and E. M. Lifshitz, *Statistical physics* (Pergamon Press, Oxford, 1959).

[139] Y. Oono and M. Bahiana, Phys. Rev. Lett. **61**, 1109 (1988).

[140] C. Yeung and R. C. Desai, Phys. Rev. E **49**, 2096 (1994).

[141] M. E. Fisher and M. N. Barber, Phys. Rev. Lett. **28**, 1516 (1972).

[142] K. Binder, in *Computational Methods in Field Theory*, Lect. Notes Phys., Vol. 409, edited by H. Gausterer and C. Lang (Springer, Berlin, 1992) pp. 59–125.

[143] J. Viñals and D. Jasnow, Phys. Rev. B **37**, 9582 (1988).

[144] H. Guo, Q. Zheng, and J. D. Gunton, Phys. Rev. B **38**, 11547 (1988).

[145] N. Wilding, C. Münkel, and D. W. Heermann, Z. Phys. B **94**, 301 (1994).

[146] S. K. Das, M. E. Fisher, J. V. Sengers, J. Horbach, and K. Binder, Phys. Rev. Lett. **97**, 025702 (2006).

[147] S. Majumder and S. K. Das, Phys. Rev. E **81**, 050102 (2010).

[148] S. Majumder and S. K. Das, Phys. Rev. E **84**, 021110 (2011).

[149] S. K. Das, S. Roy, S. Majumder, and S. Ahmad, Europhys. Lett. **97**, 66006 (2012).

[150] J. Midya, S. Majumder, and S. K. Das, J. Phys.: Cond. Mat. **26**, 452202 (2014).

[151] A. Mendoza-Coto, D. A. Stariolo, and L. Nicolao, Phys. Rev. Lett. **114**, 116101 (2015).

[152] A.-L. Barabási and E. H. Stanley, *Fractal concepts in surface growth* (Cambridge University Press, Cambridge, 1995).

[153] F. Family and T. Vicsek, J. Phys. A: Math. Gen. **18**, L75 (1985).

[154] P. N. Patrone and G. M. Gallatin, Macromolecules **47**, 4824 (2014).

[155] D. Sundrani, S. B. Darling, and S. J. Sibener, Nano Lett. **4**, 273 (2004).

[156] M. R. Hammond, E. Cochran, G. H. Fredrickson, and E. J. Kramer, Macromolecules **38**, 6575 (2005).

[157] M. R. Hammond and E. J. Kramer, Macromolecules **39**, 1538 (2006).

[158] V. Mishra, G. H. Fredrickson, and E. J. Kramer, ACS Nano **6**, 2629 (2012).

[159] V. Mishra and E. J. Kramer, Macromolecules **46**, 977 (2013).

[160] H. J. Ryu, Q. Tong, and S. J. Sibener, J. Phys. Chem. Lett. **4**, 2890 (2013).

[161] R. C. Ball and R. L. H. Essery, J. Phys.: Condens. Matter **2**, 10303 (1990).

[162] G. Brown and A. Chakrabarti, J. Chem. Phys. **101**, 3310 (1994).

[163] V. Weith, A. Krekhov, and W. Zimmermann, J. Chem. Phys. **139**, 054908 (2013).

[164] H. R. Schober, E. Allroth, K. Schroeder, and H. Müller-Krumbhaar, Phys. Rev. A **33**, 567 (1986).

[165] M. Bahiana and Y. Oono, Phys. Rev. A **41**, 6763 (1990).

[166] A. Chakrabarti and J. D. Gunton, Phys. Rev. E **47**, R792 (1993).

[167] Although we have stated before that the system is initially homogeneous, a small random perturbation must be added to $\psi(\mathbf{r}, t = 0)$ in the case $\eta = 0$ to enable microphase separation. In case of a finite noise strength $\eta > 0$, the perturbation is provided by the noise $\zeta(\mathbf{r}, t)$.

[168] The usual dynamical exponent [97] $z \equiv \frac{1}{y}$. We avoid this notation, as z might not be an integer in our case.

[169] K. R. Elder and M. Grant, J. Phys. A: Math. Gen. **23**, L803 (1990).

[170] R. Mulet and D. A. Stariolo, Phys. Rev. B **75**, 064108 (2007).

[171] H. Furukawa, J. Phys. Soc. Jpn. **58**, 216 (1989).

[172] D. S. Fisher and D. A. Huse, Phys. Rev. B **38**, 373 (1988).

[173] Y. Pomeau and P. Manneville, J. Physique Lett. **40**, 609 (1979).

[174] K. R. Elder, M. Katakowski, M. Haataja, and M. Grant, Phys. Rev. Lett. **88**, 245701 (2002).

[175] H. Emmerich, H. Löwen, R. Wittkowski, T. Gruhn, G. I. Tóth, G. Tegze, and L. Gránásy, Adv. Phys. **61**, 665 (2012).

[176] A. Chakrabarti, R. Toral, and J. D. Gunton, Phys. Rev. A **44**, 6503 (1991).

[177] Y. Shiwa, Phys. Lett. A **228**, 279 (1997).

[178] G. H. Fredrickson and K. Binder, J. Chem. Phys. **91**, 7265 (1989).

[179] S. Qi and Z.-G. Wang, Phys. Rev. Lett. **76**, 1679 (1996).

[180] S. Qi and Z.-G. Wang, Phys. Rev. E **55**, 1682 (1997).

[181] H. Ohnogi and Y. Shiwa, Phys. Rev. E **84**, 011611 (2011).

[182] K. R. Elder and M. Grant, Phys. Rev. E **70**, 051605 (2004).

[183] H. Emmerich, Adv. Phys. **57**, 1 (2008).

[184] D. A. Vega, C. K. Harrison, D. E. Angelescu, M. L. Trawick, D. A. Huse, P. M. Chaikin, and R. A. Register, Phys. Rev. E **71**, 061803 (2005).

[185] K. J. Strandburg, Rev. Mod. Phys. **60**, 161 (1988).

[186] J. G. Dash, Rev. Mod. Phys. **71**, 1737 (1999).

[187] C. Alba-Simionesco, B. Coasne, G. Dosseh, G. Dudziak, K. E. Gubbins, R. Radhakrishnan, and M. Sliwinska-Bartkowiak, J. Phys.: Condens. Matter **18**, R15 (2006).

[188] U. Gasser, C. Eisenmann, G. Maret, and P. Keim, ChemPhysChem **11**, 963 (2010).

[189] R. A. Segalman, A. Hexemer, R. C. Hayward, and E. J. Kramer, Macromolecules **36**, 3272 (2003).

[190] R. A. Segalman, A. Hexemer, and E. J. Kramer, Phys. Rev. Lett. **91**, 196101 (2003).

[191] D. E. Angelescu, C. K. Harrison, M. L. Trawick, R. A. Register, and P. M. Chaikin, Phys. Rev. Lett. **95**, 025702 (2005).

[192] G. E. Stein, E. J. Kramer, X. Li, and J. Wang, Phys. Rev. Lett. **98**, 086101 (2007).

[193] G. E. Stein, W. B. Lee, G. H. Fredrickson, E. J. Kramer, X. Li, and J. Wang, Macromolecules **40**, 5791 (2007).

[194] C. A. Murray and D. H. Van Winkle, Phys. Rev. Lett. **58**, 1200 (1987).

[195] A. H. Marcus and S. A. Rice, Phys. Rev. Lett. **77**, 2577 (1996).

[196] K. Zahn, R. Lenke, and G. Maret, Phys. Rev. Lett. **82**, 2721 (1999).

[197] T. Terao and T. Nakayama, Phys. Rev. E **60**, 7157 (1999).

[198] K. Zahn and G. Maret, Phys. Rev. Lett. **85**, 3656 (2000).

[199] P. Keim, G. Maret, U. Herz, and H. H. von Grünberg, Phys. Rev. Lett. **92**, 215504 (2004).

[200] P. Keim, G. Maret, and H. H. von Grünberg, Phys. Rev. E **75**, 031402 (2007).

[201] Y. Peng, Z. Wang, A. M. Alsayed, A. G. Yodh, and Y. Han, Phys. Rev. Lett. **104**, 205703 (2010).

[202] J. B. Pieper, J. Goree, and R. A. Quinn, J. Vac. Sci. Technol. A **14**, 519 (1996).

[203] R. A. Quinn and J. Goree, Phys. Rev. E **64**, 051404 (2001).

[204] V. Nosenko, S. K. Zhdanov, A. V. Ivlev, C. A. Knapek, and G. E. Morfill, Phys. Rev. Lett. **103**, 015001 (2009).

[205] J. S. Olafsen and J. S. Urbach, Phys. Rev. Lett. **95**, 098002 (2005).

[206] B. I. Halperin and D. R. Nelson, Phys. Rev. Lett. **41**, 121 (1978).

[207] D. R. Nelson and B. I. Halperin, Phys. Rev. B **19**, 2457 (1979).

[208] A. P. Young, Phys. Rev. B **19**, 1855 (1979).

[209] B. Jancovici, Phys. Rev. Lett. **19**, 20 (1967).

[210] M. Nonomura and T. Ohta, J. Phys.: Condens. Matter **13**, 9089 (2001).

[211] C. Harrison, D. E. Angelescu, M. Trawick, Z. Cheng, D. A. Huse, P. M. Chaikin, D. A. Vega, J. M. Sebastian, R. A. Register, and D. H. Adamson, Europhys. Lett. **67**, 800 (2004).

[212] R. Parthasarathy, Nat. Methods **9**, 724 (2012).

[213] F. Aurenhammer, ACM Comput. Surv. **23**, 345 (1991).

[214] C. B. Barber, D. P. Dobkin, and H. Huhdanpaa, ACM Trans. Math. Softw. **22**, 469 (1996).

[215] The MathWorks, Inc., *MATLAB Release 2007a* (Natick, MA, United States).

[216] K. E. Thompson, Int. J. Numer. Meth. Eng. **55**, 1345 (2002).

[217] M. Caroli and M. Teillaud, in *Algorithms - ESA 2009*, Lect. Notes Comp. Sci., Vol. 5757, edited by A. Fiat and P. Sanders (Springer, Berlin, 2009) pp. 59–70.

[218] D.-M. Yan, K. Wang, B. Levy, and L. Alonso, in *Voronoi Diagrams in Science and Engineering (ISVD), 2011 Eighth International Symposium on* (2011) pp. 177–184.

[219] A. Pertsinidis and X. S. Ling, Phys. Rev. Lett. **87**, 098303 (2001).

[220] A. Pertsinidis and X. S. Ling, New J. Phys. **7**, 33 (2005).

[221] C. Sagui and R. C. Desai, Phys. Rev. Lett. **71**, 3995 (1993).

[222] C. Sagui and R. C. Desai, Phys. Rev. E **52**, 2807 (1995).

[223] Y. Yokojima and Y. Shiwa, Phys. Rev. E **65**, 056308 (2002).

[224] H. Ohnogi and Y. Shiwa, Phys. Rev. E **84**, 051603 (2011).

[225] S. Ji, C.-C. Liu, W. Liao, A. L. Fenske, G. S. W. Craig, and P. F. Nealey, Macromolecules **44**, 4291 (2011).

[226] C. A. Knapek, D. Samsonov, S. Zhdanov, U. Konopka, and G. E. Morfill, Phys. Rev. Lett. **98**, 015004 (2007).

[227] P. Hartmann, A. Douglass, J. C. Reyes, L. S. Matthews, T. W. Hyde, A. Kovács, and Z. Donkó, Phys. Rev. Lett. **105**, 115004 (2010).

[228] P. Dillmann, G. Maret, and P. Keim, Eur. Phys. J. Spec. Top. **222**, 2941 (2013).

[229] M. Sushchik and L. Tsimring, Physica D **74**, 90 (1994).

[230] A. D. Pezzutti, D. A. Vega, and M. A. Villar, Phil. Trans. R. Soc. A **369**, 335 (2011).

[231] A. Adland, Y. Xu, and A. Karma, Phys. Rev. Lett. **110**, 265504 (2013).

[232] L. R. Gómez, E. M. Vallés, and D. A. Vega, Phys. Rev. Lett. **97**, 188302 (2006).

[233] L. R. Gómez, E. M. Vallés, and D. A. Vega, Physica A **386**, 648 (2007).

[234] Z. Wang, A. M. Alsayed, A. G. Yodh, and Y. Han, J. Chem. Phys. **132**, 154501 (2010).

[235] E. Hairer, S. P. Nørsett, and G. Wanner, *Solving ordinary differential equations*, Vol. 1 (Springer, Berlin, 2008).

[236] R. G. Petschek and H. Metiu, J. Chem. Phys. **79**, 3443 (1983).

[237] M. C. Cross, D. Meiron, and Y. Tu, Chaos **4**, 607 (1994).

[238] T. M. Rogers, K. R. Elder, and R. C. Desai, Phys. Rev. B **37**, 9638 (1988).

[239] R. E. Lynch, Appl. Numer. Math. **10**, 325 (1992).

[240] M. Abramowitz and I. A. Stegun, *Handbook of mathematical functions* (Dover Publications, New York, 1965).

[241] P. I. C. Teixeira and B. M. Mulder, Phys. Rev. E **55**, 3789 (1997).

[242] J. Viñals, J. Phys. Soc. Jpn. **78**, 041011 (2009).

[243] A. Caillé, C. R. Acad. Sci. Paris Sér. B **274**, 891 (1972).

Erklärung nach § 6 Absatz 2 Nr. 4 der Promotionsordnung

Hiermit erkläre ich, daß ich die vorliegende Dissertation selbständig verfaßt und keine anderen als die angegebenen Quellen und Hilfsmittel genutzt habe.

Chemnitz, den 20.05.2015

Christian Riesch

Curriculum vitae

Persönliche Daten

Name	Christian Hinnerk Riesch
Anschrift	Kehrenbergstr. 3 D-34327 Körle
Geburtsdatum	13.01.1984
Geburtsort	Kassel
Staatsangehörigkeit	deutsch
Familienstand	ledig

Ausbildung

2003	Abitur, Albert-Schweitzer-Schule, Kassel
2003-2004	Studium der Mechatronik, Universität Kassel
2004-2009	Studium Computational Science, TU Chemnitz
2007	Bachelor of Science, Abschlußarbeit: *Analyse von SPM-Bilddaten mittels Gabortransformation*
2009	Master of Science, Abschlußarbeit: *Quantitative Analysis of Ordering Phenomena in Block Copolymer Thin Films*
2009-2015	Doktorand, Chemische Physik, TU Chemnitz

Berufserfahrung

2009-2015	Wissenschaftlicher Mitarbeiter, Chemische Physik, TU Chemnitz

Publications

Articles in peer-reviewed journals:

- C. Dietz, M. Zerson, C. Riesch, A. M. Gigler, R. W. Stark, N. Rehse, and R. Magerle, *Nanotomography with enhanced resolution using bimodal atomic force microscopy*, Appl. Phys. Lett. **92**, 143107 (2008),
- C. Dietz, M. Zerson, C. Riesch, M. Franke, and R. Magerle, *Surface properties of elastomeric polypropylenes studied with atomic force microscopy*, Macromolecules **41**, 9259 (2008),
- E.-C. Spitzner, C. Riesch, and R. Magerle, *Subsurface imaging of soft polymeric materials with nanoscale resolution*, ACS Nano **5**, 315 (2011),
- M. Zerson, E.-C. Spitzner, C. Riesch, R. Lohwasser, M. Thelakkat, and R. Magerle, *Subsurface mapping of amorphous surface layers on poly(3-hexylthiophene)*, Macromolecules **44**, 5874 (2011),
- E.-C. Spitzner, C. Riesch, R. Szilluweit, L. Tian, H. Frauenrath, and R. Magerle, *Multiset point intermittent contact (MUSIC) mode atomic force microscopy of oligothiophene fibrils*, ACS Macro Lett. **1**, 380 (2012).
- C. Riesch, G. Radons, and R. Magerle, *Aging of orientation fluctuations in stripe phases*, Phys. Rev. E **90**, 052101 (2014).
- C. Dietz, M. Schulze, A. Voss, C. Riesch, and R. W. Stark, *Bimodal frequency-modulated atomic force microscopy with small cantilevers*, Nanoscale **7**, 1849 (2015).

Conference contributions:

- C. Riesch, E.-C. Spitzner and R. Magerle, *Quantitative analysis of block copolymer microdomain dynamics* (poster), Frühjahrstagung der DPG, Dresden, 2009,

- C. Riesch, E.-C. Spitzner, and R. Magerle, *Quantitative analysis of block copolymer microdomain dynamics* (poster), Bayreuth Polymer Symposium, Bayreuth, 2009
- C. Riesch and R. Magerle, Scaling behaviour in a minimal model for block copolymer microdomain ordering (poster), Frühjahrstagung der DPG, Regensburg, 2010,
- C. Riesch, G. Radons, and R. Magerle, *Spatio-temporal correlations in a minimal model for block copolymer microdomain ordering* (poster), 43rd IUPAC World Polymer Congress 'Macro2010', Glasgow, 2010,
- C. Riesch, G. Radons, and R. Magerle, *Aging behavior in temporal correlations in a stripe-forming system* (poster), 15th Fall Seminar on Nonlinear Dynamics, Bayreuth, 2010,
- C. Riesch, G. Radons, and R. Magerle, *Glassy dynamics of orientation fluctuations in a stripe-forming system* (poster), Frühjahrstagung der DPG, Dresden, 2010,
- C. Riesch, G. Radons, and R. Magerle, *Glassy dynamics of kinks in stripe phases* (contributed talk), 16th Fall Seminar on Nonlinear Dynamics, Bayreuth, 2011,
- C. Riesch, G. Radons, and R. Magerle, *Glassy dynamics of kinks in stripe phases* (poster), Unifying Concepts in Glass Physics V, Paris, 2011,
- C. Riesch, G. Radons, and R. Magerle, *Glassy dynamics of kinks in stripe phases* (poster), Frühjahrstagung der DPG, Berlin, 2012,
- C. Riesch, G. Radons, and R. Magerle, *Glassy dynamics of orientation fluctuations in stripe phases* (poster), 17th Fall Seminar on Nonlinear Dynamics, Bayreuth, 2012,
- C. Riesch, G. Radons, and R. Magerle, *Glassy dynamics of orientation fluctuations in modulated phases* (poster), Frühjahrstagung der DPG, Regensburg, 2013,
- C. Riesch, G. Radons, and R. Magerle, *Aging of orientation fluctuations in modulated phases* (contributed talk), 7th International Discussion Meeting on Relaxations in Complex Systems, Barcelona, 2013,
- C. Riesch, G. Radons, and R. Magerle, *Non-equilibrium dynamics of ordered modulated phases* (poster), Frühjahrstagung der DPG, Dresden, 2014,

- C. Riesch, G. Radons, and R. Magerle, *Anisotropic finite-size scaling of orientation correlation functions in stripe phases free of topological defects* (poster), Workshop „Luxembourg out of Equilibrium“, Luxembourg, 2015.